AFCRL-71-0573

EXPERIMENTATION AND INVESTIGATION OF OPTICAL-IRRADIATION-INDUCED SURFACE DAMAGE IN OPTICALLY NONLINEAR MATERIALS

by
Michael Bass
Harrison H. Barrett
Lowell H. Holway, Jr.

RAYTHEON COMPANY
RESEARCH DIVISION
WALTHAM, MASSACHUSETTS 02154

Contract No. F19628-70-C-0223

Project No. 4645
Task No. 464502
Work Unit No. 46450201

SCIENTIFIC REPORT No. 1

FEBRUARY 1972

Contract Monitor: Dr. David Milam, CROL Optical Physics Laboratory

Sponsored by

Advanced Research Projects Agency
ARPA Order No. 1434 AMD #1

Monitored by
AIR FORCE CAMBRIDGE RESEARCH LABORATORIES
AIR FORCE SYSTEMS COMMAND
UNITED STATES AIR FORCE
BEDFORD, MASSACHUSETTS 01730

Program code no 0D10

Effective date of contract .....1 May 1970

Contract expiration date .....1 November 1972

Principal investigator and phone no .....Dr. Michael Bass,
617-899-8400, ext. 2475

Project scientist and phone no .....Dr. David Milam,
617-861-3898

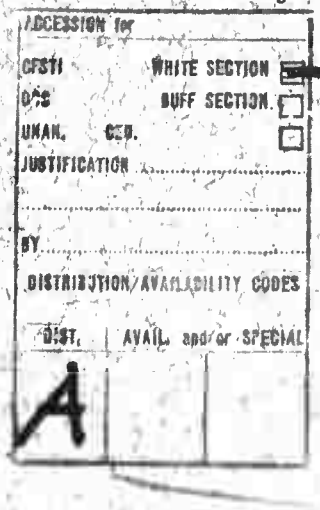

Qualified requestors may obtain additional copies from the Defense Documentation Center. All others should apply to the National Technical Information Service.

Unclassified

Security Classification

DOCUMENT CONTROL DATA - R & D

(Security classification of title, body of abstract and indexing annotation must be entered when the overall report is classified)

1. ORIGINATING ACTIVITY (Corporate author)
Raytheon Research Division
Waltham, Massachusetts 02154

2a. REPORT SECURITY CLASSIFICATION
Unclassified

2b. GROUP
N/A

3. REPORT TITLE
EXPERIMENTATION AND INVESTIGATION OF OPTICAL-IRRADIATION-INDUCED SURFACE DAMAGE IN OPTICALLY NONLINEAR MATERIALS

4. DESCRIPTIVE NOTES (Type of report and inclusive dates)
Scientific Interim

5. AUTHOR(S) (First name, middle initial, last name)
Michael Bass
Harrison H. Barrett
Lowell H. Holway, Jr.

6. REPORT DATE
February 1972

7a. TOTAL NO. OF PAGES
117

7b. NO. OF REFS
40

8a. CONTRACT OR GRANT NO. ARPA Order No. 1434
F19628-70-C-0223

b. Project, Task, Work Unit Nos.
4645-02-01

c. DOD Element:
62403F

d. DOD Subelement: 634645

9a. ORIGINATOR'S REPORT NUMBER(S)
S-1378
Scientific Report No. 1

9b. OTHER REPORT NO(S) (Any other numbers that may be assigned this report)
AFCRL-71-0573

10. DISTRIBUTION STATEMENT
Approved for public release; distribution unlimited.

11. SUPPLEMENTARY NOTES
This research was supported by the Advanced Research Projects Agency

12. SPONSORING MILITARY ACTIVITY
A.F. Cambridge Research Labs. (OP)
L.G. Hanscom Field
Bedford, Massachusetts 01730

13. ABSTRACT

Surface damage to optically nonlinear materials has been studied both experimentally and theoretically. The most important conclusion reached to date is that laser-induced damage to transparent materials is characterized by a probability for damage at each incident power density. This is in contrast to the view previously held, that there was a threshold power density which divided damaging levels from those which would do no damage.

A model for the damaging process, based on the probability measurements and electron avalanche breakdown, has been devised. In its simplest form, this model has successfully explained the most important properties of the measured damage probability in over 10 different materials. This model is being refined to examine such areas as the dependence of damage probability on laser frequency and the temporal distribution of breakdown starting times.

The present program has also explained the difference between damage produced by multimode and TEM_{00} mode laser beams, shown that the form of damage (whether on the surfaces or in the volume) depends on the laser beam geometry and has demonstrated, using streak camera photography, the upstream movement of the beam focal point under self-focusing conditions. In addition, a refined theoretical analysis of self-focusing with both instantaneous and finite response-time mechanisms has been developed.

DD Form 1473 (Nov 68) [illegible]

Unclassified

Security Classification

14. KEY WORDS	LINK A		LINK B		LINK C	
	ROLE	WT	ROLE	WT	ROLE	WT
Laser-induced damage						
Solid-state lasers						
Damage probability						
Damage dynamics						
Temporal properties of damage						
Nonlinear materials						
Avalanche breakdown						
Self-focusing						

AFCRL-71-0573 S-1378

EXPERIMENTATION AND INVESTIGATION OF OPTICAL-IRRADIATION-INDUCED SURFACE DAMAGE IN OPTICALLY NONLINEAR MATERIALS

by

Michael Bass, Harrison H. Barrett, and Lowell H. Holway, Jr.

Raytheon Company
Research Division
Waltham, Massachusetts 02154

Contract No. F19628-70-C-0223
Project No. 4645
Task No. 464502
Work Unit No. 46450201

Scientific Report No. 1

February 1972

Contract Monitor: David Milam,
Optical Physics Laboratory

Sponsored by
Advanced Research Projects Agency
ARPA Order No. 1434
Monitored by
Air Force Cambridge Research Laboratories
Air Force Systems Command
United States Air Force
Bedford, Massachusetts 01730

ABSTRACT

Surface damage to optically nonlinear materials has been studied both experimentally and theoretically. The most important conclusion reached to date is that laser-induced damage to transparent materials is characterized by a probability for damage at each incident power density. This is in contrast to the previously held view that there was a threshold power density which divided damaging levels from those which would do no damage.

A model for the damaging process, based on the probability measurements and electron avalanche breakdown, has been devised. In its simplest form this model has successfully explained the most important properties of the measured damage probability in over 10 different materials. This model is being refined to examine such areas as the dependence of damage probability on laser frequency and the temporal distribution of breakdown starting times.

The present program has also explained the difference between damage produced by multimode and TEM_{00} mode laser beams, shown that the form of damage (whether on the surfaces or in the volume) depends on the laser beam geometry and demonstrated, using streak camera photography, the upstream movement of the beam focal point under self-focusing conditions. In addition a refined theoretical analysis of self-focusing with both instantaneous and finite response-time mechanisms has been developed.

FOREWORD

This scientific report describes work performed under Contract No. F19628-70-C-0023 between 1 May 1970 and 31 October 1971. The report was assigned a Raytheon internal number S-1378.

Work was carried out at the Raytheon Research Division in Waltham, Massachusetts. The Principal Investigator was Dr. Michael Bass. Dr. Harrison H. Barrett was responsible for the development of the avalanche breakdown model and Dr. Lowell Holway contributed the theoretical analyses of self-focusing. The authors gratefully acknowledge the perserverance of D. Bua and T. Varitimos in amassing the great quantities of data necessary for this work. The authors also wish to thank J. Geller of Photometrics, Inc., Lexington, Mass. for the excellent SEM micrographs. Useful discussions with Dr. Frank Horrigan of Raytheon and Drs. David Milam and Erlan Bliss of AFCRL are also acknowledged.

This report was submitted by the authors on 30 November 1971.

TABLE OF CONTENTS

TABLE OF CONTENTS (CONT'D)

LIST OF ILLUSTRATIONS

LIST OF ILLUSTRATIONS (CONT'D)

LIST OF ILLUSTRATIONS (CONT'D)

LIST OF ILLUSTRATIONS (CONT'D)

I. INTRODUCTION

The essential component in many modulators and Q switches, and in all frequency doublers and parametric oscillators, is an optically nonlinear crystal. Unfortunately, the nonlinear materials having the largest nonlinearities (i.e., linear electro-optic coefficients, second harmonic generation (SHG) coefficients, etc.) are often those most easily damaged by intense laser beams. Even the slightest damage, which can occur on the surfaces or in the volume of the material, can render the crystal useless. Damage to optically nonlinear materials is thus a major limitation in the design of high-power lasers and optical devices.

Most reports which describe new optically nonlinear materials mention the occurrence of index-of-refraction gradients when high-average-power visible light passes through the crystal. In $LiNbO_3$ this type of damage is thought to be caused by the presence of crystalline imperfections, possibly oxygen vacancies, which trap electrons. Visible light frees these electrons, which then move away from the imperfection. The resulting internal electric fields cause index-of-refraction gradients throughout the crystal, by means of the linear electro-optic effect. Thus a coherent process such as phase-matched SHG will be severely limited. However, since heating the crystal permits the electrons to return to their initial sites, this type of damage is reversible.

On the other hand, when the light intensity incident on the crystal is high enough, irreversible damage occurs. Because of residual absorption, very high average power beams can heat the material to the point where thermal-stress-induced fracture occurs. The present program, however, is concerned with damage caused by very high-peak-power pulses of light to crystals which do not absorb at the optical wavelength. When exposed to such pulses, the crystal's surfaces may become pitted and charred, and/or the interior may become cracked or filled with bubbles. This catastrophic damage can be corrected only by re-polishing the surfaces or by replacing an internally damaged crystal.

The objective of this program is to determine how and why permanent damage is produced and to find means to minimize or avoid its deleterious effects on laser systems. The work to date can be grouped into three general areas: 1. Studies of the residual damage after irradiation using optical and electron microscopy; 2. Studies of the dynamics of the damage process using high-speed streak photography; and 3. Determination of the probability that a particular laser pulse will damage a particular material. The following list summarizes the major results reached to date:

1. Residual damage was found only after the laser irradiation caused a visible spark when passing through the sample.

2. The importance of uniform ("hot spot" free) illumination in increasing the ability of a material to withstand laser irradiation was demonstrated by comparing TEM_{00} and multimode damage.

3. Contrary to previously held opinions, when $LiNbO_3$ and KDP are used as Pockel's cell or frequency doubler crystals, internal damage is produced at the same or lower levels of irradiation than those required to produce surface damage.

4. The laser beam's focusing conditions determine the form of the residual damage; that is, whether it is internal, entrance- or exit-face damage.

5. Internal filamentary damage in $LiNbO_3$ was found to be composed of a series of very fine, nearly planar cracks which intersect to form one or more long lines having diameter $\approx 0.4\mu m$. When illuminated with visible light, diffraction effects make these lines appear blurred and give the impression of a "tube" of damaged material.

6. Experiments designed to study the dynamics of damage formation by photographing the laser-induced breakdown (the spark) with an image converter streak camera were initiated. The results of these measurements showed that when light is focused inside the material the first damage to occur is near the focal point and additional damage occurs upstream at later times. All laser-induced internal breakdowns were initiated during intervals of time when the level of irradiation increased or was maximum, and never when the intensity decreased.

7. A model for the results in 6 was developed, in which self-focusing was identified as likely to be responsible for the upstream movement of the sparks and a fast-response self-focusing process was shown to be able to explain the fact that internal breakdowns were only produced when the pulse intensity increased. The importance of beam geometry and non-self-focusing configurations were investigated.

8. There is, in general, no sharp threshold for laser-induced damage. There is, however, some probability that a particular pulse will damage a particular material. At very high levels of irradiation this probability is unity; at lower levels it is less than one, and at very low levels the probability for damage may be vanishingly small. This was studied with both Nd:YAG and ruby lasers.

9. Measurements of the dependence of damage probability on the laser beam's power density for ten different materials have led to a model for the damage mechanism based on avalanche breakdown. Good qualitative agreement has been obtained.

10. Using the streak camera, preliminary measurements of the distribution of breakdown starting times as a function of damage probability have been obtained. These data show that the most likely time for a breakdown to occur is before the peak of the laser pulse. This data may be explained using the probabilistic interpretation of laser-induced damage.

II. EXPERIMENTS

A. Parameters Necessary to Characterize Surface Damage

Since the operational characteristics of all lasers and laser systems vary widely, it is necessary to describe the light pulse responsible for the damage in question. In this manner, meaningful comparisons can be made between different materials and the results of different workers. The relevant properties of light pulses are listed in Table I. The pulse energy must be given in joules rather than some arbitrary relative unit which is meaningful only to the investigator who defines it. It is adequate to give the power density in standard units (MW/cm^2) if one also gives the pulse duration and area irradiated. Moreover, the definition of pulse duration (FWHP) or the time interval between 10 percent and 90 percent of the total energy, etc.) must be given to permit the pulse power to be computed. Finally, because the pattern and geometry of the beam incident on the crystal, these too are essential.

It is, of course, necessary to specify the state of the crystal and the irradiated surfaces by giving the parameters listed in Table II. Since contaminants such as polishing compounds and finger grease can lead to spurious conclusions, comments about the cleaning procedure are necessary. In addition, such crystalline properties as hardness or hydroscopic nature are necessary to a full description of the sample.

B. Defining the Occurrence of Damage

In all our experiments, residual damage could be observed only after a visible spark was produced by the interaction of the light and the sample. Even with 100X magnification no damage in the irradiated regions of the sample could be detected until after the spark was seen. Thus we chose as our definition of the occurrence of damage the statement that "damage has been produced when the passage of the laser pulse through the medium was accompanied by a visible spark." Post-irradiation inspection of the residual damage, however, may require inspection with proper illumination and magnification.

TABLE I

PARAMETERS NECESSARY TO CHARACTERIZE A PULSE OF LASER LIGHT

1. Wavelength and spectral width
2. Energy in joules
3. Pulse duration
4. Transverse mode pattern
5. Longitudinal mode content
6. Beam's transverse dimension at the surface
7. Position of focal point if any or the beam waist
8. Polarization state
9. Pulse repetition rate

TABLE II

PARAMETERS NECESSARY TO CHARACTERIZE A CRYSTALLINE SURFACE

1. Name of the crystal
2. How grown, including purity considerations
3. Presence of twinning
4. Ferroelectric domain structure
5. Cleaved or polished surfaces
6. Flatness of surfaces
7. Smoothness of surfaces
8. Cleanliness
9. Orientation of crystallographic axes and light beam k and E vectors
10. Temperature
11. Atmosphere surrounding the crystal
12. Dislocation count

C. The Lasers and Beam-Handling Optics

Figure 1 shows schematically the principal features of the laser damage source. The experiments in this program were performed using a pulse pumped, electro-optically Q switched, Nd:YAG, or ruby laser. The important properties of these devices are summarized in Table III.

The combination of one rotatable and one fixed polarizer resulted in a variable light attenuator which was highly sensitive, quite reproducible, and which did not affect the laser pulse's polarization, spatial distribution, or duration. If the fixed polarizer is oriented to transmit the laser polarization and if $\theta = 0°$ is the angle of the rotating polarizer which gives maximum transmission through this attenuator then the transmitted intensity at any other angle of rotation about the beam axis is

$$I(\theta) = bI_o \cos^4 \theta \quad .$$

I_o is the incident light intensity and b is the fraction transmitted when $\theta = 0°$.

D. Initial Experiments and Multimode vs TEM_{00} Mode Studies

The light from a multimode Nd:YAG laser was focused through a 10× microscope objective onto the entrance surface of several optically nonlinear materials in the very first experiments. During these experiments, we cared little for the orientation of the crystalline axes with respect to the light polarization, and used pulses which varied from ~ 10 to 30 nsec, depending on operating conditions. The pulse energy was varied by varying the laser input energy. We were, however, careful to obtain similar surface quality in all crystals (at least $\lambda/4$ flat over the small regions irradiated), treat them equally (except for those which were hydroscopic), use a low pulse repetition frequency (i.e., 1 pps), and to employ two observers to obtain two independent sets of data. The damage pattern caused by a focused "multimode" laser on a $LiNbO_3$ surface is shown in Fig. 2.

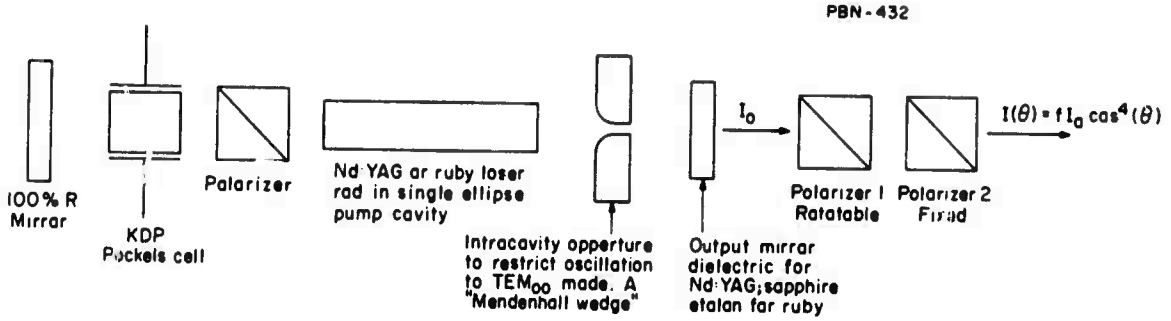

Fig. 1 Laser and Variable Attenuator Configuration for Damage Studies.

TABLE III

LASER PARAMETERS

Wavelength	Nd:YAG 1.06 μm	Ruby 0.694 μm
Energy Multimode TEM_{00} Mode	~100. mJ 1.8 mJ	$\gtrsim$ 1.0 J 1.8 mJ
Longitudinal Mode	Many	Many
Beam Diameter at Output Mirror Multimode TEM_{00} Mode	 5 mm 1 mm	 6 mm 0.75 mm
Polarization	Linear	Linear
Pulse Repetition Rate	1 pps	1 pulse/5 sec
Pulse Duration in TEM_{00} Mode	12 nsec(FWHP) (See Fig. 30)	12 nsec (FWHP)
Pulse to Pulse Energy Reproducibility	± 7%	± 10%

Fig. 2 Surface Damage on $LiNbO_3$ Due to One Pulse from a Multimode Q-Switched Nd:YAG Laser. Average power density ~250 MW/cm^2; dark field illumination.

The list of materials in Table IV, ranked according to their ability to withstand surface damage, was obtained in this initial phase of the work. Clearly the table is incomplete, it represents damage from a "multimode" beam and does not reveal any of the functional dependence of the number of pulses required to damage the surface on the power density. On the other hand, such a list as this is indicative of the differences in resistance to surface damage among non-linear materials. In addition, since the surface quality of KDP, which has the highest resistance to surface damage, was not as good as that of $LiNbO_3$, this compilation also shows that the differences are caused by the material and not the surface finish.

More extensive data was obtained for $LiNbO_3$ and $Ba_2NaNb_5O_{15}$ where we measured the average number of pulses required to produce damage N, as a function of the optical power density on the crystal's surface. The data shown in Fig. 3 was obtained. In this figure the quantities labeled P_α and P_1 are defined as:

P_α is the highest power density of a particular pulse which did not damage the surface of the crystal;* and

P_1 is the lowest power density which will always damage the surface in a single pulse.

Note that by definition

$$P_\alpha \leq P_1 \quad ,$$

and so for values of power density, P between P_α and P_1 the number of pulses required to produce damage will depend upon P. As we shall see in Secs. II-H and I, the most revealing experimentation and theorizing concerns this intermediate range of power densities. At this point, however, it suffices to define these parameters and to point out that the value of P_α, in say MW/cm^2, can be used as a practical measure of a material's resistance to surface damage.

---

* In this stage of the program P_α corresponded to the power density which caused no damage in 500 pulses. This concept is examined further in Sec. II-H in view of the probabalistic interpretation.

TABLE IV

Several Nonlinear Materials Listed in Order of Decreasing Resistance to Surface Damage (Multimode Illumination)

	$P_\infty \left(\frac{MW}{cm^2}\right)$
Potassium Dihydrogen Phosphate (KDP)	> 400
Ammonium Dihydrogen Phosphate (ADP)	> 400
7-Diethylamino-4-Methylcoumarin	400
Coumarin	10
$Ba_2NaNb_5O_{15}$	10
$LiNbO_3$	6

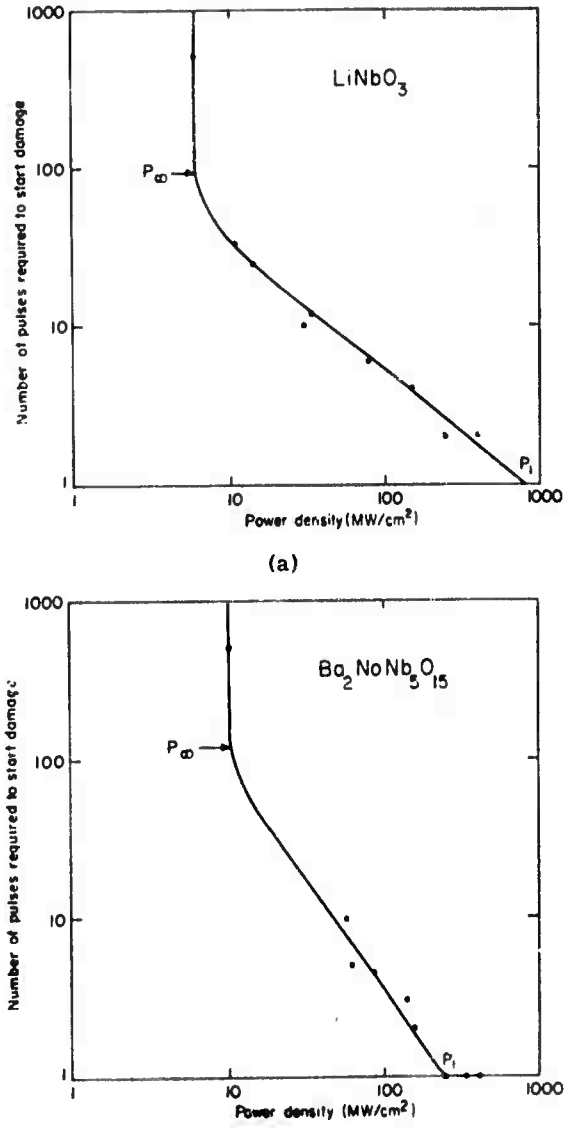

Fig. 3 Measured N = N(P) Using Multimode, Pulsed, Q-switched Nd:YAG Laser.

Since the laser output was varied by varying the flashlamp input in these early experiments, it is possible that the laser mode varied in a systematic manner, resulting in these particular relationships. However, the $LiNbO_3$ damage data described below, which was obtained using the laser-attenuator in Fig. 1, also shows a similar relationship for intermediate values of P through the exact functional dependence is different.

The values of P_α, P_1 and slope, m (see Fig. 3) depend on the beam's transverse mode or, in other words, on the transverse intensity distribution. Using the setup sketched in Fig. 1 where the laser was restricted to the TEM_{00} mode and the power density could be varied without altering either the pulse duration or the polarization state, we found that the value of P_α for $LiNbO_3$ is 350 MW/cm^2 as compared to 6 MW/cm^2 for a "multimode" pulse.* In this case, $P_1 \tilde{=} 1600$ MW/cm^2. The damage pit on $LiNbO_3$ produced by a single pulse of 1.06μm light in a TEM_{00} mode and having P = 1600 MW/cm^2 is shown in Fig. 4. This pit is $\sim 2.7 \times 10^{-2}$ mm in diameter and ~2100 A deep.

Figure 5 shows the measured relationship between N and P for $LiNbO_3$ when irradiated by a pulsed, Q-switched TEM_{00} mode, Nd:YAG laser. The pulse duration was 15 nsec (FWHP) and it was focused to a nearly circular spot of diameter $\leq 3 \times 10^{-2}$ mm. The crystal surface was polished flat to $\lambda/10$ and its smoothness figure was (0,0). It was uncoated and cleaned with lens tissue and methanol after each damage spot occurred. During these experiments the crystal was oriented so that the b axis was normal to the surface and the light polarization parallel to the crystal's axis. Note the similarity in the functional relationships between N and P obtained in the "multimode" and TEM_{00} mode experiments.

Determination of the area irradiated proved to be the major source of error in the measured power densities. Several measurements of this quantity were obtained by direct measurement of the area burned by the focused laser

---

* Note that this is the average power density of the focused TEM_{00} mode beam. At the center the peak power density is at least 2 × the given value.

Fig. 4 Surface Damage on $LiNbO_3$ Due to One Pulse from a TEM_{00} Mode, Q-Switched Nd:YAG Laser. Average power density ~ 1600 MW/cm^2; bright field illumination.

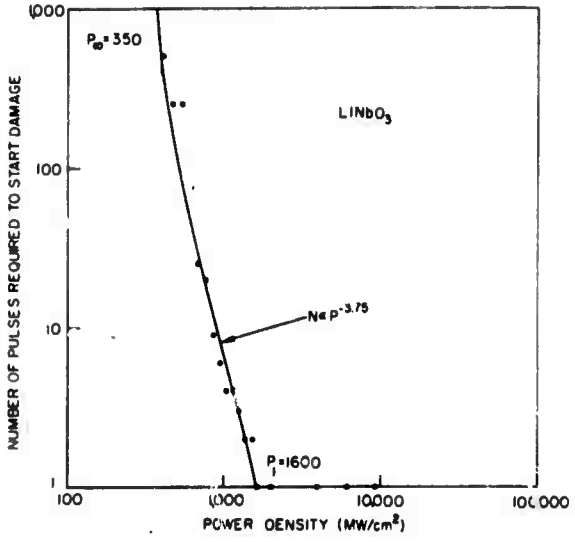

Fig. 5 Measured N = N(P) Using TEM_{00} Mode Pulsed, Q-Switched Nd:YAG Laser.

beam on the surface of several different materials (stainless steel, anodized aluminum, etc.). The area was also calculated from the beam diameter incident on the objective lens and the effective f number. These various determinations agreed reasonably well (± 10 percent) with one another, but in order to be conservative and underestimate the power density, we selected the largest value of the area obtained.

The difference between the values of P_∞ and P_1 using TEM_{00} mode and "multimode" beams can be understood by considering that the peak power density in a "multimode" beam (i.e., in each "hot spot") can be many times the value estimated from the pulse energy, its duration and the total irradiated area. In each hot spot, power densities as high as in a TEM_{00} mode are possible (see Fig. 2), if at least 75 percent of the "multimode" energy is evenly distributed among the several hot spots.

All the preceding measurements were performed at a pulse-repetition frequency of 1 pps, at room temperature, and in air. No noticeable difference was detected in P_∞ for $LiNbO_3$ when the crystal was heated to 200°C or when the ambient atmosphere was N_2, Ar or vacuum.

Since the surface-quality question inevitably arises, we examined the imperfection density per unit area of various crystalline surfaces using large angle X-ray scattering. Even the smallest crystalline misorientation, and any cracks, scratches, or other imperfections, show up as areas of different scattering intensity in this type of measurement. Figure 6 shows these Berg-Barrett X-ray topographs of the polished surface of both a $LiNbO_3$ and a KDP crystal. This procedure enables one to locate surface imperfections and to try to correlate damage pits with these locations. No significant correlations could be found.

These data show that the material, and not the surface treatment alone, accounts for the difference in damage resistance. KDP offers outstanding evidence of this; it cannot be polished finer than $\lambda/4$ and smoother than (10, 20)

2 mm

$LiNbO_3$

KDP

Fig. 6 Berg-Barrett Surface Reflection X-Ray Topographs of Polished Crystalline Surfaces.

but the resistance to damage is the highest yet measured. Improvement in surface quality alone then could improve a given material's resistance to surface damage, but it will not eliminate the differences between materials.

E. Internal Damage Using Optical Microscopy

In the experiments described in II-D the beam was sharply focused on the crystal's surface and only surface damage was noted. However, when the focusing condition was relaxed slightly and/or the beam was focused inside the crystal, internal damage was easily induced. Filamentary damage and internal pitting as well as surface/volume damage were observed following irradiation at levels which in the earlier experiments did not induce surface damage.

To improve the photographic documentation of these types of damage, photomicrographs were made using side-light illumination. In this manner damage tracks as shown in Fig. 7 were seen, which could not otherwise be detected. The crystal was a repolished "hot" $LiNbO_3$* sample from Crystal Technology, Inc. which had previously been used as a frequency doubler and had suffered surface damage. The tracks run from one end of the crystal to the other, are very straight, and contain a series of nearly regularly spaced regions of damage extending ~ 0.04 mm normal to the length of the track. Since these tracks were not observed in other types of inspection and do not correspond to damage purposely induced, it is possible that they or other internal damages are induced at low levels of irradiation and go unnoticed until surface damage occurs. It is even possible that such internal damage might be the precursor to surface damage.

As a consequence of these observations several other surface-damaged $LiNbO_3$ and KDP samples used in the past as Pockel's cells or frequency doublers were examined for internal damage. These crystals had been inspected visually and thought to have suffered surface damage only. In a few cases, in fact, we had the surfaces repolished and had reused the crystal. In all cases, however, within the crystal, in the volume contained between the damaged areas of the surfaces

---

* "Hot" $LiNbO_3$ is a Li rich form of this material which has a higher a axis index matching temperature for 1.06 and 0.53μ than stoichiometric $LiNbO_3$.

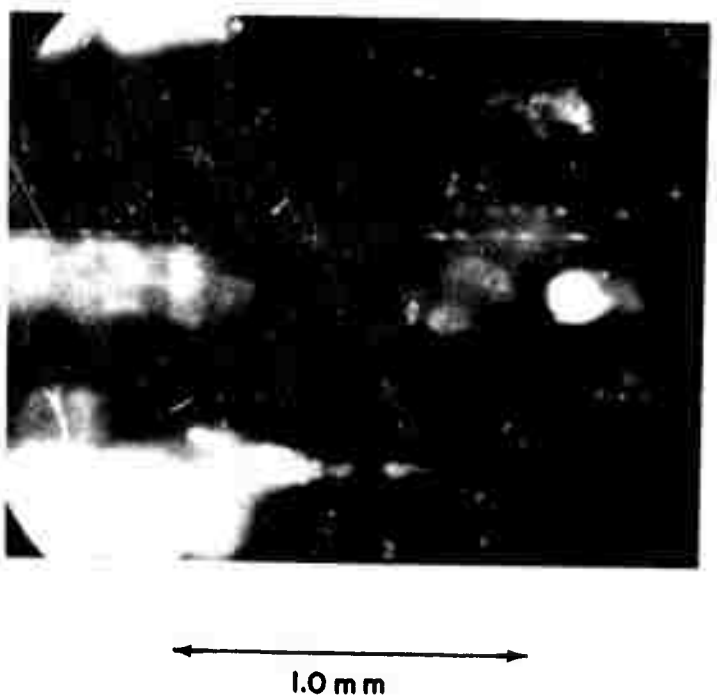

Fig. 7 Faint Filaments Inside $LiNbO_3$ Seen with the Aid of Sidelighting. Large, out-of-focus areas are regions where internal damage was purposely produced.

we found many pits and bubbles and at least one or two of the latter type of tracks (see Fig. 8). Elsewhere the interiors of these crystals are free of any sign of internal damage. It seems, therefore, that internal damage which is not readily detected by the usual inspection procedures does occur in $LiNbO_3$ or KDP. In fact, since the use of each of these crystals was halted at the first sign of surface damage, the internal damage was induced at the same or lower levels of irradiation. To realize the generality of this observation it is important to recall that the 1.06μm beams of light responsible for the damage shown in Figs. 7 and 8 were multimode, unfocused and had pulse durations between 10 and 40 nsec and the crystals were oriented for both Pockels-cell and frequency-doubler operation.

A new $LiNbO_3$ sample[1] was prepared with all six faces polished so that the interior of the material below the irradiated surface could be examined microscopically with both back and side illumination. The damages shown in Fig. 9 were induced with the beam incident along the crystal's b axis and polarized parallel to the a axis.

When the TEM_{00} mode 1.06μm laser is focused on the crystal's surface at high power densities, a small circular pit is formed on the surface and no internal damage is observed. At somewhat lower power (Fig. 9b) densities this type of surface damage is sometimes detected. However, at ostensibly the same power density (Fig. 9c) internal filamentary damage and surface/volume damage where the filamentary damage rises to the surface sometimes occur. At still lower power densities, only internal filamentary damage is detected. These results were obtained using a 7 nsec long pulse (FWHP) as compared to the 15 nsec pulse duration used in the work in Sec. II-D.

The output energy of the laser used in these experiments varied by ± 10 percent from pulse to pulse and so the different types of damage in Fig. 9 induced at 5.3 GW/cm^2 were probably induced by slightly different power densities. However, this level of irradiation is of interest because it represents the value at which the dominant damage mechanism changes. In the case under discussion, the surface damage mechanism dominates at high levels of irradiation while internal filamentary damage just below or reaching the surface is dominant at lower levels.

Fig. 8 Internal Pit and Filamentary Damage in a $LiNbO_3$ Q-Switch Crystal.

Views of $LiNbO_3$ surface on which a TEM_{00} mode Nd:YAG laser was focused (focal spot dia. = 0.003 cm) (pulse duration = 7 nsec)

0.1 mm

Views of the interior below the irradiated area

Power density = 31.0 GW/cm²	= 5.3 GW/cm²	= 5.3 GW/cm²	= 3.4 GW/cm²	= 1.9 GW/cm²
3 shots	1 shot	1 shot	1 shot	1 shot

Fig. 9 Various Types of Laser-Induced Damage.

We found that this change in damage process occurs at 0.84 GW/cm^2 when the irradiated area was four times that in Fig. 9. Therefore, the two experiments yield the same value for the "change-over" power or energy within experimental error. That is, when a small area of $LiNbO_3$ is irradiated by a TEM_{00} mode 1.06μm laser pulse of 7 nsec duration and ~ 0.5 mJ energy content the damage process which dominates may be either that which results in surface damage or that which results in internal filamentary damage.

$LiNbO_3$ frequency doublers and Pockels cells undergo surface damage when irradiated by Q-switched multimode Nd:YAG laser beams of ~ 10 nsec duration and 20-40 mJ total energy. In general, the cross sections of these beams are composed of between 10 and 40 hot spots and so the area of the crystal irradiated by each "hot spot" is subjected to from 0.5 to 4 mJ of 1.06μm light. This is in good agreement with the value obtained above for the level of irradiation at which the dominant damage mechanism becomes that responsible for surface damage. With less energetic but otherwise similar laser beams internal damage which generally goes unnoticed is induced.

Filamentary damage has been associated with the phenomenon of self-focusing where a nonlinear interaction between the light and the medium leads to a local increase in the index of refraction and so focuses the beam.[2,3,4] If the focusing is sufficiently strong, the beam diameter can become so small that diffraction effects become large and a trapped filament may result. The extremely high optical electric fields in the irradiated region might cause electrical breakdown and thereby damage the medium.[2]

When the laser was focused on the entrance face of the crystal the depth to which filamentary damage penetrated was found to be independent of the pulse energy (see Fig. 9) but was inversely proportional to the focal length of the lens. The length of the filament, however, did vary with the incident energy. Since the light entering the crystal under these conditions is divergent, it is reasonable that a short-focal-length lens produces filamentary damage which penetrates deeper than that produced with a long-focal-length lens using the same incident power; the beam must propagate further into the crystal so that self-focusing can result in damaging power densities.

When the lens is focused inside the crystal, one end of the filamentary damage is near the focal point and the filament extends back towards the lens (see Fig. 10). The end near the focal point is small and disappears into the undamaged material while the other end is characterized by a large cracked region having overall dimensions $\simeq 10\times$ the filament diameter. Zverev et al.[5] have observed similar behavior for filamentary damage in sapphire. The overall length of the damage does not increase substantially when several pulses are fired into the same region. However, the cracked end becomes larger and more cracks appear. The overall length of the filamentary damage varies with the pulse energy, power, or power density. As demonstrated in Fig. 11, this relationship is found to be approximated quite closely by a power law where damage length is proportional to energy or peak power or power density. Note that, due to self-focusing, it is impossible to give the power density inside the medium; therefore the pulse duration, energy and the focusing conditions assuming linear optics are specified separately.

A crystal of KDP which had previously been used to frequency-double a Nd:YAG laser and which was thought to be surface-damaged was repolished for use in this work. It was found that when the TEM_{00} mode Nd:YAG laser was focused on the surface, damage was initially produced inside the crystal at a power density of $\sim 2.7\ GW/cm^2$ and no damage at all could be produced at $\sim 0.24\ GW/cm^2$. At intermediate levels of irradiation, internal damage sometimes could be produced in one pulse and sometimes several pulses were required. Upon examination of this sample with the microscope, however, many cracked and pitted regions were found at or just below the surface which did not correspond to those which were induced on purpose. These are the remains of the so-called surface damage which was supposedly removed upon repolishing. These residual damages are completely invisible to the naked eye and so generally pass unnoticed. Their presence, however, is responsible for the erratic results obtained and demonstrates that surface and volume damage occur at almost the same levels of irradiation in KDP as well as in $LiNbO_3$.

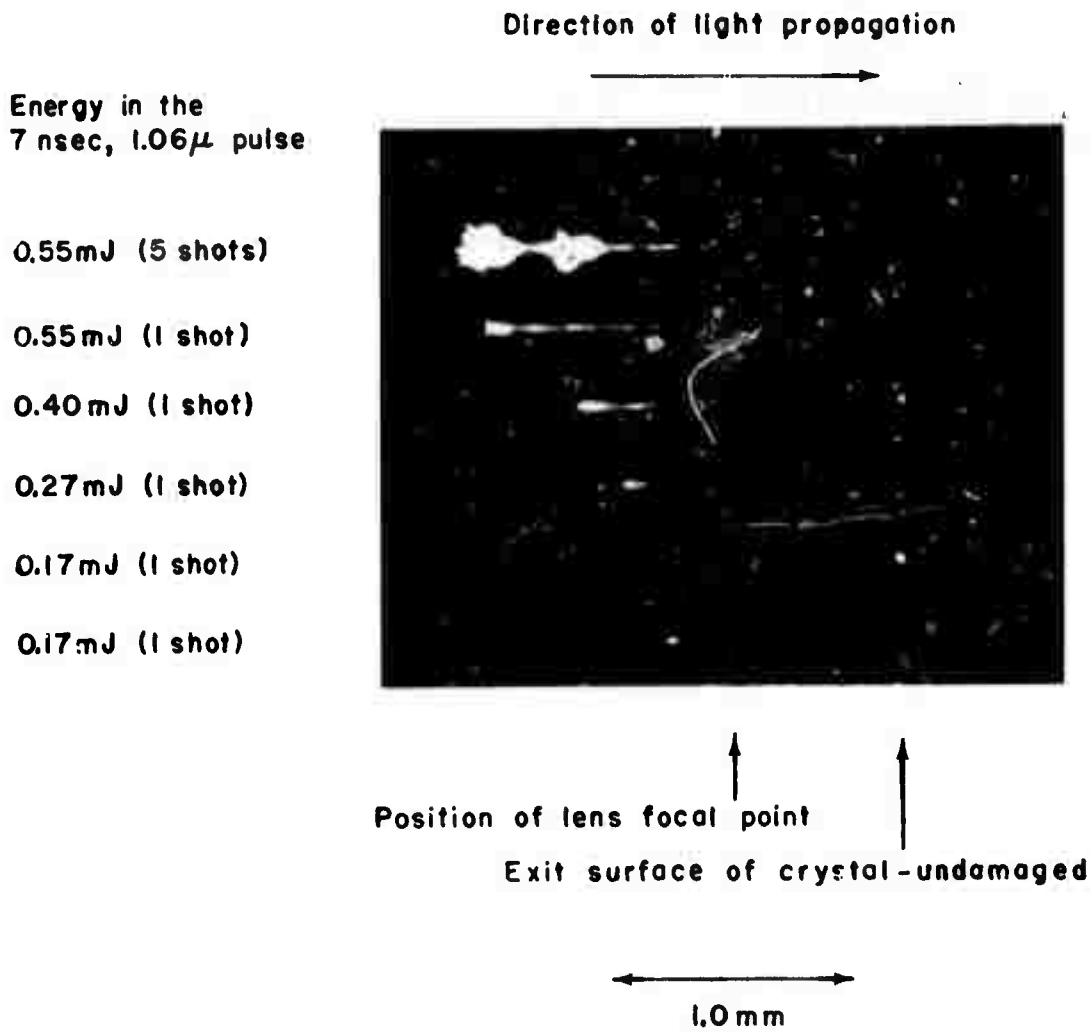

Fig. 10 Filamentary Damage in $LiNbO_3$ When Light is Focused Inside the Crystal but Near the Exit Surface.

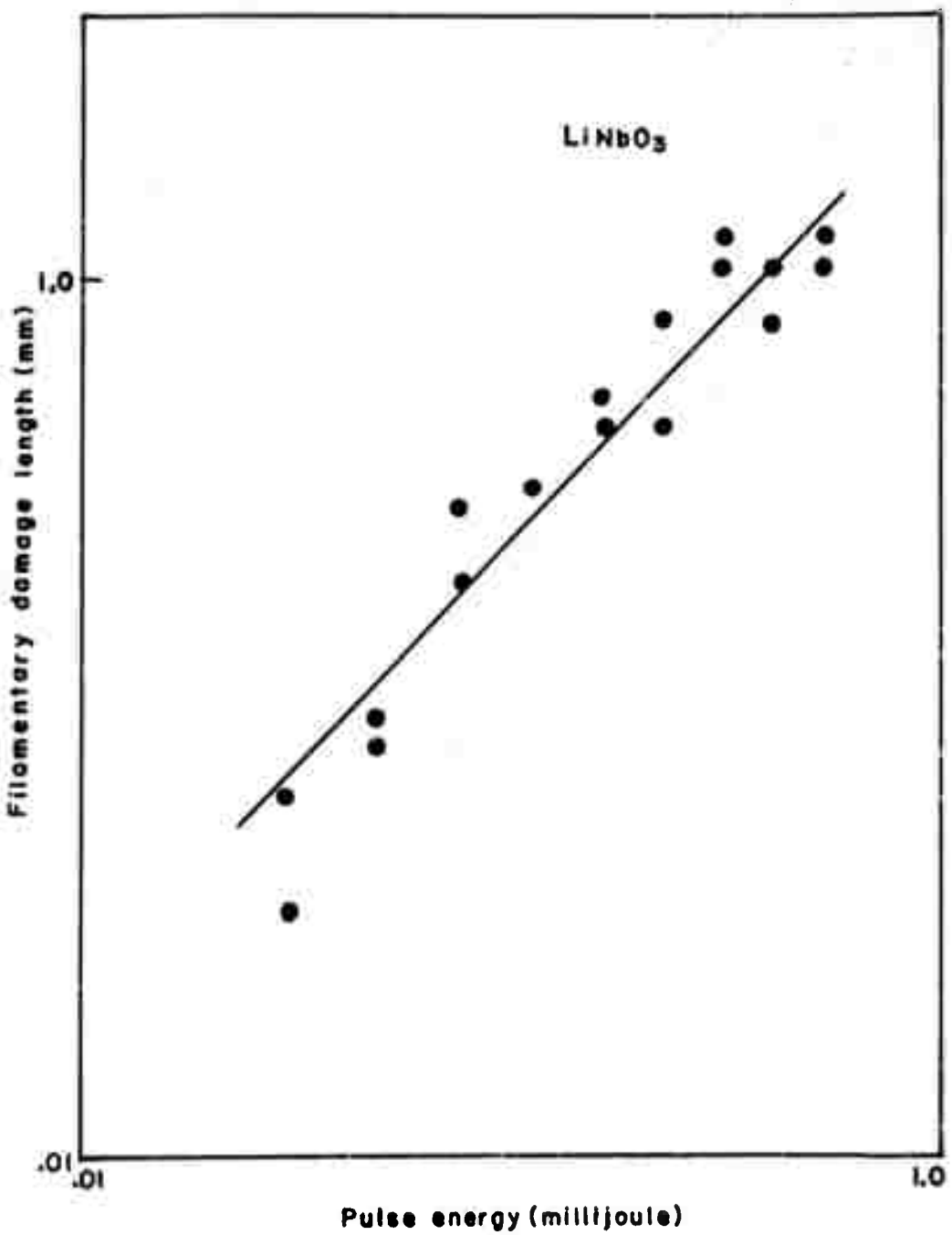

Fig. 11 Filamentary Damage Length Versus Pulse Energy Where the 1.06 μm TEM_{00} Mode Laser is Focused Inside the Crystal. Pulse duration = 7 nsec. If there were no self-focusing, the focal diameter would have been 0.006 cm.

One very practical outcome of this work stems from the fact that any sample which shows surface damage is very likely also damaged internally; thus, a repolished sample is not as good as one which has never been damaged. This holds both for samples used in damage studies and as frequency-doubler or Pockels-cell crystals.

F. Scanning Electron Microscope Studies of Residual Damage

1. Surface damage

Guiliano et al.[6] recommended the use of the scanning electron microscope in the study of laser-induced surface damage to ruby crystals. Following their suggestion, a scanning electron microscope (SEM) was used to examine laser-induced damage to $LiNbO_3$ with more resolution and magnification than could be obtained from the best optical microscopes.

Two SEM micrographs of the surface damage shown in Fig. 12 were taken at slightly different electron-beam incidence angles and a stereo view assembled. In this manner it was discovered that in profile the damage initially rises sharply above the undamaged surrounding area, then slowly falls down towards the center where a small, deeper depression is found. With such a profile, a surface pit should more properly be called a crater!

The outer diameter of the damage in Fig. 12 is approximately equal to the focal diameter used to irradiate the crystal. In the surrounding region many microscopic particles are found which seem to have been ejected from the crater. Though the laser was operated in the TEM_{00} mode and would thus have irradiated a circular area, the crater is slightly irregular and smooth. This suggests the possibility that the material composing the crater wall was at one time molten and flowed into this shape. In Appendix A a measurement of the absorption in $LiNbO_3$ at 1.06μm is described, and the value of absorptivity is found to be too small to account for melting. An additional process such as a rapid increase in absorptivity with temperature or the formation of a hot plasma which in turn causes the damage must be involved.

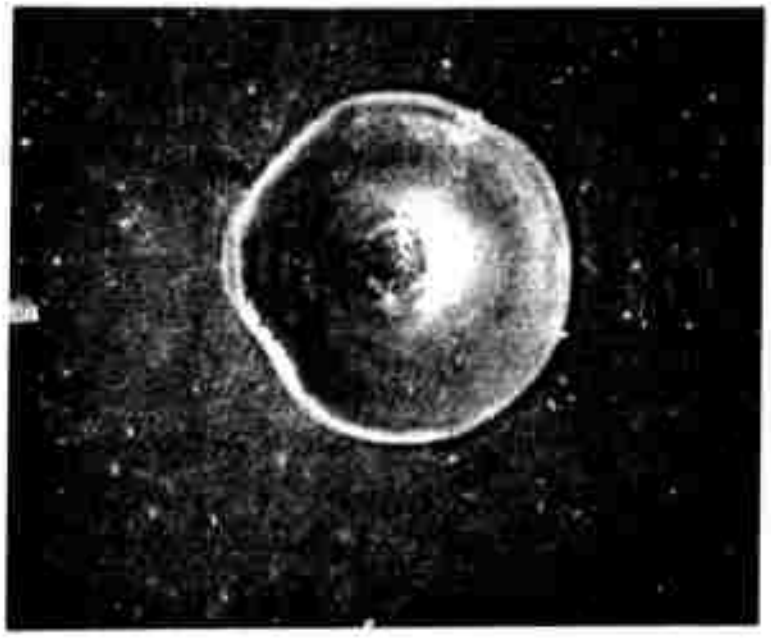

↔

0.001 cm

Electron beam incidence angle surface normal

0°

↔

0.0002 cm

45° from left to right

Fig. 12 Entrance Surface Damage to $LiNbO_3$ when TEM_{00} Mode 1.06μm Laser is Focused on the Entrance Surface. Focal dia. = 0.006 cm; pulse duration = 7 nsec; pulse energy = 0.26 mJ. S.E.M. micrographs.

Figure 13 shows the surface damage caused by the same pulse used to achieve the damage in Fig. 12, but focused to a diameter one-half as large. Note that the damage crater has a similar profile (rising first and then falling), the surrounding area is littered with ejected matter and the crater diameter is again approximately that of the irradiation.

The damage in Fig. 14 was caused by three 1.5 mJ pulses applied at one-second intervals. Otherwise the irradiation was identical to that used in Fig. 13. The many small (more microscopic) pits surrounding the crater are probably caused by molten particles ejected from the interior of the crater falling back onto the surface. In the case of Fig. 13, most of these particles were either too small or too cool to melt into the crystal. Instead, as seen in that figure, they lie on the surface. In this case, as in Figs. 12 and 13, no internal damage can be detected by optical means in the region under the crater.

Figure 15 shows a case of surface/volume damage in $LiNbO_3$ obtained with a 0.17 mJ pulse of 7 nsec duration. Note the very different character of this damage when compared to that in Figs. 12 - 14. The surface layers have been physically lifted off and large pieces have been ejected. A filamentary damage region is seen at the center of the outwardly radiating cracks. When very highly magnified and overexposed, the SEM micrograph at the bottom of Fig. 15 reveals that this filamentary damage is not hollow.

In the regions nearest the filament there is material that seems to have been molten and to have re-solidified. Apparently a melting process occurs in this case as well as in Figs. 12 - 14, but is obscured by the much larger destruction which results when the filamentary damage reaches the surface. Since the thermal expansion coefficients of $LiNbO_3$ are very anisotropic,[7] it is possible that following internal heating, the surface layers were highly strained and so broke off.

The SEM micrographs in Fig. 16 shows that the type of damage observed on the exit face when the lens is set to focus through the material and on the exit

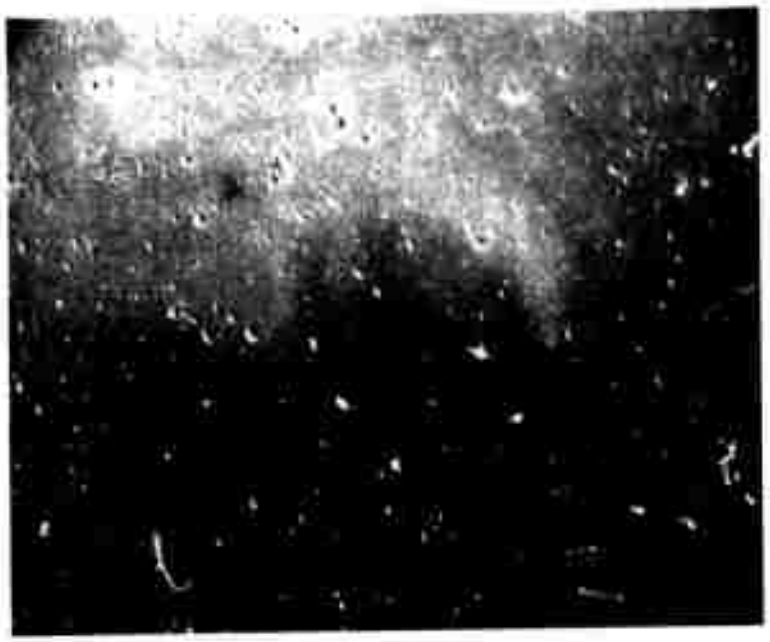

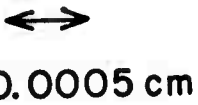

Fig. 13 Entrance Face Surface Damage to $LiNbO_3$ when TEM_{00} Mode 1.06 μm Laser is Focused on the Entrance Face. Focal dia. = 0.003 cm; pulse duration = 7 nsec; pulse energy = 0.26 mJ. S.E.M. micrograph. Electron beam incident from left to right at 45° to the surface normal.

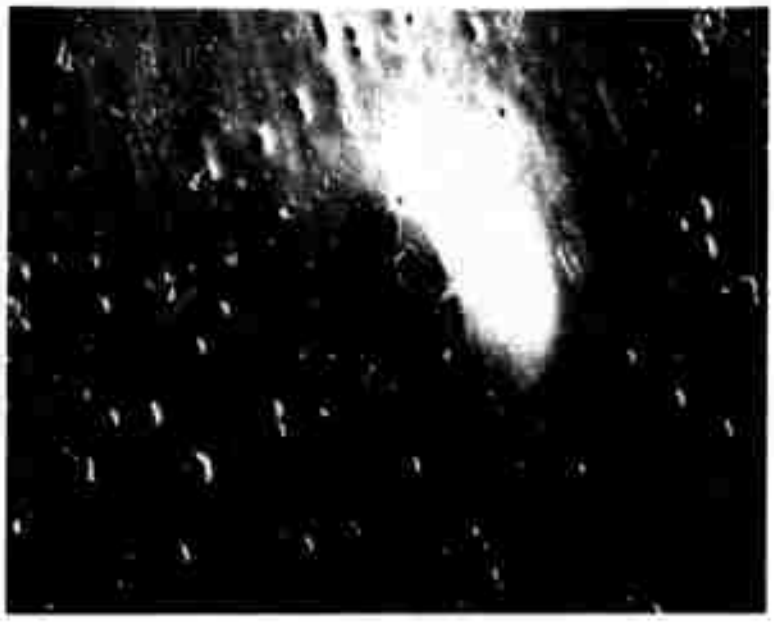

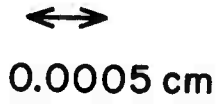

Fig. 14 Entrance Face Surface Damage to $LiNbO_3$ when TEM_{00} Mode 1.06 μm Laser is Focused on the Entrance Face. Focal dia. = 0.003 cm; pulse duration = 7 nsec; pulse energy = 1.5 mJ; 3 shots. S.E.M. micrograph. Electron beam incident from left to right at 45° to the surface normal.

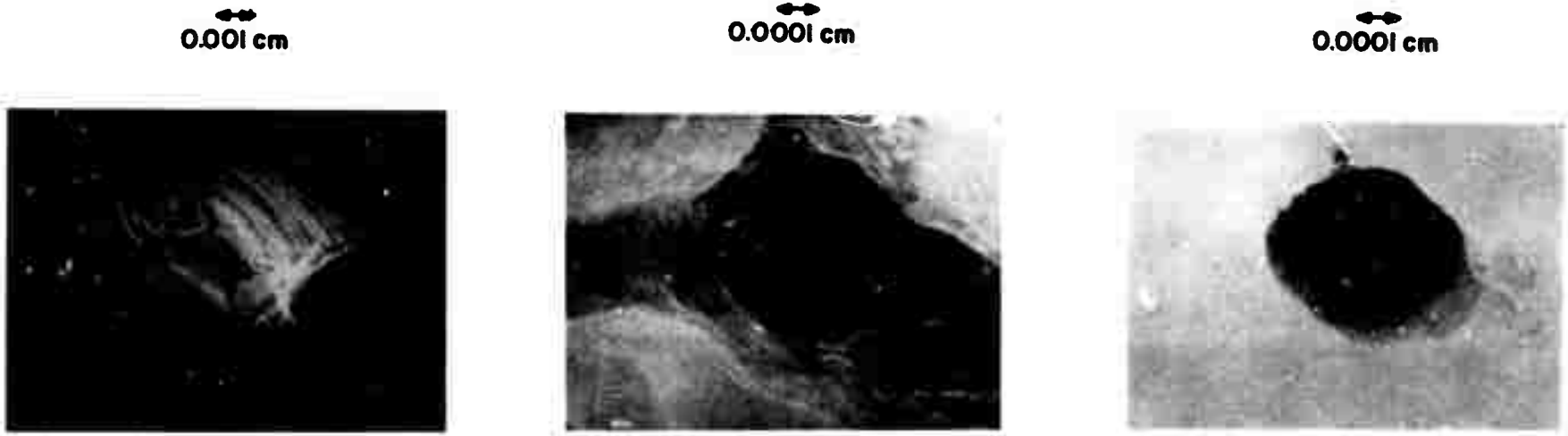

Fig. 15 Entrance Face Surface Damage to $LiNbO_3$ where an Internal Filamentary Damage Reached the Surface. The TEM_{00} mode 1.06 μm laser was focused on the entrance face to a dia. = 0.006 cm S.E.M. micrographs with electron beam incident normal to the surface.

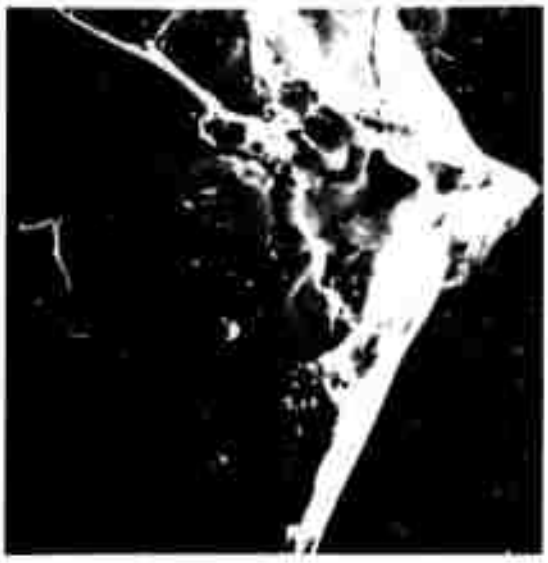

PBN-447

0.001 cm

Fig. 16a Entrance Face Damage to $LiNbO_3$ when TEM_{00} Mode 1.06 μm Laser is Focused on the Entrance Face.

0.001 cm

Fig. 16b Exit Face Damage to $LiNbO_3$ when Same Lens as Used Above is Set to Focus the Same Pulse as Used Above on the Exit Face.

Focal Dia. = 0.006 cm; pulse duration = 7 nsec; pulse energy = 0.26 mJ. S.E.M. micrographs with the electron beam incident normal to the surface in both a and b.

face is very different from that induced when the light is focused on the entrance face. The character of exit face damage, as seen in Fig. 16, is the result of a damage mechanism which is complicated by the beam's propagation through the medium: Self-focusing effects must be included in the analyses of laser-induced damage whenever the light enters the medium.

The form of damage induced by a ruby laser in materials which do not absorb at 6943 or 3471 Å is very similar to that produced by a Nd laser. When sharply focused a ruby laser pulse produces surface damage only; when the focusing condition is relaxed, the damaged regions extend into the volume of the sample. Results obtained for ruby laser-induced damage are described in Sec. II-H after the concept of damage probability is introduced.

2. Internal filamentary damage in $LiNbO_3$

Internal filamentary damage in $LiNbO_3$ was studied in more detail with the scanning electron microscope by polishing the sample in order to expose the damage. The sample was oriented so that the plane of the polishing lap was parallel to the long axis of the damage and material was removed in ~ 5μm steps. This process was continued until no damage material remained.

Optical observations before polishing into the damage indicated that, in addition to a central tube of damaged material, there were several long, thin cracks lying parallel to the filament and oriented so that they could intersect. When the edges of these cracks had been exposed, the scanning electron microscope was used to measure their width; they were between 0.3 and 0.5μm wide. The polishing process did not reveal any central tube of damaged material in either optical or electron micrographs. It is therefore concluded that the damage tube observed optically before polishing is the overlapping diffraction pattern of the lines of intersection of the several cracks.

The preceding conclusion is supported by the fact that the diameter of the "central damage tube" when measured with an optical microscope was

found to depend nearly linearly on the focal-length-to-aperture ratio (the f number) of the objective lens used. This result can be understood by recognizing that the apparent dimensions of a small object (i.e., one having dimensions on the order of an optical wavelength) when viewed through an optical device are primarily determined by diffraction effects. In particular, it is easy to show that the apparent diameter of a line source of true diameter D is closed approximated by

$$D_{app} = (1 + 1/M)\, 2\lambda F + D \quad ,$$

when viewed in light of wavelength λ through a lens having magnification M and f number, F. In the present experiments $M \geq 10$, $\lambda \approx 0.5\mu m$, ≥ 6 and $D \approx 0.4\mu m$, so that

$$D_{app} \propto F \quad ,$$

is the expected result.

G. Dynamic Properties of Laser-Induced Damage

The sparks which can be seen both inside and on the surface of transparent media when damaging pulses of light pass through, lie along the beam axis and are bright enough to be photographed with an image converter streak camera. Fersman and Khazov[8] report that the temperature of an entrance surface spark produced by a Q-switched ruby laser on K-8 glass is initially in excess of 8000°K, certainly bright enough to be photographed and hot enough to cause damage. Since residual damage in solids is found only where and after sparks were observed, these sparks are either coincident with or the direct cause of the damage.

In this work, a TWR STL Products Model 1D image converter camera with streak plug-in units 7B or 5B was used to photograph the temporal development of the laser-induced sparks. A pulsed Q-switched Nd: YAG laser which

could produce multimode pulses of energy up to 75 mJ and duration of ~ 15 nsec (FWHP) was the damage light source. The peak of the laser pulse was reached in 7 - 8 nsec. So that the mode pattern and pulse waveform would be nearly constant, the laser was always pulsed at 1 pps and with the same total input energy. The energy incident on the lens used to focus the light into the sample (the "damage" lens) was controlled with the polarizer attenuation described in Sec. II-C. A small part of the laser output was removed with a beam splitter and frequency doubled. Several components, constituting an optical path less than 1 nsec longer than that of the 1.06 μm beam, aimed the green light parallel to the camera axis and focused in the plane containing the damage. The image of this light provides a reference on the streak photo as to the time when light entered the medium. Coupled with the pulse waveform, this streak permits one to determine which part of the pulse caused a particular spark. The experiment is diagrammed schematically in Fig. 17.

Figure 18 shows the formation of sparks in and on the entrance face of lucite acrylic plastic using two different lenses. To avoid confusion of the green light streak with streaks due to sparks, the green light was spatially offset from the line of the sparks by the indicated distances. When this offset is subtracted, these data show that the first internal spark to occur in Fig. 18a begins at the same instant that the leading edge of the 1.06 μm pulse arrives at the lens focus and that all the sparks are initiated within the 7 - 8 nsec required for the pulse intensity to reach its maximum. No sparks are initiated at later times. Similar results are obtained in Fig. 18b using a different focusing lens. These photos show conclusively that, when the light is focused inside the medium, the sparks are formed sequentially beginning with those nearest the focal point and ending with those nearer the lens. This result is also obtained in other transparent solids and liquids.

When the light is focused 0.123 cm inside the plastic sample, an internal spark at the focus is the only one to appear at the lowest input which always results in a breakdown. As the pulse energy is increased, more internal sparks appear until at ~ 6× this input an entrance surface spark is also produced. The delay between the arrival of light at the focus and the beginning of the first spark decreases with increasing pulse energy.

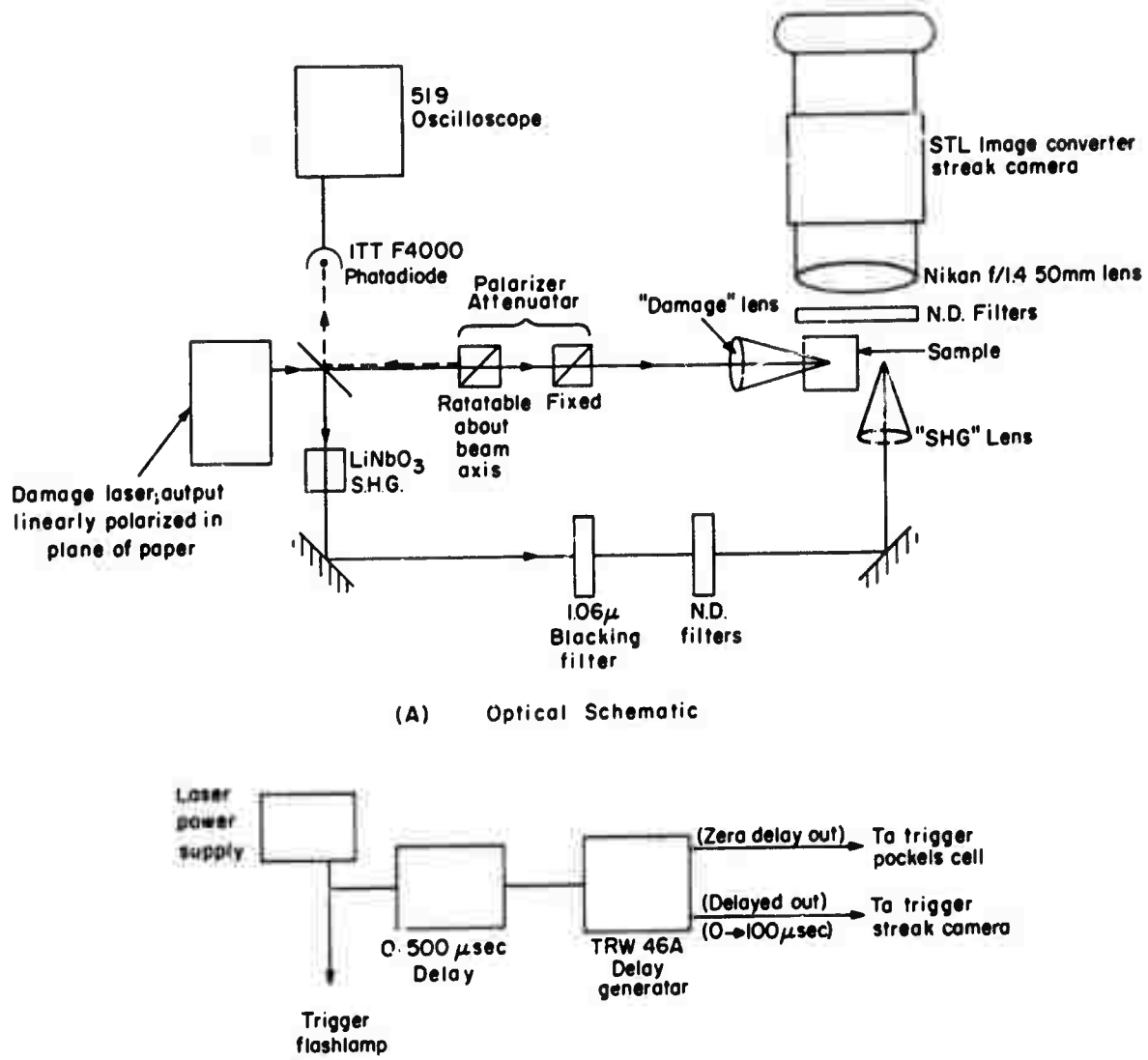

Fig. 17 Schematic Diagram of Streak Camera Experiment.

a. Optical
b. Electrical

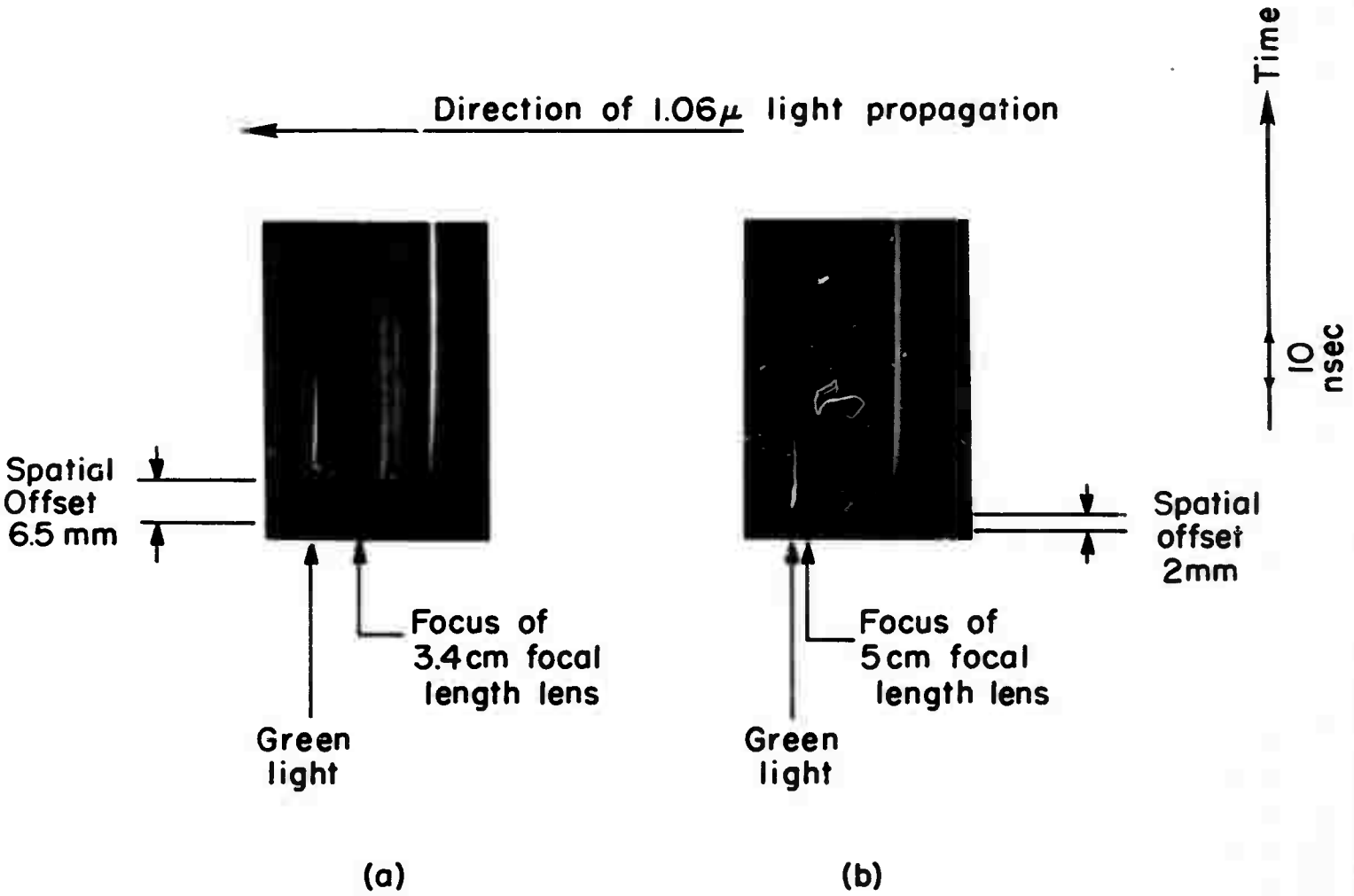

Fig. 18 Streak Photographs of Laser-Induced Sparks in Lucite Acrylic Plastic. In (a) a 3.5 cm focal length lens was used; in (b) a 5 cm focal length lens was used. The focus was set to produce both internal and surface sparks.

Exit surface damage can be produced by focusing through the sample and on the exit face. At the lowest input which always produces breakdown, only exit surface breakdown is observed while at higher energies internal sparks are also produced. Figure 19 shows these sparks in acrylic plastic.

Figure 20a shows breakdown produced when a 20 mJ multimode 1.06μm pulse is focused in air. This spark begins ≈ 3 nsec after the first light arrives at the focus. The spark in Fig. 20b is formed when a plastic sample is placed 0.25 mm downstream from the focus. It begins nearly coincidentally with the arrival of the 1.06μm light, and its growth to the right (i.e., upstream) takes place over a time interval nearly 2× that in Fig. 20a. In Fig. 20c sparks are formed both within and on the entrance face with the light is carefully focused on this surface. The difference between the sparks in these photos shows that the surface breakdown which leads to damage is dependent on the presence of the material and is not due to breakdown in the ambient gas.

In order to study the fact that sparks were produced only when the laser intensity was increasing in more detail, the laser cavity was lengthened from 50 to 185 cm to produce pulses having structure as shown in Fig. 21c and total duration on the order of 100 nsec. The lengthened laser output was 29 mJ.

Figure 21a shows the relative spatial position of the green light and the line of sparks when the 3.4 cm focal length lens was used to damage plate glass. The first spark to occur, as shown in Fig. 21b, began at t_1, 14 nsec after the first light arrived at the focal point. In agreement with the results obtained with the smooth pulse above, comparison of the time coordinate for the formation of sparks in Fig. 21b with the pulse waveform in Fig. 21c shows that sparks are formed only during intervals of time when the level of irradiation increases. On the other hand, when the pulse energy or intensity is high but nearly constant, or increasing slowly, for example between t_2 and t_3, no new sparks are formed.

A qualitative model which explains these results can be constructed by requiring that self-focusing of the beam precede the initiation of an internal breakdown, that the self-focusing process is very fast, say with response time

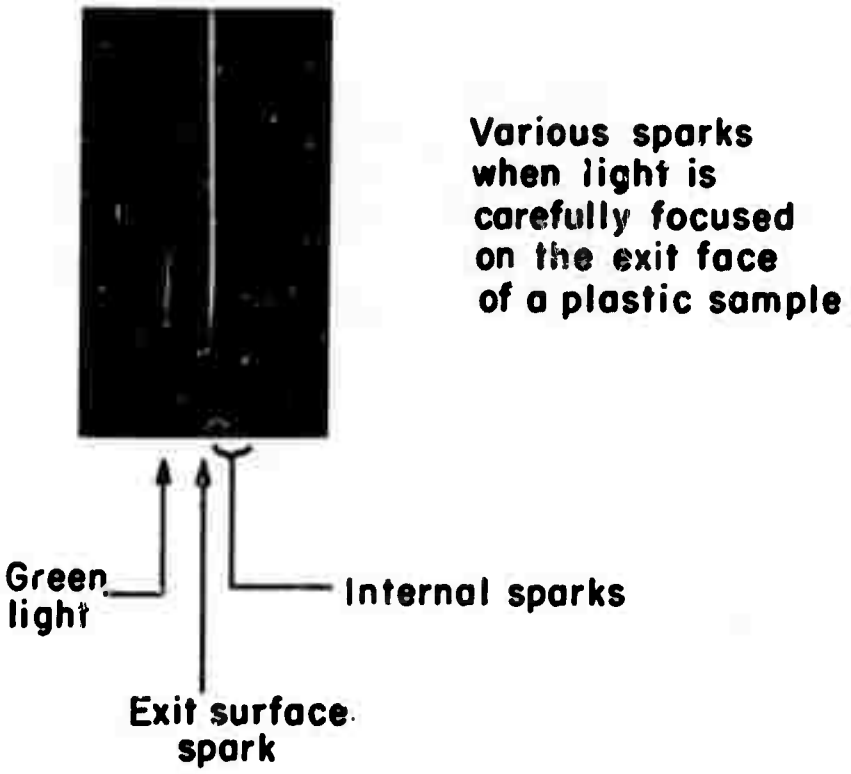

Fig. 19 Breakdown on the Exit Face of an Acrylic Plastic Sample. The laser was focused through the sample and on the exit face.

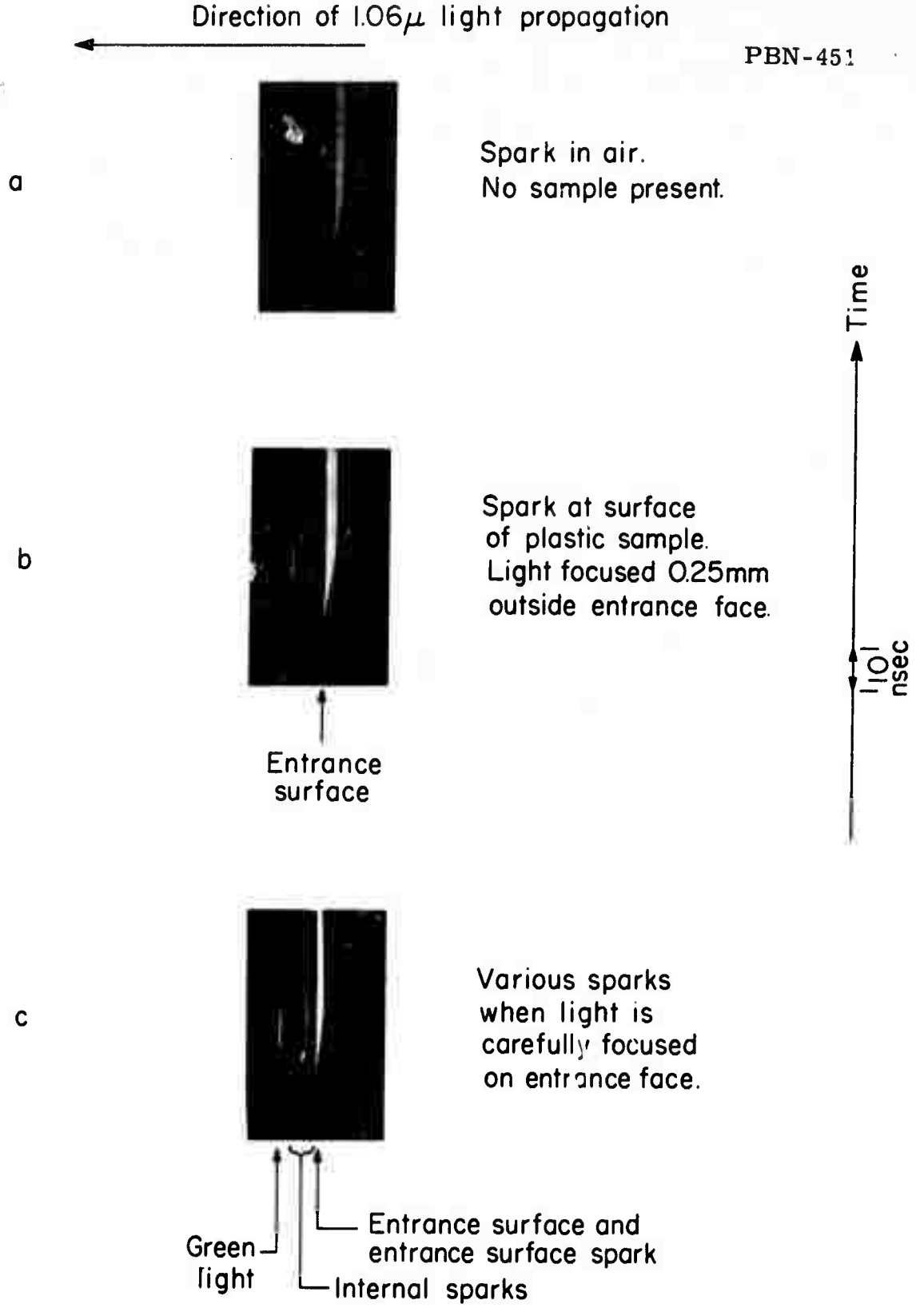

Fig. 20 Breakdown on the Entrance Face of a Acrylic Plastic Sample.

a. Breakdown in air with no sample present.
b. Breakdown near the surface of the sample. The focus was 0.25 mm outside the entrance face.
c. Breakdown when focused on the sample's entrance face. Note internal sparks are also produced.

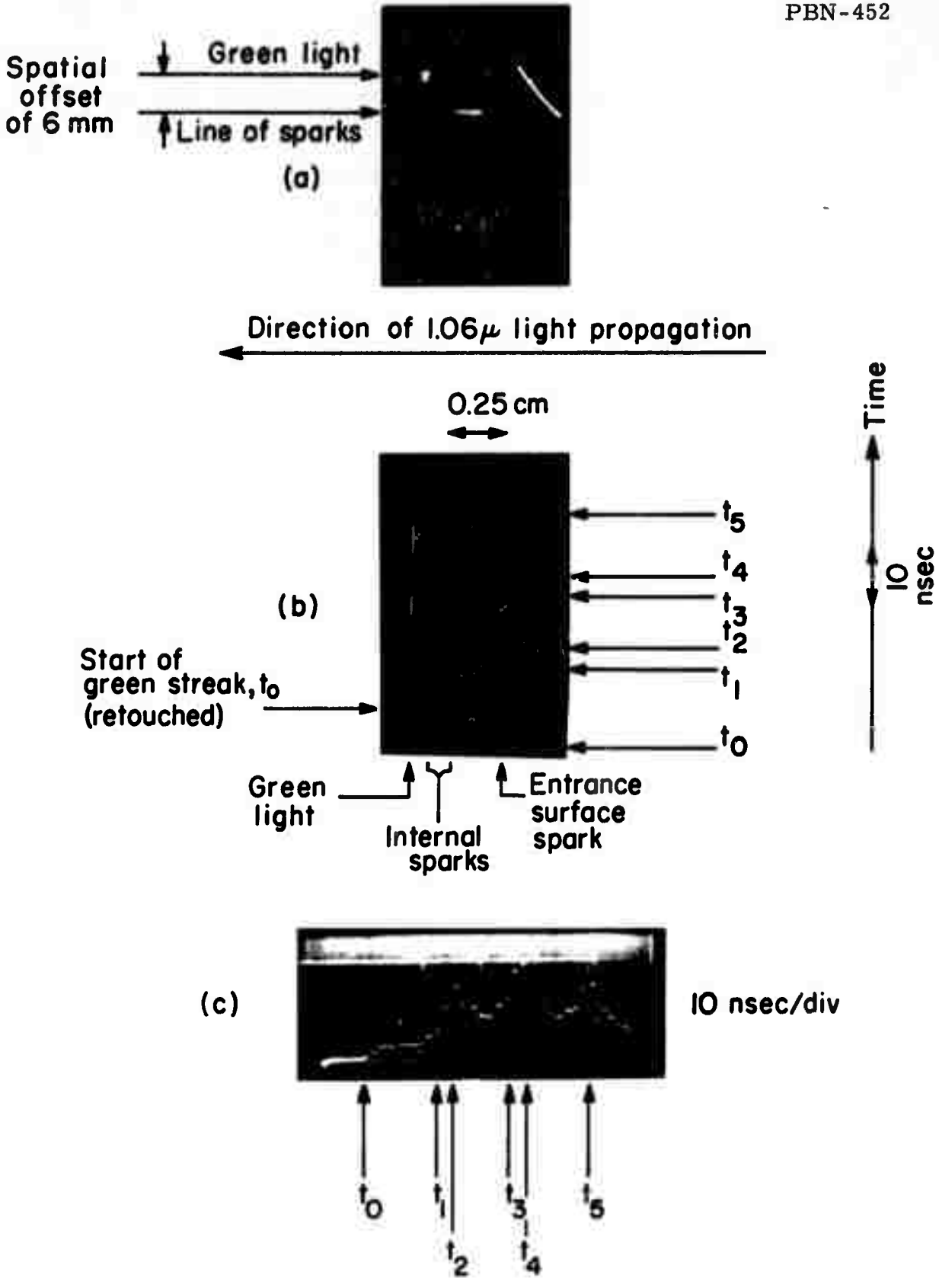

Fig. 21 Streak Photographs of Laser-Induced Sparks in Plate Glass.
a. Unstreaked sparks and green light
b. Streaked sparks and green light
c. Waveform of the pulse which produced the sparks in (b). Arbitrary vertical scale.

$\lesssim 10^{-10}$ sec, and that the focus moves upstream with increasing intensity. A fast self-focusing process can follow changes in the pulse intensity and give rise to the sequences of focusing conditions sketched in Fig. 22 for a smooth pulse and in Fig. 23 for a "wiggly" pulse. The beam focus can be in undamaged material only when the pulse intensity increases, implying that new breakdown can occur only during these intervals.

The requirement that self-focusing in solids have a fast response time is satisfied in glass as the measurements of Duguay et al.[9] have demonstrated. Theoretical calculations of the movement of the beam focus in Sec. IV agree with the qualitative picture given above. These considerations also show that the form and extent of the movement is dependent on the initial power density and geometrical parameters of the beam. In fact, no moving focal point is found for a collimated 1.06μm, TEM_{00} mode, beam of ~0.6 mm diameter and ~700 MW/cm^2 power density. These conditions were satisfied in an experiment, and the results are shown in Fig. 24. There is no sequential ordering to the initiation of sparks which is what one would expect if there were no moving focal point. However, once again all the breakdowns are initiated during the first 8 nsecs of the pulse's duration suggesting the possibility that the light which arrives later cannot penetrate the existing sparks to produce new breakdowns.

Note that in spite of the absence of self-focusing internal damage in plastic at 700 MW/cm^2 is easily produced, while at this level of irradiation and using the sharply focused beam geometry as in Sec. II-H, it is unlikely that one would ever see surface damage. This implies that it is easier to produce a breakdown within a material than on its surface. Viewed in terms of the avalanche mechanism, discussed in Sec. III, there are more chances for an avalanche to grow to breakdown when a large volume of material is irradiated. If impurity sites are important in providing the electron which starts the avalanche, then this statement is more readily understood. The sample was cut from a commercially available piece of 4 ft. × 8 ft. sheet plastic and so is not a material from which impurities were rigorously excluded. Thus, studies of the probability for internal damage in more controlled materials are planned to resolve this question.

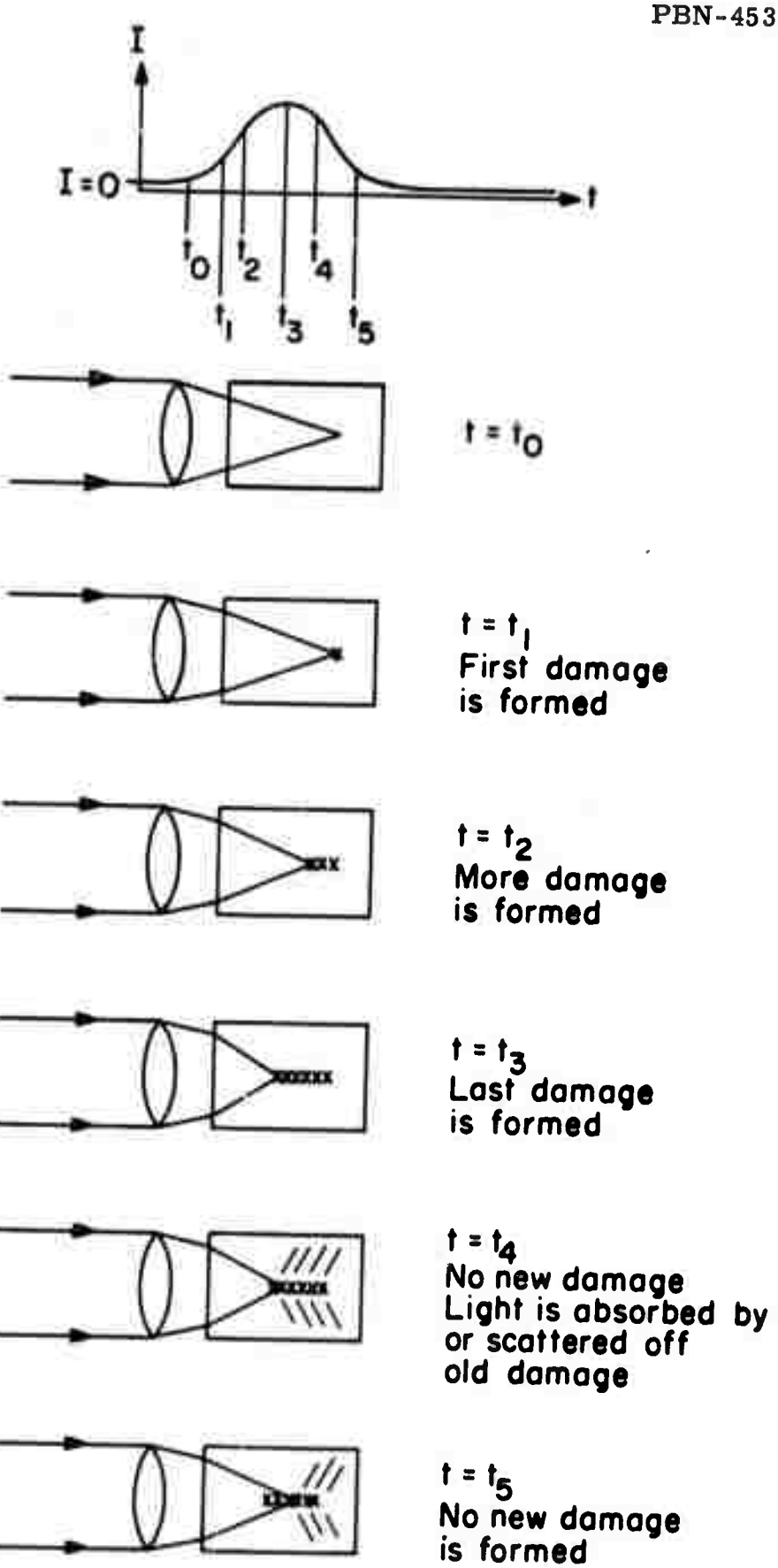

Fig. 22 Sketch of the Sequence of Breakdown Formation Assuming a Fast Response Self-Focusing Process and a Smooth Pulse Waveform.

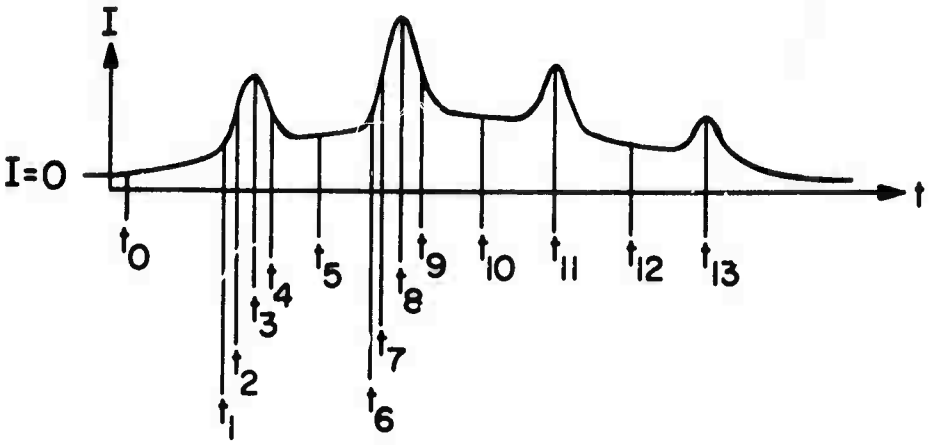

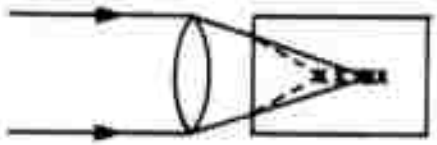

$t_1 \leq t \leq t_3$
Damage is formed

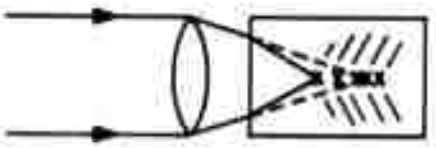

$t_3 < t < t_6$
No new damage
is formed

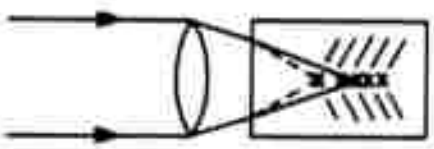

$t_6 \leq t < t_7$
Focus moves upstream
but no new damage
forms until it passes
the damage formed at t_3

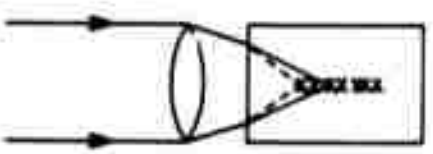

$t_7 \leq t \leq t_8$
New damage is formed

At later times no new damage
is formed unless $I(t) > I(t=t_8)$

Fig. 23 Sketch of the Sequence of Breakdown Formation Assuming a Fast Response, Self-Focusing Process, and a "Wiggly" Pulse Waveform.

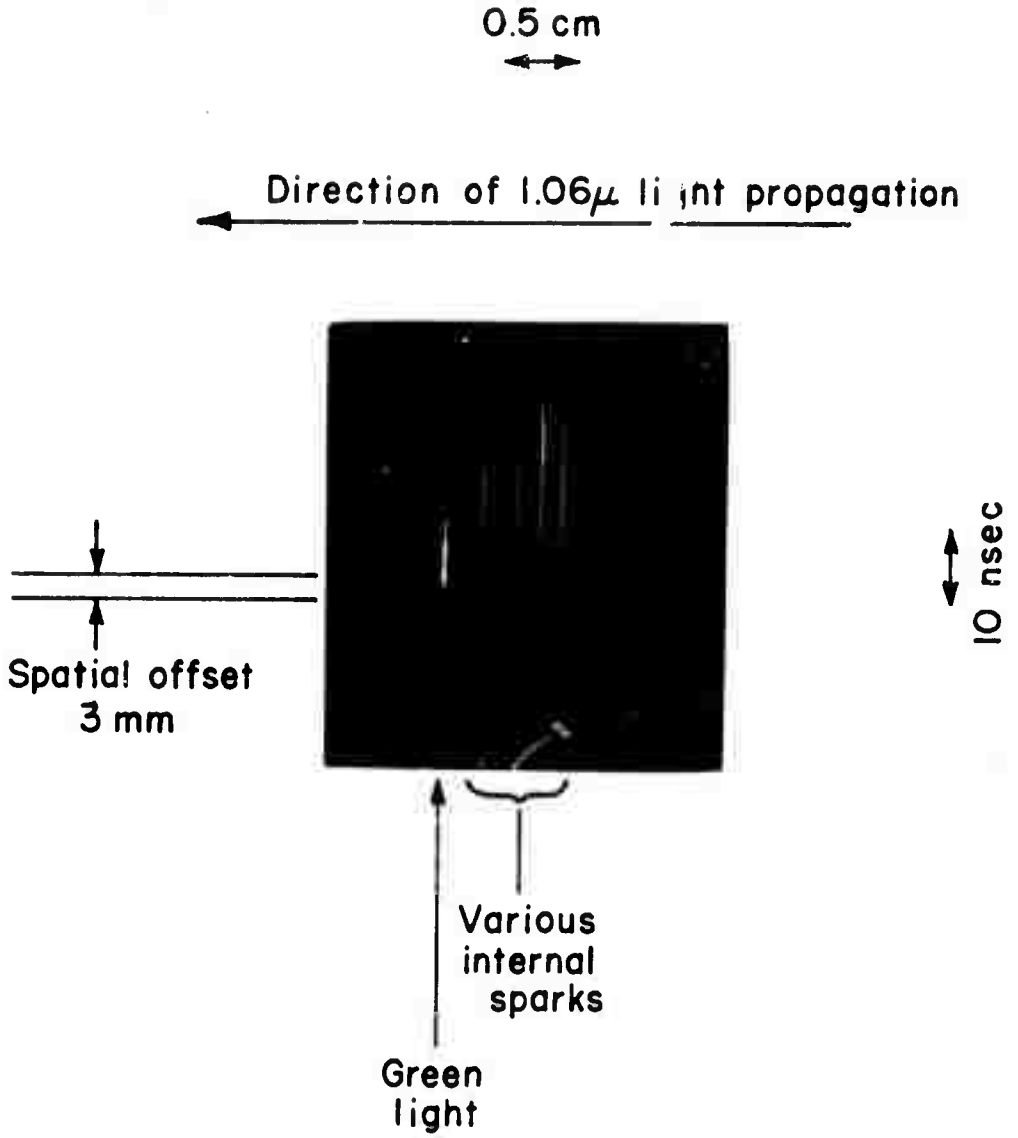

Fig. 24 Streak Photo of Laser-Induced Breakdown in a Plastic Sample Using a Collimated TEM_{00} Mode Laser Beam. The pulse waveform was not completely smooth. Pulse power density 700 MW/cm^2.

Additional information about laser-induced breakdown can be inferred from the length of time during which visible radiation is emitted by the spark. The radiant energy emitted by such a hot body in general rises rapidly as the spark is formed and then falls over a much longer period of time according to the cooling law for the particular type of spark and medium. Within limits determined by its spectral sensitivity and the level of initial exposure, the streak camera can be used to measure the time interval during which a spark radiates. This provides useful information about the mechanisms available to dissipate the energy contained in the various sparks. Since the sparks in liquids can cool by expansion as well as by radiation and conduction, the shortest lived sparks are found in water and 1,2-dichloroethane where they typically do not exceed 70 nsec in duration. On the other hand, the same laser pulse produced internal sparks in plastic and glass having duration between 500 and 2000 nsec. Entrance surface sparks sometimes lasted as long but generally were about 300 - 6000 nsec in duration. Exit surface sparks did not exceed 300 nsec duration.

H. Measurements of the Probability for Laser-Induced Surface Damage

In Sec. II-D, Figs. 3 and 5 show the number of pulses required to damage $LiNbO_3$ and $Ba_2NaNb_5O_{15}$. Upon re-examination of these data it was realized that the measurements could be more readily understood if one accepted the notion that the number of pulses required to damage was in fact a measure of the probability for a pulse of that particular power density to induce damage in the material. Therefore, a new series of experiments was performed using the techniques described in Sec. II-D to measure the probability for damage as a function of power density for several materials.

The experimental setup is described in Secs. II-C and D. Throughout the present series of experiments the following parameters were maintained constant:

Laser and laser wavelength: Nd:YAG with $\lambda = 1.064\,\mathring{A}$ or
Ruby with $\lambda = 0.6943\mu m$

Laser mode: TEM_{00}, linearly polarized

Pulse waveform: Nearly smooth and symmetric with $\tau = 12$ nsec (FWHP)

Pulse repetition rate: 1 pps for Nd:YAG and 1 pulse/5 sec for ruby

Focusing conditions: A 10× microscope objective was used to focus the the beam to a circular spot of diameter, d, $\simeq 0.003$ cm for Nd:YAG and $\simeq 0.0025$ cm for ruby. With this beam geometry the damage was confined to the material nearest the entrance surface.

Sample temperature: Room temperature

Ambient atmosphere: Room air except for the hygroscopic samples which were maintained in a dry nitrogen atmosphere.

All the surfaces studied were polished to the best optical finish which could be obtained, not coated and carefully cleaned following procedures appropriate to the particular material. The glass and plastic samples, however, had lower-quality inspection finishes but were kept clean and free of dust particles during these experiments.

The samples were irradiated at the indicated rate until the spark which coincides with the occurrence of damage was observed. The observer then checked for the presence of residual damage with a 100× microscope. The number of pulses, N, required to damage was noted and then the sample was moved so that undamaged material could be studied. At each power density about 25 different measurements of N were made and the probability for damage by a single pulse taken to be

$$p_1 = \frac{\text{number of damages}}{\Sigma N} \quad . \tag{1}$$

When no damage could be found after 500 pulses, the sample was moved and irradiated again. If this occurred five times in succession, the sequence of events was taken to indicate that $p_1 < 0.0004$. As discussed in more detail below, the sequence of N values obtained was used as a check on the constancy of the experimental parameters.

The main experimental error in measuring the power density was incurred in determination of the focal spot diameter. The true value of the focal spot diameter is felt to be within ± 5 percent of that used. Other errors enter in measuring the pulse energy and duration, so that the power density measurements herein are estimated to be accurate to ± 20 percent. Note that the average, not peak, power density is computed when one divides pulse energy by τ and $(\pi/4)d^2$. Measurements of damage probability are limited at low probabilities by one's endurance in counting pulses which do no damage. At high probabilities, when damage occurs within 1 or 2 pulses, several errors of one pulse in counting the pulses required to cause damage can result in a substantial change in the value of p_1. To obtain a measure of the error in p_1, several measurements were made of a p_1 in the vicinity of 0.01. The standard deviation of these values from their mean was ~25 percent.

The data plotted in Fig. 25 shows the measured probability that one of our laser pulses damages the surface of several materials. It is clear from these data that at any power density there is always some probability that a single pulse will induce damage. Now consider the probability, p_N, that damage be produced by the N^{th} pulse. If p_1 is the constant probability that a single pulse produces damage, then p_N is given as

$$p_N = (1 - p_1)^{N-1}(p_1) \quad . \tag{2}$$

This is simply the compound probability that there be exactly N-1 nondamaging pulses followed by one which causes damage. If a large number of measurements of the number of pulses required to cause damage are made, the fraction of the total number of measurements in which N pulses were observed is a measure of p_N. If the measured probability distribution and that predicted by Eq. (2) using the measured value of p_1 agree then one can conclude that the probability for damage was p_1 for each pulse. This also means pulses of light were constant throughout the experiment and that the irradiated areas of the material were all equivalent. Figure 26 shows the results obtained for fused quartz irradiated by 17.9 GW/cm^2 pulses. Under these conditions p_1 = 0.16 and 99 measurements of N were made in order to obtain the experimental distribution.

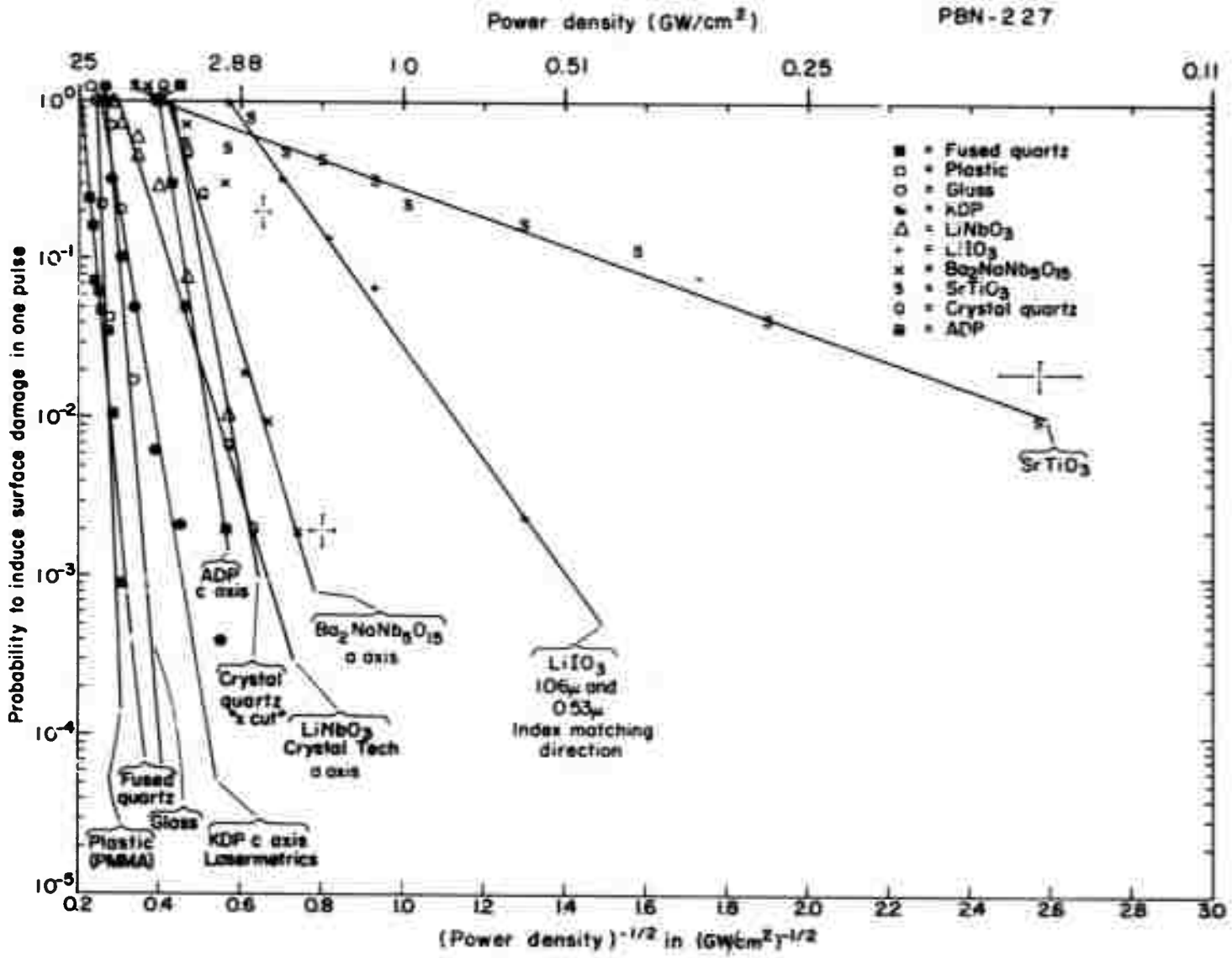

Fig. 25 Plot of the Logarithm of Damage Probability Versus the Reciprocal Square Root of the Power Density on Lower Abcissa and Versus Power Density on the Upper. An Nd:YAG laser was the irradiation source. Since the lower abcissa is proportional to the reciprocal of the electric field, this plot serves to test for a dependence of the form $p \sim \exp(-\text{const}/E)$.

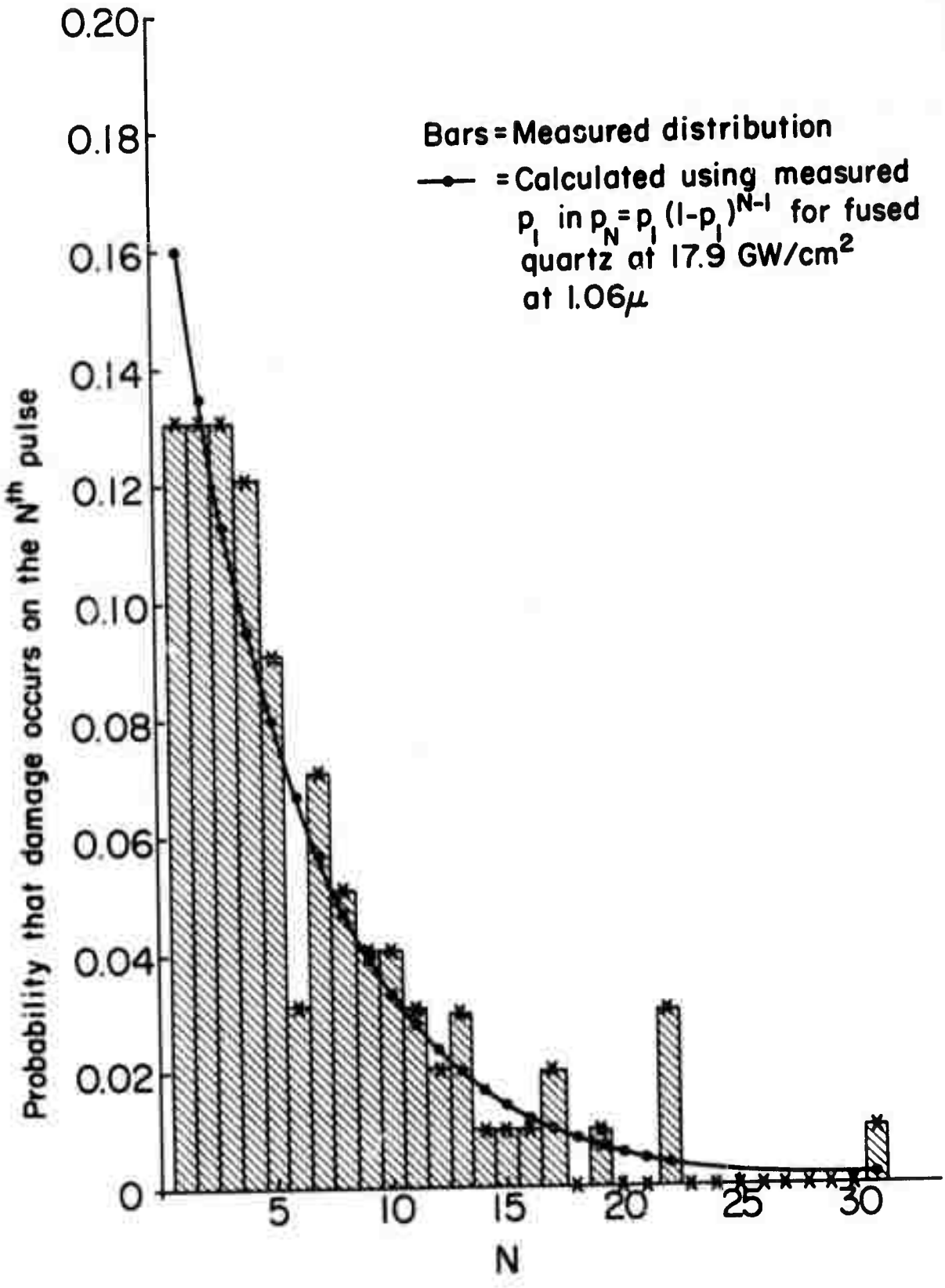

Fig. 26 Probability that Damage Occurs on the Nth pulse Versus N for the Fused Quartz. A 17.9 GW/cm^2 TEM_{00} mode 1.064 μm beam was used.

It is evident from the analysis and data above that it is quite possible to have one sample of one material be damaged by one number of pulses and another, identical sample be damaged by another. In fact, for power densities where p_1 is small ($p_1 \lesssim 0.01$) the probability for not causing damage in N-1 pulses is large,[10] therefore $p_N \approx p_1$ for many values of N, and it is highly likely that measurements of N will yield many widely different results. Having made measurements of N at this level of irradiation one must then examine the distribution of N values in order to be certain that p_1 remained constant throughout the experiments.

Consider the data shown in Table V. The $LiNbO_3$ crystal studied in this experiment was obtained from the Union Carbide Company,[11] and was the only sample to show any extreme difference between the measured distribution and that calculated from p_1. Light was incident along the c axis of this sample. At 3.15 GW/cm^2, the material withstood 500 or more pulses four times in a set of 25 measurements. The other 21 times, damage was achieved in the first few pulses. Since the data in Fig. 26 lends strong evidence to the notion that any laser pulse was almost identical with any other, these data suggest that this sample was not the same everywhere. If the four sets of 500 non-damaging pulses are included, then one finds $p_1 = 0.01$. Among the 25 measurements, however, there are too many low values of N and too many at values of $N > 500$ for the set of 25 N values to be considered a valid sample of the distribution $p_N = (0.99)^{N-1}(0.01)$. If the four measurements of no damage after 500 or more pulses are considered to represent an unusually damage-resistant material and the other 21 measurements are considered as representative of a more easily damaged main component of the sample then, for this component, $p_1 = 0.35$. The distribution of these 21 values of N_1 though obtained from a small number of samples, is close to that predicted by $p_N = (0.65)^{N-1}(0.35)$. Therefore we conclude that this sample of $LiNbO_3$ contains regions which are more resistant to laser-induced damage than the rest of the material. Initial measurements show that the dimensions of these regions can be ~ 1 mm. The bulk of this sample, however, has slightly higher damage probability at a particular power density than that shown in Fig. 25 for light incident along the a axis of a $LiNbO_3$ sample obtained from Crystal Technology, Inc.

TABLE V

Raw Data for Surface Damage to $LiNbO_3$ as a Function of Power Density*

Power Density GW/cm^2	Number of Pulses Required to Cause Damage												
> 10.4	1	1	1	1	1	1	1	1	1	1	1	1	1
8.3	1	1	1	1	1	1	1	1	1	1	1	1	1
6.4	1	6	128	2	2	1	1	1	1	2	1	1	2
3.2	4	2	2	2	2	1	2	2	2	10	4	3	2
1.15	6	6	None in 500	6	4	None in 500	None in 500	None in 500	None in 500	None in 500			

Power Density GW/cm^2	Number of Pulses Required to Cause Damage											
> 10.4	1	1	1	1	1	1	1	1	1	1	1	1
8.3	1	1	1	1	1	1	1	1	1	1	1	1
6.4	1	1	2	1	1	1	1	1	1	1	1	1
3.2	None in 500	5	3	None in 500	None in 500	2	None in 500	2	3	3	2	2

* Light was incident along the c axis. The crystal was prepared by Union Carbide Co.

Table VI lists two operationally interesting levels of 1.06μm irradiation for several materials. One is P_1, the lowest power density at which the probability for damage in a single pulse is unity, as defined in Sec. II-D. The other is called P_{2500} and is a power density at which 500 pulses induced no damage in five successive trials. This sequence of events strongly suggests a very low probability for damage.

An improved experimental arrangement was introduced to permit graphical recording of both the laser pulses and the occurrence of damage. One pen of a dual-pen chart recorder was driven with a signal proportional to the laser pulse energy and the other pen monitored the intensity of a beam of light transmitted through the region which was exposed to the laser pulses. This arrangement, shown in Fig. 27, was sensitive to the appearance of surface damage craters ≈ 0.003 cm in diameter, the smallest damage produced. A typical recording, derived from this arrangement, is shown in Fig. 28 where a ruby laser at ≈ 9 GW/cm^2 was used to irradiate an x-cut crystalline quartz sample. Note the ± 10 percent laser pulse energy variation. The first pulse to strike the sample is marked with an arrow and the 99th pulse, marked with a star, is the one which produced damage. This is indicated by the sharp reduction in the transmitted monitor intensity. The laser trigger signal was picked up by the photomultiplier and so results in a fiducial marker on the record of the transmitted light intensity.

The data in Fig. 28 shows that at this level of irradiation the sample does not have to damage when exposed to any particular pulse. In fact, preceding the damaging pulse (No. 99), there were several more energetic pulses which, according to the "threshold point of view," should have been the ones to cause damage.

In Fig. 29 the results of damage probability measurements for $LiNbO_3$, crystalline quartz and KDP using ruby laser irradiation are shown in comparison with data obtained with the Nd:YAG laser. This comparison reveals that the dominant damage mechanism appropriate to $LiNbO_3$ using ruby irradiation is

TABLE VI

Two Power Densities of Interest: P_1 = Lowest Power Density at Which Damage Always Occurs in a Single Pulse

P_{2500} = A Power Density Where the Probability for Damage In a Single Pulse is Less than 0.0004*

Material	P_1	P_{2500}
Fused Quartz	24.0 GW/cm^2	8.3 GW/cm^2
Plastic	16.1	11.0
Glass	14.4	6.7
KDP	14.4	2.1
$LiNbO_3$	11.1	2.0
ADP	6.4	2.0
Crystal Quartz	6.4	1.2
$Ba_2NaNb_5O_{15}$	6.4	1.2
$SrTiO_3$	6.4	0.08
$LiIO_3$	3.2	0.37

* P_1 for fused quartz is obtained by extrapolating the data plotted in Fig. 25. All other values are measured. Note that P_{2500} is not necessarily the power density at which $p_1 = 0.0004$.

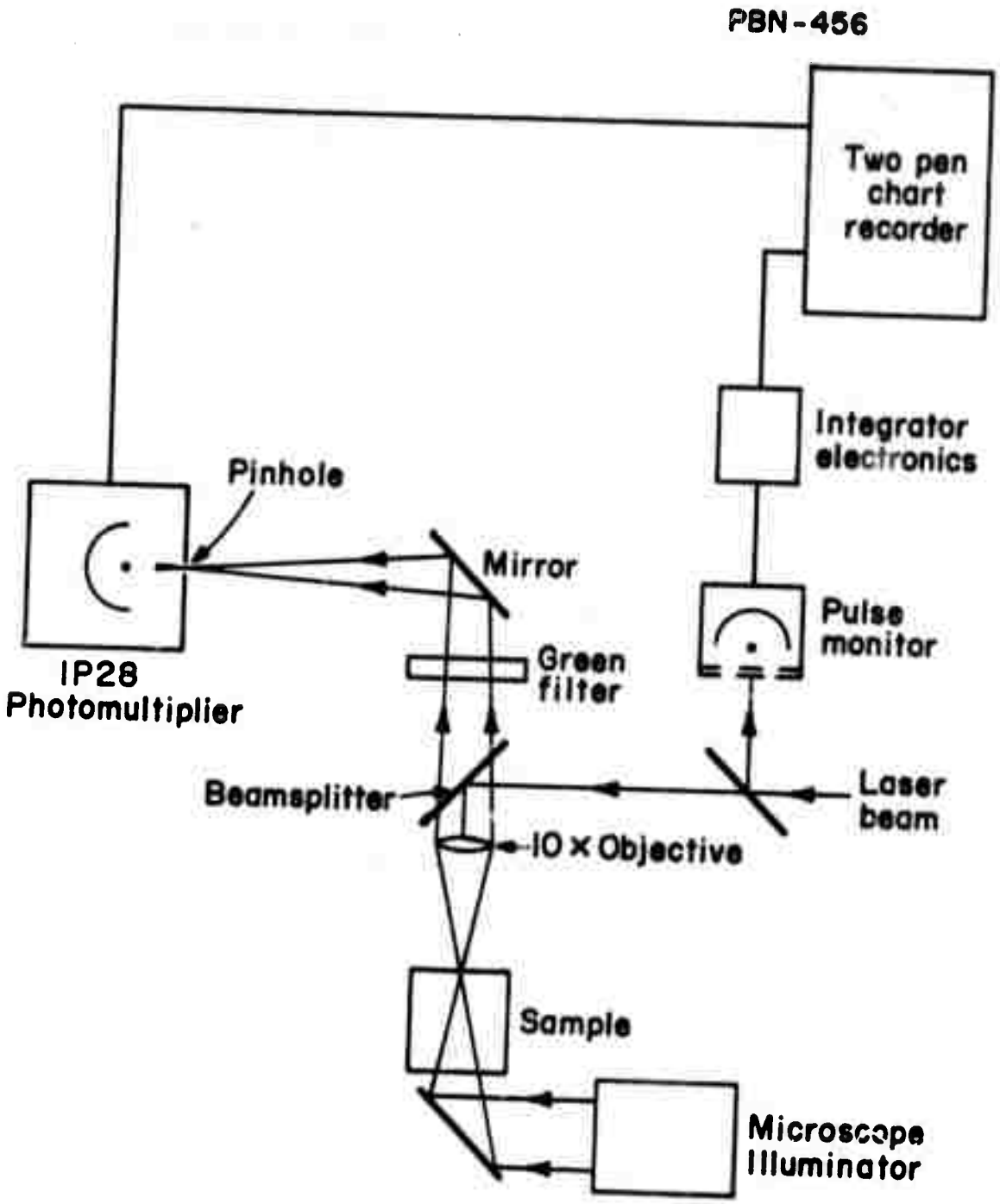

Fig. 27 Schematic Diagram of Automatic Pulse and Damage Monitoring Apparatus.

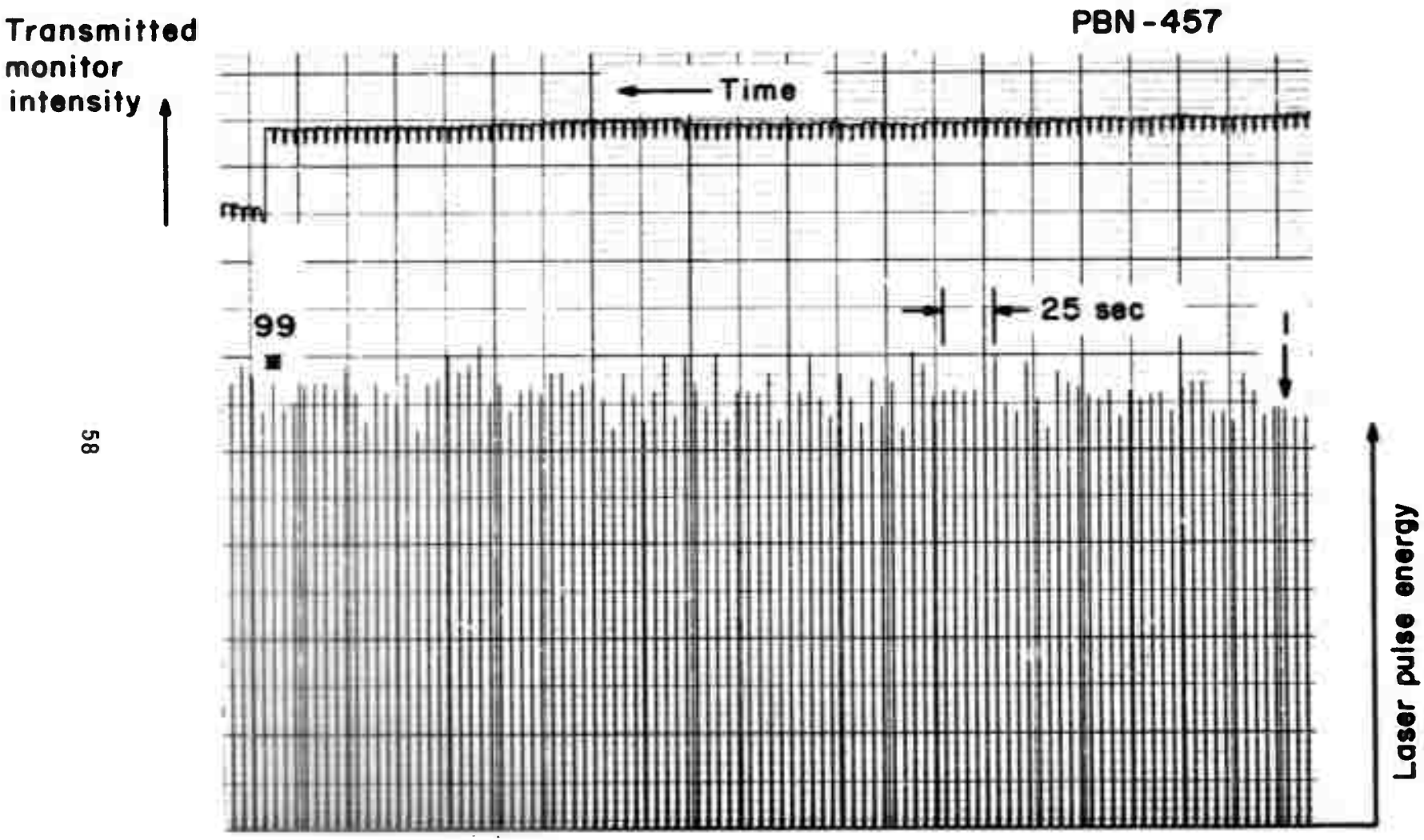

Fig. 28 Record of Exposures of X-Cut Crystalline Quartz to Pulses of Ruby Laser Light at ~ 9 GW/cm^2.

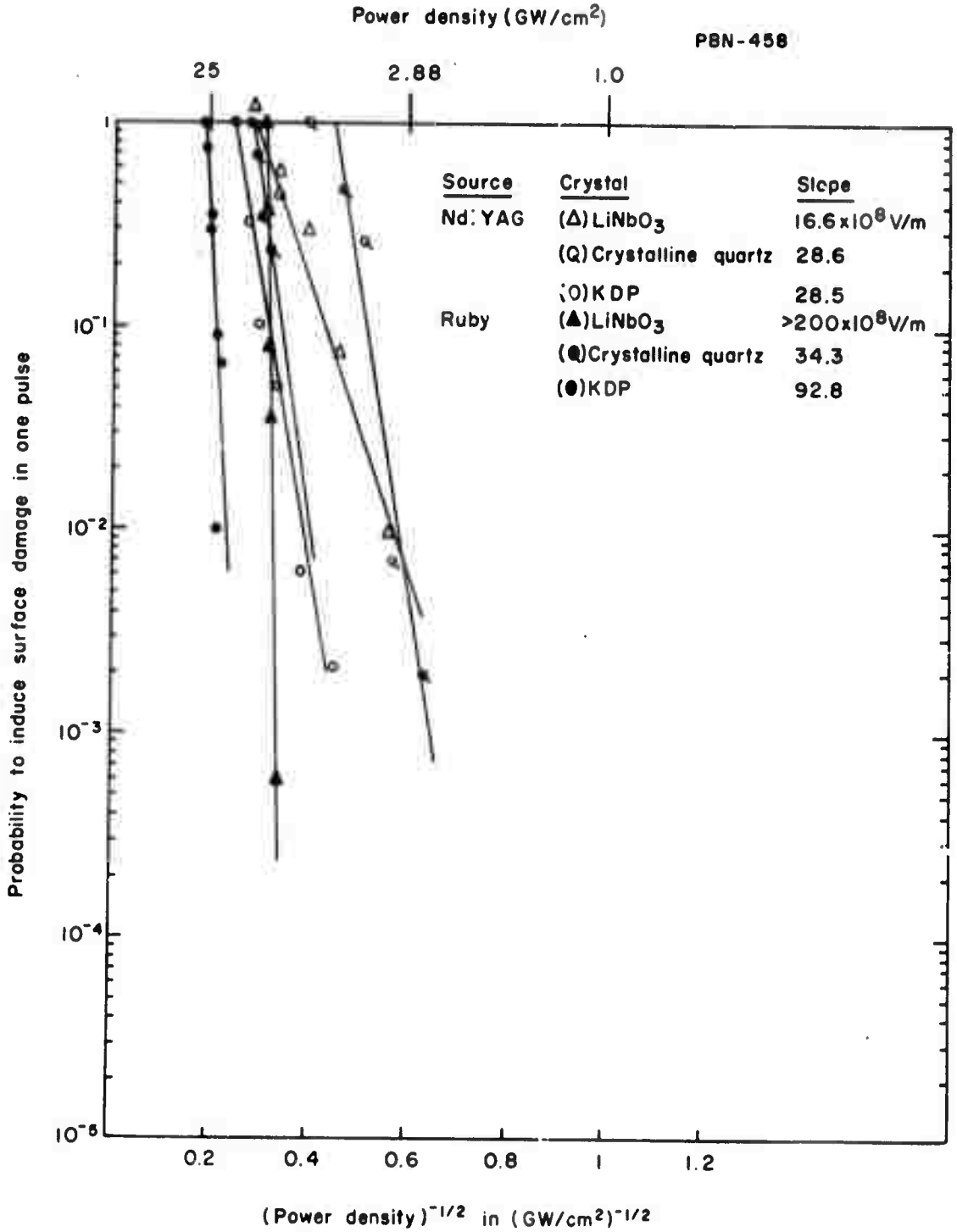

Fig. 29 Comparison of Damage Probability Measurements Obtained Using Nd:YAG or Ruby Laser Irradiation. (See also Fig. 25.)

quite different from that using a Nd:YAG laser. When using a ruby laser to irradiate $LiNbO_3$ the material is less likely to damage than when using a Nd:YAG laser of the same power density. However, the "slope" of the relationship between damage probability and power density plotted for $LiNbO_3$ is much steeper in the former case. In fact, with so steep a slope this material with ruby laser irradiation may be said to exhibit a "damage threshold." This case requires further study and analysis because, first, ruby laser light can produce annealable optical inhomogeneities in $LiNbO_3$ in the manner described in Sec. I and, second, $LiNbO_3$ absorbs strongly at $0.347\mu m$, the ruby laser second harmonic and so two-photon absorption may be important. In Secs. III-B and C the dependence of damage probability on the laser frequency is considered. Both the rate of change of probability with optical field strength and the magnitude of the probability for damage at any field are dependent on the laser frequency. Cases such as those of crystalline quartz and KDP will be studied in more detail in the future to determine how to account for the data in Fig. 29.

Since the ruby laser damage data was obtained during the last month of this program, there has not been enough time for more complete experimental and theoretical studies of the frequency dependence of damage probability. This will be a major area for future work.

I. Measurements of the Distribution of Breakdown Starting Times

The experimental apparatus described in Fig. 17 with the Nd:YAG laser in Fig. 1 was used to study the distribution of surface breakdown initiation times as a function of damage probability. Since these experiments were initiated during the summer of 1971 only two materials, plate glass and $SrTiO_3$, had been studied at the time this report was written. So far, however, we have found that the most likely time for a breakdown to begin is before the peak of the laser pulse and that the width of the distribution increases with decreasing optical electric field strength. These results are discussed analytically in terms of the probabilistic model of damage in Sec. III-B.

Figure 30 shows the distributions of breakdown starting times obtained for plate glass at three different levels of irradiation. Twenty to twenty-five measurements were made to obtain each distribution. At the highest level, where the peak optical field strength was 41.8×10^7 V/m the power density was P_1, the lowest value at which damage always occurred in one pulse. Notice the spread in the distribution as the field strength is lowered and the fact that the most probable starting time is before the field strength is maximum in all three cases. Figure 31 shows similar results for $SrTiO_3$.

The spread in the starting times as the field strength is lowered is further evidence of the probabilistic nature of laser induced damage. A phenomenon governed by a threshold field strength would always break down when that field strength was reached and the distribution of starting times would always be very sharp.

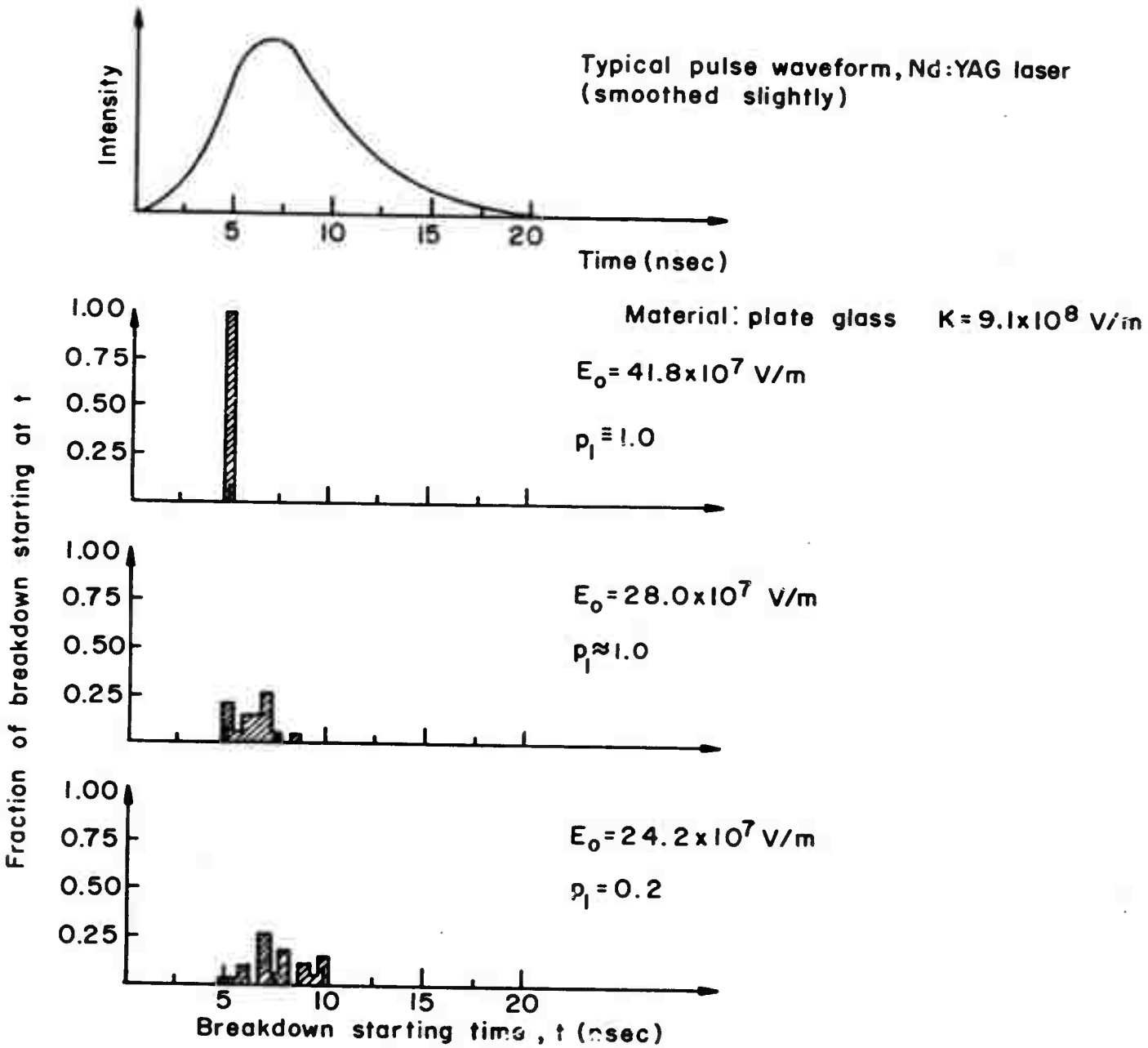

Fig. 30 Distribution of Surface Breakdown Starting Times for Plate Glass for Three Different Damage Probabilities.

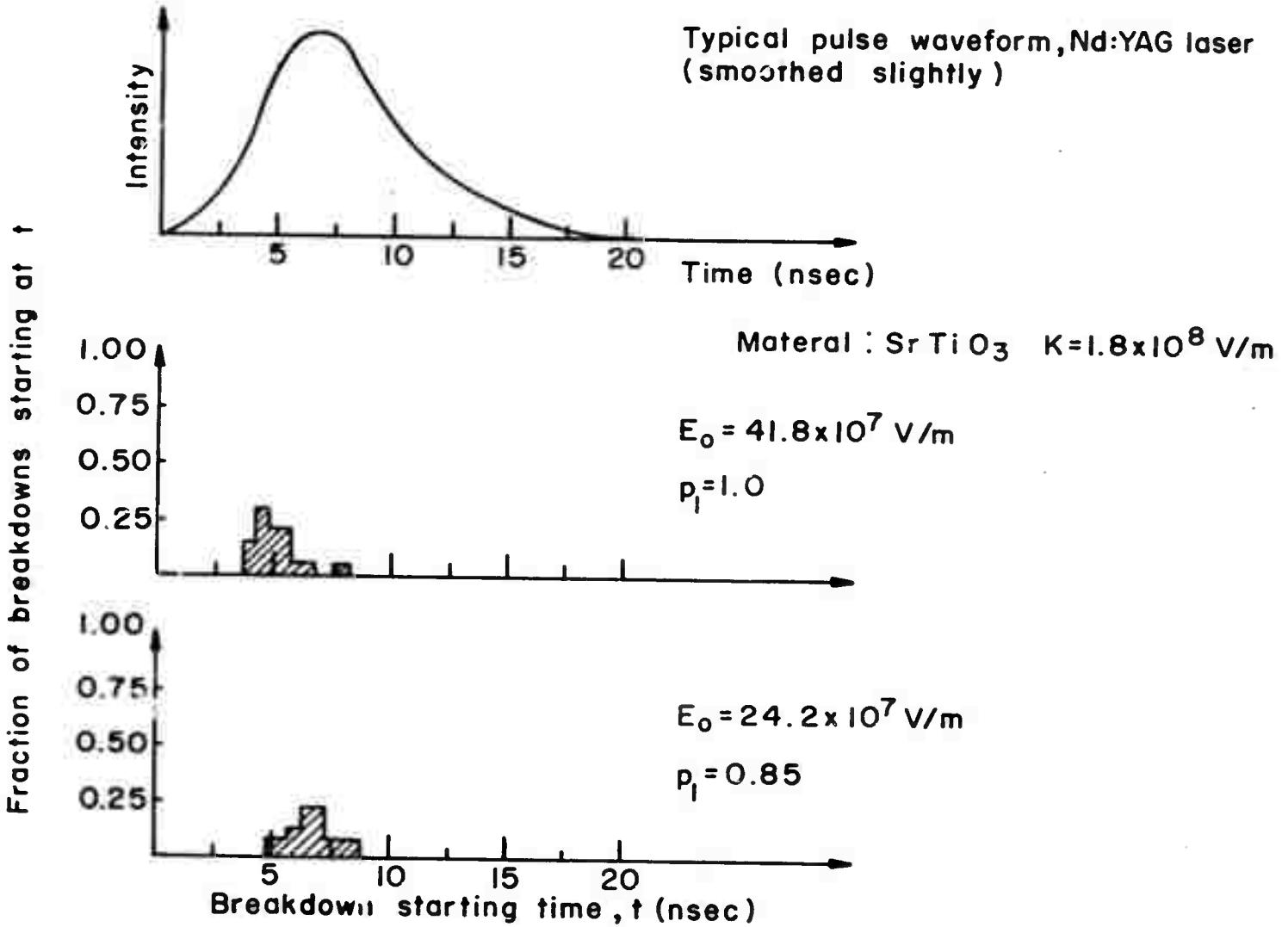

Fig. 31 Distribution of Surface Breakdown Starting Times for $SrTiO_3$ for Two Different Damage Probabilities.

III. THEORETICAL EXAMINATION OF DAMAGE PROBABILITY

A. Avalanche Breakdown

Avalanche breakdown has been considered previously by several other workers, including Wasserman,[12] Sviridenkov,[13] Zverev et al.[14] and Hellwarth.[15] However, since the results of their work showed that the calculated breakdown field was an order of magnitude larger than that which was measured, this mechanism is not generally accepted as responsible for laser induced damage. The data presented in Figs. 25 and 29 and the discussion of avalanche breakdown presented in the rest of this section show that avalanche breakdown should be considered as a possible damage mechanism.

Our review of previous work on the possibility of avalanche breakdown in optical field begins with a discussion of the role of electron collisions. A perfectly free electron in an optical frequency electric field will simply oscillate back and forth with its velocity 90° out of phase with the driving field and consequently there will be no average energy absorption. The coherently oscillating energy of such an electron in a field at the damage threshold is readily calculated to be only 10^{-3} to 10^{-4} eV. Therefore there is no possibility of an ionizing collision.

However, electrons in a solid are not really free. They experience collisions with phonons which tend to relax the distribution towards equilibrium. These collisions also result in a component of electron velocity in phase with the field so that there can be an average energy absorption. A phenomenological equation of motion for an electron in a solid may be written as

$$m^* \left(\frac{\partial v}{\partial t} + \frac{v}{\tau} \right) = eE\, e^{i\omega t} \quad , \tag{3}$$

where m^* is the effective mass, v is the electron velocity, τ is some average relaxation time, e is the electronic charge and E is the amplitude of the electric field at radian frequency ω. It is easy to see that the energy $\mathcal{E}$, of an electron raised to the conduction band increases initially as

$$\partial \mathcal{E}/\partial t = \frac{1}{2} \operatorname{Re} \langle eE \cdot v^* \rangle = \frac{\tau e^2 E^2/2m^*}{1+\omega^2\tau^2} \approx \frac{e^2E^2}{2m^*\omega^2\tau}, \qquad (4)$$

Equation (4) predicts that $\mathcal{E}$ will grow without limit, which, of course, is unrealistic. The energetic, or "hot", electrons will also lose energy, primarily by collisions with optical phonons. An equilibrium may be thus established as discussed by Wasserman.[12] However, at high fields, all electrons having energy greater than some value $\mathcal{E}_c$ will, on the average, gain more energy than they lose and therefore will be accelerated to ionizing energies.

Detailed treatments based on this approach must include a calculation of the electron-optical phonon interaction and a discussion of the choice of $\mathcal{E}_c$. The problem has much in common with the dc breakdown of dielectrics, where fairly accurate calculations of the threshold are possible.[16] For the optical case, this procedure was carried out by Wasserman.[12] He calculated a breakdown field an order of magnitude greater than is observed.

On the other hand, a rather different approach has been successful for the closely related problem of avalanche multiplication breakdown in semiconductor p-n junctions. There Chynoweth[17] found empirically that the ionization coefficient α (E), analogous to the first Townsend coefficient[18] in gas breakdown, varied with field as

$$\alpha(E) \sim \exp(-\text{const}/E) \qquad (5)$$

Physically, α (E) is the average number of hole-electron pairs produced by an electron falling 1 cm in the field direction.

For high frequency cw fields, breakdown occurs when the rate of increase of the number of electrons, simply related to α (E), exceeds the rate of loss of electrons due to recombination, trapping or diffusion out of the field region.[18] For pulsed fields, there is the additional requirement that the electron concentration buildup to destructuve levels during the pulse period. In either case, the major problem is the calculation of α (E) which, to our knowledge, has not been carried out for optical fields.

For dc fields several calculations of α (E) are available. The simplest is due to Shockley.[19] He contends that an equation of motion like Eq. (3) is not applicable because it gives the behavior of an average electron. Ionization is produced mainly by those exceptional electrons which are accelerated to the ionizing energy $\mathcal{E}_i$ without undergoing a single collision, even though they must cover a distance of many mean free paths. The probability of a particular electron covering a distance x without a collision is exp $(-x/\ell)$, where ℓ is the mean free path. To be accelerated to $\mathcal{E}_i$, the electron must traverse a distance $x = \mathcal{E}_i/eE$. Therefore

$$\alpha (E) \sim \exp (-\mathcal{E}_i/eE\ell) \quad . \tag{5a}$$

Shockley found that Eq. (5) gave a good fit to Chynoweth's data with $\ell \sim 100\text{Å}$.

A very different approach was taken by Wolff[20] who used a Boltzmann equation and expanded the electron distribution function in Legendre polynomials retaining only the zeroth and first-order terms. He found

$$\alpha \sim \exp (-\text{const}/E^2) \quad . \tag{6}$$

The basic difference between the approaches of Wolff and Shockley is that the former assumes that the distribution is only slightly distorted, while the latter assumes that it develops a large spike in the field direction.

The discrepancy was resolved by Baraff[21] and Keldysh[22] who showed that Eq. (5) is the low-field limiting form of the general solution, while Eq. (6) applies only at high fields. The crossover point isn't well specified, but Shockley's result seems to work well to $E \sim 10^6$ V/cm. In other words, the electron may make several collisions before ionization without α (E) showing a significant departure from the exp (-const/E) behavior which was derived on the assumption of no collisions. Some justification for this success of Shockley's theory has been given by Baraff.[21]

Shockley's argument can also be applied to high frequency fields.* For an electron to continually gain energy from an alternating field, it must undergo certain favorable elastic collisions which reverse its momentum when the field reverses. Then a lucky electron in an optical frequency field is one which undergoes just the right collisions to keep it in phase with the field. Such an electron requires only about 5 cycles of the field (at $E = E_1$; see Table VIII) to reach ϵ_i. Admittedly, the sequence of special collisions has a low probability of occurrence, but so does the collisionless sequence postulated by Shockley. In fact, if the probability of some collision during one half-cycle of the field is almost unity, then no collision (or one with only a small momentum transfer) is as specific an event as the particular collision needed to keep the electron in phase with the field. We would therefore expect the dc and optical ionization probabilities to show the same field dependence.

To make this argument more precise, suppose that an electron, starting from rest, will remain "acceptably" in phase with the field provided it travels a distance $x_1 - \Delta x_1$ during one half-cycle, undergoes a "proper" collision somewhere between $x_1 - \Delta x_1$ and $x_1 + \Delta x_1$, then

---

* Note that by using the Shockley model for breakdown we are considering the energy distribution of electrons to be distorted with a large spike at high energies and in the direction of the field. This is the same conclusion reached by Giuliano et al. using several physically reasonable approximations to analyze the kinetic equation for electrons interacting with phonons in an intense optical field.[23]

TABLE VII

Damage Properties for Evaluating the Avalanche Breakdown Model

Material	K(V/M)	P_1(GW/cm^2)	E_1(V/M)$^+$	ℓ(Å)*	M	n(cm^{-3})$^\pm$
Plastic	133×10^8	16.1	5.3×10^8	4	2	6×10^{14}
Glass	66.5	14.4	5.0	8	2	1×10^{10}
Fused quartz	60.5	24.0	6.4	8	1	2×10^7
ADP	31.6	6.4	3.3	20	5	7×10^{11}
KDP	28.5	14.4	5.0	25	3	2×10^8
Crystal quartz	28.5	6.4	3.3	25	5	3×10^{12}
$LiNbO_3$	16.6	11.1	4.4	20	2	2×10^6
$Ba_2NaNb_5O_{15}$	16.7	6.4	3.3	20	4	6×10^8
$LiIO_3$	7.1	3.2	2.4	40	7	2×10^{11}
$SrTiO_3$	1.8	6.4	3.3	220	4	8×10^9

$^+$ E_1 is the RMS field at the exact center of the focal spot, assuming a Gaussian beam and assuming that the measured diameter of the focal spot corresponds to the 1/10 power points.

* Calculated from $K = \epsilon_i / e\ell$ using estimates of the bandgap for ϵ_i

$^\pm$ The initial free electron concentration calculated from Eq. (7) setting $p(E_1) = 1$ and assuming $f = 0.1$. Note that n = N ÷ focal volume.

travels to $x_2 - \Delta x_2$ without collision, etc. Obviously the turning points, x_m, must be given by the positions of the electron at the times when the field reverses. Suppose further that of all the electrons which undergo some collision between $x_m - \Delta x_m$ and $x_m + \Delta x_m$, a fraction f_m undergo a collision which reverses their momentum to a sufficient degree. For isotropic scattering, f_m might be expected to be about 0.1 or 0.2. The overall probability per unit time of the electron being accelerated to ϵ_i is the trial rate,[17] or frequency of collisions, τ_{coll}^{-1}, times the probability of this sequence of events:

$$P(\epsilon_i) = \tau_{coll}^{-1} \sum_{m=1}^{M} [\exp(-|x_m - x_{m-1}|/\ell)] [1-\exp(2\Delta x_m/\ell)] f_m. \quad (7)$$

M is the approximate number of half cycles of the field required for the electron energy to reach ϵ_i. Now if ℓ is sufficiently small, $\exp(-2\Delta x_m/\ell) << 1$, so that any electron which makes it into the range $x_m \pm \Delta x_m$ undergoes some collision with high probability, then

$$P(\epsilon_i) \approx \tau_{coll}^{-1} \sum_{m=1}^{M} [\exp-(|x_m - x_{m-1}|/\ell)] f_m \approx \tau_{coll}^{-1} f^M \exp(-x_i/\ell) \quad (8)$$

where x_i is the total path length needed to attain energy ϵ_i, i.e.,

$$x_i = \sum_{m=1}^{M} |x_m - x_{m-1}| = \epsilon_i / e\bar{E} \quad (9)$$

with $\bar{E}$ being the time average of the absolute magnitude of the optical electric field. We have assumed that all $f_m = f$. This treatment is clearly oversimplified because other sequences of collisions which include some unfavorable events may also lead to ionization. In fact, its inadequacies are the same as in Shockley's dc model, which nonetheless has been successful in describing the experimental data.

It still remains to connect $P(\epsilon_i)$, the probability of a single electron reaching ϵ_i, with $p_1(E)$, the probability of damage in a single pulse. In general, this is a difficult problem, requiring the calculation of the distribution of avalanche sizes and integrating to determine what fraction of the avalanches exceed the critical size for damage. However, the experimental data suggests that $p_1(E) \propto P(\epsilon_i)$, which could happen if the avalanche statistics were governed by the first stage or two of the avalanche. This assumption is plausible since the mean energy of the secondary carriers produced by an ionizing collision is much greater than kT and may even be greater than the bandgap.[24] The secondary then has a much higher chance of itself producing ionization than a thermal carrier, and so, following the first one or two steps in the avalanche, the process can continue until breakdown occurs.[25] Thus, assuming further that the mean number, N, of initial free electrons in the focal volume is independent of E prior to onset of the avalanche, we obtain

$$p_1(E) = f^M N (\tau_{laser}/\tau_{coll}) e^{-\epsilon_i/e\bar{E}\ell} \quad . \tag{10}$$

Now, M is given by

$$M = \frac{\sqrt{2m\epsilon_i}}{e\bar{E}} \left(2\nu_{opt}\right) \tag{11}$$

where ν_{opt} is the optical frequency. Then the f^M factor may be written

$$f^M = \exp\left[\left(-\frac{\sqrt{2m\epsilon_i}}{e} 2\nu_{opt}\ \ell n(\tfrac{1}{f})\right)/\bar{E}\right], \tag{12}$$

so that this factor simply changes the coefficient of $\bar{E}^{-1}$ in the exponent. Therefore, finally,

$$p_1(E) = A\, e^{-K/\bar{E}} \tag{13}$$

where

$$A = N\, \tau_{laser}/\tau_{coll} \tag{14}$$

and

$$K = \frac{\epsilon_i}{e\ell} + \frac{\sqrt{2m\epsilon_i}}{e} \, 2\nu_{opt} \, \ell n \frac{1}{f} \quad . \tag{15}$$

The second term in K was omitted in previous reports, but can be significant in materials, such as $SrTiO_3$, which have small measured values of K.

The data in Figs. 25 and 29 and Table VII agree qualitatively with Eq. (13) in several respects. Obviously the functional dependence on field is correct. Also, the amorphous materials are all quite damage-resistant and show large slopes. In terms of Eq. (10), this is probably due to the small value of ℓ, which should be comparable to the mean interatomic distance, as observed[26] (see Table I). Among the crystalline materials, those with a large gap (KDP, ADP and quartz) and therefore large ϵ_i have a large slope. $SrTiO_3$ is known to have a relatively large mobility[27] which implies a large ℓ (to the extent that "hot" electrons are scattered by the same mechanism as thermal ones) and therefore a small slope. The values of ℓ in Table VII derived neglecting the second term in Eq. (15), for all of the crystalline materials are in the range 20 - 220Å. For comparison $\ell \sim$ 50 - 100Å is found in Si and Ge from avalanche multiplication data.[16,17]

A further check on Eq. (10) is obtained by computing N using $p_1(E_1) = 1$ and assuming f = 0.1. The resulting carrier concentrations, n, shown in the last column of Table VII are all reasonable. Only the values for $LiNbO_3$ and plastic look at all unusual for dielectrics, and in the latter case especially, n is very sensitive to the precise value of E_1; a 10 percent change in E_1, comparable to experimental error, leads to a factor of 10 change in n.

In spite of this good qualitative agreement, the model which led to Eq. (10) is highly simplified and further theoretical work is needed. The

factors f_m should be calculated taking account of band structure and phonon spectra. The variation of electron mean free path and effective mass with energy should be considered. Finally, a proper calculation of $P(\epsilon_i)$, possibly by a Monte Carlo technique, should be performed. This would obviate the need for the assumption of small ℓ which was made in our derivation, and which in fact is not satisfied for some of the materials studied here.

B. Temporal Effects

The discussion in the last section considered the optical field to be constant over the pulse width τ_{laser}. This assumption must be removed, and a more rigorous derivation of the damage probability given, in order to explain the streak camera data in Sec. II-I.

From the discussion in the last section, the probability per unit time of any one electron being accelerated to ϵ_i is given by $B\exp(-K/\overline{E})$ where

$$B = \tau_{coll}^{-1} \tag{16}$$

Therefore the probability per unit time of some electron reaching ϵ_i is

$$h(t) = n \int B\, e^{-(K/\overline{E})}\, dv \tag{17}$$

where n is the density of free carriers, here assumed independent of $\overline{E}$, and the integral is over the volume occupied by the field. The prefactor B can, in general, depend on $\overline{E}$ since the electron energy distribution changes with field. However, for simplicity, this effect is neglected.

To perform the integral in Eq. (17) we must assume some form for the spatial distribution of E. First, we take the radial dependence of the field to be gaussian:

$$\overline{E} = \overline{E}(\rho,t) = \overline{E}_0 f(t)\, e^{-\beta\rho^2} . \tag{18}$$

Here f(t) is a normalized pulse shape function and β is a parameter related to the beam diameter. The bar over $\bar{E}$ and $\bar{E}_0$ signifies an average of the field magnitudes taken over one cycle of the optical frequency during which f(t) is so slowly varying as to be considered constant.

The second assumption relates to the variation of E in the depth or z dimension. Here we assume that there exists some characteristic dimension z_c, such as the focal depth, the distance below the surface in which damage can be detected, or a distance over which n is substantially greater than in the bulk due to surface states. Then we assume $\bar{E}$ to be constant for $0 \leq z \leq z_c$ and to be zero otherwise.

Finally, the probability per unit time of a lucky electron reaching ϵ_i is

$$h(t) \approx nB \int \exp\left[-K/(\bar{E}_0 f(t)\, e^{-\beta\rho^2}) \right] 2\pi\rho d\rho dz$$

$$\approx \pi z_c nB \int \exp\left[-K(1+\beta\rho^2)/\bar{E}_0 f(t) \right] d(\rho^2) \,. \tag{19}$$

The second step is valid here if $K/\bar{E}_0 >> 1$ so that $\beta\rho^2$ is a small quantity anywhere that the exponential factor is appreciable.

Performing the indicated integrations, we obtain

$$h(t) = \pi z_c nB \left(\frac{\bar{E}_0 f(t)}{\beta K}\right) \exp\left(-K/\bar{E}_0 f(t)\right) \tag{20}$$

The interpretation of this result is aided by defining a time-dependent effective field volume by

$$V_{eff} = \pi \frac{z_c}{\beta} \frac{\bar{E}_0 f(t)}{K} \tag{21}$$

In other words, Eq. (13) is still valid for the time dependent case, but with N replaced by nV_{eff}. This comes about because at small fields, or in materials with large K, the exponential factor varies so rapidly with E that only that portion of the volume near the very peak of the field spatial distribution participates in breakdown.

Now, h(t) is still not the quantity to be compared to the streak camera data, since we have not allowed the possibility that destructive damage occurs at some time before t. Let us suppose, as discussed in the previous section, that damage occurs with high probability after some electron has been accelerated to ϵ_i. Further assume that this damage occurs with a very small time delay, say less than 1 nsec. This latter assumption is plausible from the work of Seitz, who showed that only some 40 generations of an avalanche are needed to disrupt a lattice. In our case the first generation takes only M cycles of the field, and subsequent ones may take even less if, as discussed previously, the resulting carriers from an ionization event have much more than thermal energy. Therefore, the time delay between the occurrence of the lucky electron and visible damage is expected to be only a few hundred cycles at most.

Consider an ensemble of samples, each subjected to the same laser pulse. Let g(t) dt be the fractional number of samples in the ensemble which damage between t and t+dt and $\nu(t)$ be the fractional number which have not damaged by time t. The time origin, t = 0, is taken to be before the application of the laser pulse so that, $\nu(0) \equiv 1$. g(t) must satisfy

$$g(t) = -\frac{\partial \nu(t)}{\partial t} = \nu(t)\, h(t) \tag{22}$$

since, by our assumptions, h(t) is now the damage rate. Therefore

$$\nu(t) = \exp\left[-\int_0^t h(t')\, dt'\right] \tag{23}$$

and

$$g(t) = h(t) \exp\left[-\int_0^t h(t')\, dt'\right] \tag{24}$$

The most probable time for breakdown to begin is the time, t_M, when g(t) is maximum. Thus we consider

$$\frac{d(g(t))}{dt} = \left(\frac{d(h(t_M))}{dt} - (h(t_M)^2 \right) \exp\left(-\int_0^{t_M} h(t')\, dt' \right) = 0 \quad . \tag{25}$$

Since $\exp\left(-\int_0^{t_M} h(t')\, dt'\right) \neq 0$, Eq. (25) holds when

$$\frac{d(h(t_M))}{dt} = (h(t_M))^2 \quad . \tag{26}$$

Between t = 0 and t_{E_M}, the time where the field strength is largest $dh(t)/dt \geq 0$ and Eq. (26) can be solved. For times greater than t_{E_M}, $d(h(t))/dt < 0$ and there is no solution to Eq. (26). We conclude therefore that $t_M \leq t_{E_M}$ which is in agreement with the experimental results in Figs. 30 and 31. Note that this result is independent of the precise form of h(t). The only requirement on h(t) is the physically reasonable condition that

$$\frac{dh}{dE} > 0 \text{ for all } t \ .$$

The formalism developed in this section will be used for detailed computer computations of the temporal distributions in the rest of the program.

C. Dependence of Damage on Optical Frequency

If the laser wavelength is changed, the formalism given in the previous sections would predict only a change in K (see Eq. (15)). However, the prefactor A may also have a wavelength dependence if the initial carrier density n is due to multiphoton absorption of the laser light rather than thermal excitation. Then A will also depend on E,

i.e., if j photons are required to excite carriers from the valence band or an impurity level, A will be proportional to E^{2j}.

This possibility will be explored further when more data on damage probabilities are available using ruby laser. An attempt will be made to find a physically reasonable value of j for the various materials which will be consistent with the probability vs field data, its wavelength dependence (see Figs. 25 and 29) and the temporal distributions (see Figs. 30 and 31).

IV. THEORETICAL ANALYSIS OF SELF-FOCUSING

The destructive effects of a high-power laser beam upon an optical crystal will depend upon the electric field intensity within the solid. However, because of the self-focusing of the light beam, the electric field within the solid will vary from point to point in a manner which must be determined from the intensity and the phase distribution of the incident radiation. To provide a tool for calculating this intensity, we have developed a computer program which numerically calculates the beam dimensions and the electric field intensity within the solid, given certain input information which includes the entrance face conditions for the beam, the pulse shape as a function of time, and a formula relating the index-of-refraction variations to the variations in electric field intensity.

We have taken advantage of certain approximations which are normally valid for the laser beams of interest, in order to simplify the mathematics and also to reduce the amount of data which is required to specify the solution to our computation. For example, we make the paraxial approximation, that is, we assume that the distance along the beam in which significant changes take place in the time-averaged intensity is large compared with the radius of the beam. Also we assume axial symmetry and show that these approximations are sufficient to lead to a self-similar solution near the axis. By self-similar, we mean a solution in which the power flux has the form

$$I = I_o(z)\, h^2(\xi) \quad , \tag{27}$$

where $\xi = r/a(z)$, and I_o and a are independent of r (we have suppressed a time dependence which occurs over a scale comparable to the pulse duration, on the order of nanoseconds in the experimental setup).

Our mathematical methods are closely related to those described previously in Refs. 28-32, although these references generally refer to Gaussian distributions of intensity, instead of the more general self-similar solutions. Self-similar solutions have been used effectively in the past for simplifying the partial differential equations of Hydrodynamics; these self-similar solutions

might be appropriately referred to as "automodel flows", as in the Russian hydrodynamic literature, since the intensity distribution across the beam at one position is modeled after its own shape at a different position.[33-35]

There will generally be some response time for the nonlinear response of the dielectric constant to the applied field. For example, if the induced change of dielectric constant were due to thermal effects, there would be a time lag before the temperature would build up to its final value, and similarly, after the main pulse was turned off, a temporary trail of an induced inhomogeneity in the index of refraction would remain and might provide lensing effects during times comparable to the response time. At the present time, we have incorporated "memory" effects into the computer program by assuming that the index of refraction at a point depends upon the entire history of the electric intensity at that point. Later it would be useful to include the effects of elastic waves induced by electrostrictive forces, which differ from the present model because the acoustic disturbance at a point depends on the history of the electromotive forces at all points within some neighborhood of the point of interest.

A. Dependence of the Index of Refraction Upon the Electric Field

In most of the literature on self-focusing, the index of refraction has been written in the form

$$\eta = \eta_o + \eta_2 u - \eta_4 u^2 \quad , \tag{28}$$

where $u = 1/2\ \eta_o |E^2|$ with E the peak electric field ($\vec{E} = i E e^{i\omega t}$). Equation (28) is valid when η changes slowly during a period comparable with a period of the optical field but changes rapidly compared with the laser pulse duration.

Equation (28) should be looked at as the first terms of a Taylor's expansion in powers of the square of the electric field. For very strong fields, the expansion will not be valid and it is known that, with a sufficient increase in

the field, the index of refraction will approach a limiting value known as the saturation limit. In fact, the term in Eq. (28) involving η_4 was included by Akhmanov et al.[28] as a first approximation to the polarization saturation. In general, the index of refraction is some arbitrary function of E^2, $\eta = f(E^2)$, and our computer program was written in such a way that any desirable formula can be included with little difficulty. For example, Wagner et al.[30] use a relationship of the form

$$\eta = \sqrt{\eta_o^2 + \frac{\eta_2 E^2}{1 + E^2/E_s^2}} \quad , \tag{29}$$

where Eq. (29) is slightly different in form from Ref. 16 because the nonlinear effects in that reference were expressed in terms of dielectric susceptibilities instead of the indices of refraction.

The effect of relaxation processes have been included in our computer program by generalizing the definition of u in Eq. (28) to

$$u = \frac{1}{2} \frac{\eta_o}{\tau_o} \int_{-\infty}^{t} |E^2(\tau)| \, e^{-\frac{(t-\tau)}{\tau_o}} \, d\tau \quad , \tag{30}$$

where τ_o is a relaxation time. The change in E in Eq. (30) will occur over periods comparable to the pulse duration which in our experiment will be on the order of nanoseconds. If the relaxation time is very short compared to the pulse duration, Eq. (30) reduces to the instantaneous form

$$u = \frac{1}{2} \eta_o |E^2(t)| \quad , \tag{31}$$

which was given previously. On the other hand, when the relaxation time is long, then Eq. (30) approaches the form

$$u = \frac{1}{2} \frac{\eta_o}{\tau_o} \int_{0}^{t} |E^2(\tau)| \, d\tau \quad , \tag{32}$$

where the pulse has been taken to vanish for $t < 0$.

More realistically, when the relationship between the index of refraction and the field is a linear functional of E^2, we would have

$$u(r,t) = \frac{1}{2}\,\eta_o \int_{-\infty}^{t} d\tau \int dr'\, G(r'',t'')\,\left|E^2(\vec{\tau},\vec{r'})\right| \quad , \tag{33}$$

where $t'' = t - \tau$ and $\vec{r''} = \vec{r} - \vec{r'}$. Equation (33) is the sort of relationship we might expect if heat or momentum were released at a position $\vec{r'}$ at time τ and G plays a role similar to a Green's function in describing the propagation of the effect to the position $\vec{r}$ at time t. We now make the somewhat drastic approximation that

$$G(r'',t'') = \delta(\vec{r''})\, g\,(t'') \quad ,$$

which ignores the transfer of fluctuations in the index of refraction from point to point in the medium as would be expected to occur due to thermal conduction and convection when the fluctuations are caused by thermal effects or due to elastic waves when the fluctuations are caused by electrostriction. Then Eq. (33) becomes

$$u(\vec{r},t) = \frac{1}{2}\,\eta_o \int_{-\alpha}^{t} \left|E^2(\tau,\vec{r})\right|\, g(t'')\, d\tau \quad . \tag{34}$$

Equation (30) results from Eq. (34) when we take $g(t'') = \exp(-t''/\tau_o)/\tau_o$ which, with an appropriate choice of the relaxation time τ_o, should be an appropriate approximation since it is physically apparent that g(t'') must be a monotonically decreasing function of t''.

B. Electrostrictive Effects

The characteristic time scale for elastic waves excited by a laser beam is on the order of the beam radius divided by the longitudinal sound velocity.

Although the precise value depends upon the beam radius, this suggests a characteristic time on the order of 10^{-8} seconds. Since this is comparable to the pulse duration, and also because the exit-face surface damage might involve elastic waves striking a semimolten surface, one might wish to include these effects in the final version of the computer program as a separate term independent of the relaxation form described in the previous section, using an approach similar to that of Kerr.[32]

The electrostrictive force is a volume force proportional to the gradient of the intensity, i.e.,

$$f = \alpha \nabla I \quad ,$$

where $I = \frac{1}{2} E^2$. If we let $\vec{u}$ be the displacement, the equation of motion is

$$\rho \ddot{\vec{u}} = \vec{F} + \vec{f} \quad , \tag{35}$$

where

$$F_i = \frac{\partial \sigma_{ik}}{\partial X_k} \quad .$$

For a solid satisfying Hooke's law, the stress is a linear function of the strain and when the body is also isotropic, we have[36]

$$\ddot{\vec{u}} = c_\ell^2 \text{ grad div } u - c_t^2 \text{ curl curl } \vec{u} + \frac{\alpha}{\rho} \text{ grad } I \quad , \tag{36}$$

where $c_\ell^2 = E(1-\sigma)/\rho(1+\sigma)$, $c_t^2 = E/2\rho(1+\sigma)$, E is Young's modulus, and σ is Poisson's ratio.

Since an arbitrary vector can be written in the form

$$\vec{u} = - \text{grad } \phi + \text{curl } \vec{A} \quad , \tag{37}$$

Eq. (36) becomes

$$\text{grad}\left[\ddot{\phi} - c_\ell^2 \nabla^2 \phi + \frac{\alpha}{\rho} I\right] = \text{curl}\left[\ddot{\vec{A}} + c_t^2 \text{ curl curl } \vec{A}\right] . \quad (38)$$

In an infinite medium, it is apparent from Eq. (38) that only the longitudinal wave will be excited by electrostrictive forces and that it will satisfy

$$\ddot{\phi} = c_\ell^2 \nabla^2 \phi - \frac{\alpha}{\rho} I \quad . \quad (39)$$

At first, we will neglect the vector wave $\vec{A}$ although we note that transverse waves described by the vector $\vec{A}$ will be excited by boundary conditions at the surface. This effect may be important for calculations of the acoustic intensity at the exit face.

Now let $\rho' = \rho - \rho_o$ be the increase in density. From the continuity equation for small amplitude waves, we find

$$\rho' = \rho_o \nabla^2 \phi \quad ,$$

so the wave equation for ρ' becomes

$$\frac{\partial^2 \rho'}{\partial t^2} = c_\ell^2 \nabla^2 \rho' - \alpha \nabla^2 I \quad . \quad (40)$$

Equation (40) is the wave equation with a source term depending upon the optical intensity I. The transverse Laplacian terms in a paraxial laser beam will be much larger than the longitudinal terms. Then, Eq. (40) can be solved as a two-dimensional problem at each point z, and for axial symmetry has the form

$$\frac{\partial^2 \rho'}{\partial t^2} = c_\ell^2 \frac{1}{r} \frac{\partial}{\partial r} r \frac{\partial \rho'}{\partial r} - \frac{\alpha}{r} \frac{\partial}{\partial r} r \frac{\partial I}{\partial r} \quad . \quad (41)$$

Equation (41) can be solved numerically by making use of the usual Green's functions[37] by methods similar to those of Kerr[32] and must be solved simultaneously with the equation for the intensity I. When the laser pulse is turned on, Eq. (41) describes a sound wave which initially implodes upon the axis, giving a high density on the axis, thus forming a self-focusing acoustic lens. As time goes on the density on the axis will temporarily decrease as the acoustic wave is reflected from the axis, in a manner dependent upon the laser pulse shape, but it will essentially reach the steady state condition in which the left-hand side of Eq. (41) vanishes. Then ρ' takes the steady-state form

$$\rho' = \frac{\alpha}{c_\ell^2} I \quad , \tag{42}$$

with an index of refraction

$$\eta = \eta_o + \left(\frac{\partial \eta}{\partial \rho_s}\right) \rho' \quad . \tag{43}$$

Thus for times large compared with the relaxation time, the steady-state form of Eq. (43) is the same form as Eq. (28) (with $\eta_4 = 0$).

C The Paraxial Beam-Tracing Equation

We consider a laser beam propagating in the z-direction and symmetrical about the z-axis. We assume that the electric field magnitude can be written in the similarity form

$$E(r,z) = E_o h(\xi) a(o)/a(z) \quad , \tag{44}$$

where $\xi = r/a$, E_o is independent of r and z and a is a function of z alone. The radial distribution, $h(\xi)$, is determined by the boundary conditions at the entrance plane, and may, for example, have the Gaussian form

$$h(\xi) = e^{-(\xi^2/2)} \quad . \tag{45}$$

Here a may be considered as the beam radius. We have suppressed a slow time dependence in E_o and a, which change over a time comparable with the pulse duration.

Although we have assumed the self-similar form given in Eq. (43), we will show that, near the axis of the beam, this form is consistent with the governing equations. These governing equations can equally well be obtained from the ray-tracing equation of geometrical optics[29] or from the eikonal approximation to the wave equation.[28,30] In the former approach, the diffraction term must be added in an ad hoc manner to give agreement with the linear wave equation.

Taking the wave equation approach, with vanishing conductivity, the wave equation is

$$\text{curl curl } \vec{E} = -\frac{1}{c^2} \frac{\partial^2 \vec{D}}{\partial t^2} \quad , \tag{46}$$

where we have assumed the magnetic permeability $\mu = 1$. The electric displacement $\vec{D} = \eta^2 \vec{E}$ where η is the index of refraction and is inhomogeneous since it depends upon E^2. In general we assume that η depends upon the average of E^2 over many optical cycles so that to sufficient accuracy

$$\frac{\partial^2 \vec{D}}{\partial t^2} \simeq \eta^2 \frac{\partial^2 \vec{E}}{\partial t^2} \quad ,$$

and Eq. (46) becomes

$$\nabla^2 \vec{E} - \text{grad div } \vec{E} = \frac{\eta^2}{c^2} \frac{\partial^2 \vec{E}}{\partial t^2} \quad . \tag{47}$$

Now

$$\text{div } \vec{D} = 0 = \eta^2 \text{ div } \vec{E} + 2\eta \vec{E} \cdot \nabla \eta \quad ,$$

so div $\vec{E} = -\vec{E} \cdot \nabla (\ln (\eta^2))$. Thus the div $\vec{E}$ term does not generally vanish; however, it is generally small except near the focal point[32] and we will neglect the term henceforth.[30] To proceed we assume that

$$\vec{E} = \hat{e}\, \frac{a(0)}{a(z)}\, E_o(t)\, h(\xi)\, e^{-iks(r,z)}\, e^{i(\omega t - kz)}$$

$$= \hat{e}\, \psi E_o(t)\, e^{i(\omega t - kz)} \quad , \tag{48}$$

where we specify $E_o(t)$, $h(\xi)$ and $s(r,0) = r^2/2R^2$ at the entrance face where the boundary condition on the eikonal $s(r,0)$ has been chosen so that the light will focus at the point $z = R$. The propagation constant $k = \eta_o \omega / c$.

Neglecting div $\vec{E}$, Eq. (47) becomes

$$\frac{1}{r}\frac{\partial}{\partial r}\, r\, \frac{\partial \psi}{\partial r} + \frac{\partial^2 \psi}{\partial z^2} - 2ik\frac{\partial \psi}{\partial z} + (\eta^2 - \eta_o^2)\frac{\omega^2}{c^2}\psi = 0 \quad . \tag{49}$$

For paraxial beams the term $\frac{\partial^2 \psi}{\partial z^2}$ can be assumed small in comparison with the transverse Laplacian. Then let $\psi = \psi_o\, e^{-iks}$, multiply Eq. (49) by e^{iks} and equating imaginary parts, we obtain

$$\frac{\partial \psi_o^2}{\partial z} = -\frac{1}{r}\, \frac{\partial}{\partial r}\, r\, \psi_o^2\, \frac{\partial s}{\partial r} \quad . \tag{50}$$

Integrating Eq. (50) over a volume bounded by $r = R_o$ and the planes $z = z_1$, and $z = z_2$, when $R_o \to \infty$, shows that the power

$$2\pi \int_0^R \psi_o^2\, r\, dr \quad ,$$

is a constant independent of z which is necessary in a nonabsorbing medium. This is consistent with the self-similar form since

$$\int \psi_o^2 \, r \, dr = \frac{a^2(0)}{a^2} \int_0^R h^2(\xi) \, r \, dr$$

$$= a^2(0) \int_0^{R/a} h^2(\xi) \, \xi \, d\xi = \text{constant.}$$

Equating the real parts of Eq. (49) yields

$$\frac{1}{k^2 \psi_o} \frac{1}{r} \frac{\partial}{\partial r} r \frac{\partial \psi_o}{\partial r} + \frac{\eta^2 - \eta_o^2}{\eta_o^2} = \left(\frac{\partial s}{\partial r}\right)^2 + 2 \frac{\partial s}{\partial z} \quad , \tag{51}$$

and, using the self-similar form for ψ_o, we have

$$\frac{1}{k^2 a^2} \frac{1}{h(\xi)} \frac{1}{\xi} \frac{\partial}{\partial \xi} \xi \frac{\partial h}{\partial \xi} + \frac{\eta^2 - \eta_o^2}{\eta_o^2} = \left(\frac{\partial s}{\partial r}\right)^2 + 2 \frac{\partial s}{\partial z} \quad . \tag{52}$$

In general, Eqs. (50) and (51) are in a convenient form for numerical solution independent of the similarity assumption, since these equations could be numerically integrated by a marching method starting from the boundary conditions at $z = 0$. For a similarity solution we expand s, and η in Taylor's series in ξ, which have the form

$$s(r,z) = s_o(z) + \frac{1}{2} s_2(z) \xi^2 \quad , \tag{53a}$$

$$\frac{\eta^2 - \eta_o^2}{\eta_o^2} = K_o(z) + \frac{1}{2} K_2(z) \xi^2 \quad , \tag{53b}$$

so that substituting Eq. (53a) into Eq. (50) yields

$$a \frac{da}{dz} = s_2 \quad , \tag{54}$$

while substituting Eq. (53b) into Eq. (52) yields

$$2 \frac{\partial s_o}{\partial z} + \xi^2 \left(\frac{\partial s_2}{\partial z} + \frac{2 s_2}{a} \frac{da}{dz} + \frac{s_2^2}{a^2} \right) - K_o(z) - \frac{K_2(z) \xi^2}{2}$$

$$= \frac{1}{k^2 a^2} \frac{1}{h \xi} \frac{\partial}{\partial \xi} \xi \frac{\partial h}{\partial \xi} \quad . \tag{55}$$

If h is the Gaussian $e^{-\xi^2/2}$, the right hand side of Eq. (55) is $(\xi^2 - 2)/k^2 a^2$. For other functions we can expand $d = 1/h\xi \; \partial/\partial\xi \; (\xi \; \partial h/\partial \xi)$ in a Taylor's series so that the right hand side equals $d(0) + d'' \xi^2/2$. In either case we obtain an equation for s_2 by equating the coefficients of ξ^2. For the Gaussian we obtain

$$- \frac{2 s_2}{a} \frac{da}{dz} + \frac{d}{dz} s_2 + \frac{s_2^2}{a^2(z)} = \frac{K_2(z)}{2} + \frac{1}{k^2 a^2} \quad , \tag{56}$$

while an equation for s_o can be obtained by equating the constant term. (The axial eikonal s_o is not needed to determine the intensity but it could be useful in determining the spectral output of a nonlinear beam.) Substituting Eq. (56) into Eq. (54) gives the following second-order equation for a,

$$\frac{d^2 a}{dz^2} = \frac{a \eta(0)}{\eta_0^2} \left(\frac{\partial^2 \eta}{\partial r^2} \right)_{r=0} + \frac{1}{k^2 a^3} \quad . \tag{57}$$

Equation (57) can be considered the equation for the radius of the laser beam. For a Gaussian beam the power in any cross-section falls off as $\exp(-r^2/a^2)$. The initial conditions require the beam radius a_o and the first derivative $da/dz = -a_o/R$. The total power delivered to the solid is

$$P = \frac{c}{4} a_o^2 E_o^2(t) \int_0^\infty \eta(\xi)\, \xi h^2(\xi)\, d\xi$$

$$\simeq \frac{c}{8} a_o^2 E_o^2(t)\, \eta_o \quad , \tag{58}$$

which determines $E_o(t)$, given a_o and the instantaneous total power P.

When η is given as a function $\eta = f(u)$, Eq. (57) can be written as

$$\frac{d^2 a}{dz^2} = \frac{a}{2\eta_o} \left(f(u) \frac{\partial f}{\partial u} \frac{\partial^2 u}{\partial r^2} \right)_{r=0} + \frac{1}{k^2 a^3} \quad , \tag{59}$$

and when u has the instantaneous form $u = \frac{1}{2} \eta_o E^2$, Eq. (59) becomes

$$\frac{d^2 a}{dz^2} = \frac{E_o^2 a_o^2}{\eta_o a^3} h(0)\, h''(0) \left(f(u) \frac{\partial f}{\partial u} \right)_{r=0} + \frac{1}{k^2 a^3} \quad , \tag{60}$$

where u at r = 0 has the value

$$u = \frac{1}{2} \eta_o E_o^2 \left(\frac{a_o}{a} \right)^2 h^2(0) \quad .$$

In the more general case, the computer program solves Eq. (59) where u is evaluated by knowing the value of E at a given point over its entire past history, and applying Eq. (30).

D. Numerical Methods

In the case where the beam-tracing equation is used with an instantaneous response mechanism, Wagner et al.[30] have noted that the equation has the same form as the equations of motion for a single particle in a potential well, which allows one to make use of analytical solutions for certain relationships between the index of refraction and the fieldstrength. The approach used in the computer program is to numerically integrate the equation, a procedure which allows us to be flexible in choosing different functions $\eta = f(u)$ and also to include response time effects which are incorporated in Eq. (30).

In the numerical computation the function $h(\xi)$ has been taken to be a Gaussian. The values of u on the axis at time t are stored at up to 400 positions along the center of the beam. The increments in u_i from t to $t + \Delta t$ are then calculated by a method which amounts to a finite difference expansion based on Eq. (30). However, this updating requires the values of the radius a at t and $t + \Delta t$, that are found simultaneously by integrating the beam-tracing equation (Eq. (40)) from the entrance face, this being accomplished by a fourth-order Runge-Kutta integration. During this integration, a test for accuracy is made and the step size in the integration is automatically divided by two so many times as is necessary until the criterion is met. An alternative program was written to use only the instantaneous version of Eq. (30) which gave a convenient method of testing the accuracy of the second program by letting the relaxation time in that program to be taken extremely small compared with the pulse duration. The instantaneous program and the program including relaxation are described in the next two sections.

E. Beam-Tracing Equation with an Instantaneous Response Mechanism

In order to be able to predict the field intensities along the track, two programs were written. The first program treats the case where the index of refraction along the track adjusts instantaneously to the applied field. The second program which will be described in Sec. IV-F treats the case where there is a time lag between the application of the optical field and the adjustment of the index of refraction along the trail. The first program is quicker to run and a can be operated with a larger step increment in the z-direction.

When relaxation effects are ignored the mathematical problem can be expressed in the form of Eq. (60) which can be rewritten as

$$\frac{\partial^2 a}{\partial z^2} = -\frac{\partial U}{\partial a} \quad , \tag{61}$$

where

$$U = \frac{h''(0)}{2h(0)} \left(\frac{f^2}{\eta_o^2} \right)_{r=0} + \frac{1}{2k^2 a^2} \quad , \tag{62}$$

where (for a Gaussian beam satisfying Eq. (45) so that $h''(0) = -h(0)$) Eqs. (61) and (62) are equivalent to Eqs. (2.16) and (2.17) of Wagner et al.,[30] except for an unimportant constant in the definition of U and a slight change of notation. (We use f/η_o for the ratio of the nonlinear diffraction index to the undisturbed index while they define $\epsilon_L + \chi$ as the susceptibility with constant magnetic permeability so that $1 + \chi/\epsilon_L = f^2/\eta_o^2$.)

If we let $p = da/dz$, Eq. (61) is easily integrated to give

$$\frac{1}{2} p^2 + U = E \quad , \tag{63}$$

where E, "the energy", is a constant as we move along the beam. It can now be easily recognized that Eq. (61) is equivalent to a particle moving in a one-dimensional conservative potential U, as noted by Wagner et al.,[30] or to the two-body central-force problem[38] where U is the fictitious potential, provided that we interpret z, the distance along the beam as time, and a, the radius of the beam, as position, with $p = da/dz$ playing the role of momentum. The identification of our problem with the standard problem of classical mechanics allows us to use our familiarity with these solutions in the beam-tracing problem. Wagner et al.[30] give a few illustrations of this. Another illustration is the "giant planet" instability; that is, it is known that a relatively small perturbation caused when a comet passes near a large planet may change the orbit in such a way that a previously captive comet may be thrown into an escape orbit. A similar effect happened in the original version of beam-tracing program in which we found that small numerical errors would cause the escape of a beam which had previously been trapped and had described several focal points; the inverse effect was probably possible in which a numerical error could cause a beam to be trapped even though its initial conditions should not have allowed this. This numerical problem was solved in the final version of the program by requiring the derivative da/dz to satisfy the constraint represented by Eq. (63).

Another illustration concerns an expression in common usage for the nonlinear index of refraction

$$\eta^2/\eta_o^2 = 1 + \frac{\eta_2}{\eta_o} \frac{E_o^2 a_o^2}{a^2} \quad , \tag{64}$$

which leads to the potential

$$U = -\frac{1}{2}\left(1 + \frac{\eta_2}{\eta_o}\,\frac{E_o^2 a_o^2}{a^2}\right) + \frac{1}{2k^2a^2} \quad ,$$

or equivalently by adding a constant to U, we replace U by

$$U' = \frac{1}{2k^2a^2}\left(1 - \frac{\eta_2}{\eta_o}\, k^2 E_o^2 a_o^2\right) \quad . \tag{65}$$

(Note that in Eq. (64) we have departed from the general form given by Eq. (28). Unfortunately, there is a great deal of confusion about these expansions. For example, Akhmanov et al.[28] state that they are expanding the index of refraction as $\eta = \eta_o + \eta_2 |A|^2 + \eta_4 |A|^4$ but when they apply this in their derivation of their Eq. (8) and thereafter, they have actually used the expansion

$$\frac{\eta^2}{\eta_o^2} = 1 + \frac{\eta_2}{\eta_o} |A|^2 + \frac{\eta_4}{\eta_o} |A|^4 \quad . \tag{66}$$

This means that the usual form keeping only the quadratic terms in Eq. (66) involves a fourth order term in the index of refraction. All this means is that Akhmanov et al.[28] have really expanded in terms of susceptibility like Wagner et al.[30] and there is really no physics lost, but the inconsistency can be confusing. In any case, our use of Eq. (64) allows our results to be directly comparable to Eq. (18) of Akhmanov and, by replacing η_2/η_o by ϵ'_2/ϵ_L, to Eq. (3.2) of Wagner et al.)

Now, it is immediately apparent from the analog with mechanics that, if the initial conditions at $z = 0$ are $a = a_o$ and $da/dz = a'_o$, the beam will be trapped only if

$$\frac{1}{2} a_o'^2 + U'(a_o) < 0 \quad , \tag{67}$$

in which case there are an infinite number of focal points. On the other hand, in the opposite case there will either be no focal points or, at most, one (if $a_o' / a_o < 0$). Now Akhmanov et al.[28] state conditions in which they claim there are exactly two focii. Actually they have introduced a spurious solution in going from their Eq. (19) to Eq. (20). Their Eq. (19) has the form

$$\left(\frac{df}{dz}\right)^2 = \frac{c_1}{f^2} + c_2 \quad , \tag{68}$$

where c_1 and c_2 are constants defined in their text.

An integration of Eq. (68) gives

$$z + \frac{1}{c_2}\sqrt{c_1 + c_2} = \frac{1}{c_2}\sqrt{c_1 + c_2 f^2} \quad , \tag{69}$$

with the boundary condition $f = 1$ at $z = 0$. Now, Akhmanov et al. give as the integral of Eq. (68) the result of squaring Eq. (69), that is

$$f^2 = c_2 z^2 + 2 (c_1 + c_2)^{1/2} z + 1 \quad , \tag{70}$$

which is also equivalent to Eq. (3.4) of Wagner et al.

At a focal point $f = 0$, so Akhmanov et al. assumes that the values of z at which focal points occur is obtained by setting the quadratic on the right-hand side of Eq. (70) equal to zero, which, for a positive discriminant, leads to two solutions. However, one of these solutions is spurious and only the solution corresponding to setting $f = 0$ in Eq. (69) can be real. Thus, the results plotted in Fig. 1 of reference 28 are incorrect. This error would be difficult to spot if we did not have guidance from the analogy with classical mechanics. (Since we have gone to some trouble pointing out small mistakes in Akhmanov et al.,[28] we should state that, taken as a whole, their paper is not only useful but also one of the important basic references in the theory of self-focusing.)

A listing of the program which was written to integrate the beam tracing program is given in Fig. 32 a-d. The shape of the pulse into the medium can be chosen arbitrarily by adjusting constants in the DATA statement in subroutine

```
C DT=TIME SAMPLE,NYET=NO OF FRAMES
C    THIS PROGRAM CALCULATES THE SELF FOCUSING OF A LASER BEAM
      COMMON HEX,CAP,H,DEE
      DIMENSION A(401),P(401),Z(401)   ,POW(12)
      NAMELIST/PARAM/ RELAX,E2,E4
      READ(5,PARAM)
      WRITE(6,PARAM)
      NAMELIST/CONTRO/ DT,NYET,LEGUP,NA,NB,LETS,NET,INTO
      READ (5,CONTRO)
      WRITE(6,CONTRO)
  600 READ(5,100)  G,       WL,R,AL,     AO
  100 FORMAT(5E10.4)
C  POWER IN MEGAWATTS,COEFFICIENTS IN CM/STVT,WVLENGTH INCM,RAD OF CUR
C    IN CM, LENGTH IN CM,NO OF POINTS,RADIUS OF BEAM IN CM
      PCRIT=.0030*WL*WL/64./3.14159/3.14159/E2     *2.
      H=AL/FLOAT(NET)
      NET1=NET+1
      GIM=G
      T=0.0
      ITIM=NYET*DT
      WRITE(6,903) ITIM
  903 FORMAT(1H1,25X,'TIME SEQUENCES FOR A',I3,' NANOSECOND PULSE'/)
      DO 5 I=1,NET1
      Z(I)=H*FLOAT(I-1)   + 0.1E-06
      A(I)=0.0
    5 P(I)=0.0
      DO 190 LOCK=1,NYET
      T=T+DT
      CALL POWER(T,PAT)
      G=GIM*PAT
      A(1)=AO
      P(1)=-AO/R
      CAP=   WL**2/4./3.14159/3.14159- 8.*G/0.003 *E2
      HEX= 64.*E4*(G/0.003 )**2
```

Fig. 32a Computer Program to Integrate the Beam Tracing Problem.

```
      OEE=   (AO/R)**2+(CAP +HEX/2./AO/AO)/AO/AO
      MIX=35
      DO 15 J=1,NET
      IF(MIX.NE.35) GO TO 832
      IF(A(J).LT.0.0) MIX=J
      IF((P(J)/R) .GT.0.0) MIX=J
  832 CONTINUE
      AN=A(J)
      PN=P(J)
      CALL RATE(AN,PN)
      A(J+1)=AN
   15 P(J+1)=     PN
      IF(MOD(LOCK,LETS).NE.0) GO TO 190
      WRITE(6,210) PCRIT,G,E2,E4,WL,R,AL,AO,NET
  210 FORMAT( 35X,16HCRITICAL POWER =,E12.4,2HMW/37X ,14HACTUAL POWER =,
     2    E12.4,2HMW/
     3 10X,10X,5HN2/NO,10X,5HN4/NO,5X,
     4                    10HWAVELENGTH,          6X,9HCURVATURE,
     5 9X,6HEXTENT, 6X,9HRADIUS AO,11X,
     6                                   4HMESH, /10X,6E15.5,I15/)
      LZ=0
      DO 413 M=NA,NB ,LEGUP
      LZ=LZ+1
  413 POW(LZ)=G/3.14159/A(M)**2
      WRITE(6,200) T,(Z(N),N=NA,NB ,LEGUP),   (A(N),N=NA,NB ,LEGUP),
     2                (P(N),N=NA,NB ,LEGUP),    (POW(N),N=1,11)
  200 FORMAT(26X,    'BEAM GEOMETRY WHEN T=' ,F6.2,'NANOSECONDS'
     2                                        /4X8HPOSITION,11F10.7/6X,6HRADIU
     3S,11E10.4/7X,5HSLOPE,11E10.4/4X,8HPOYNTING,11E10.4/4X,4HFLUX)
      LZ=MIX-6
      DO 199 M=1,11
      LZ=LZ+1
  199 POW(M)=  G/3.14159/A(LZ)**2
      LZ=  MIX-5
      LZ1=MIX+5
      WRITE(6,205)   (Z(N),N=LZ,LZ1        ),   (A(N),N=LZ,LZ1        ),
     2               (P(N),N=LZ,LZ1        ),    (POW(N),N=1,11)
  205 FORMAT(26X,    'GEOMETRY NEAR THE BEAM WAIST'
     2                                        /4X8HPOSITION,11F10.7/6X,6HRADIU
     3S,11E10.4/7X,5HSLOPE,11E10.4/4X,8HPOYNTING,11E10.4/4X,4HFLUX ///)
  190 CONTINUE
      INTO=INTO-1
      IF(INTO.GT.0) GO TO 600
      CALL EXIT
      END
```

Fig. 32b Computer Program to Integrate the Beam Tracing Problem.

```
      SUBROUTINE RATE(AN,PN)
      COMMON HEX,CAP,H,DEE
      F(Y)=(CAP*HEX/Y**2)/Y**3
      LAMB=1
      LETGO=1
      NOB=1
      QUAD=H
  115 CONTINUE
      T11=H*PN
      T12=F(AN)*H
      T21=H*(PN+0.5*T12)
      BY=AN+0.5*T11
      T22=F(BY) *H
      IF(((1.-T12/T22)**2).LT..01) GO TO 15
      IF((T22/PN)**2.LT. 0.1E-07)  GO TO 15
      IF(NOB.EQ.-1.AND.LAMB.EQ.1)
     2                 WRITE(6,139) LETGO      ,AN
      IF(NOB.EQ.-1)  LAMB=-1
  139 FORMAT(1X,30H SLIPPAGE                          ,13HLETGO EQUALS ,I5,
     2 E15.4)
      IF(NOB.EQ.-1) GO TO 15
      H=H/2.
      LETGO=2*LETGO
      GO TO 115
   15 CONTINUE
      NOB=-1
      T31=H*(PN+2.*T22-T12)
      BY=AN+2.*T21-T11
      T32=F(BY) *H
      AN=AN+(T11+4.*T21+ T31)/6.
      PN=PN+    (T12+4.*T22+    T32)/6.
      LETGO=LETGO-1
      IF(LETGO.GT.0) GO TO 115
      P2=DEE-(CAP*HEX/2./AN/AN)/AN/AN
      IF(P2.LT.0.0)  GO TO 53
      P2=SQRT(P2)
      PN=P2*ABS(PN)/PN
   53 H=QUAD
      RETURN
      END
```

Fig. 32c Computer Program to Integrate the Beam Tracing Problem.

```
      SUBROUTINE POWER (T,    PAT)
      DIMENSION TAU(10),FIT(10)
      DATA (TAU(N),N=1,5)/0.,10.,20.,30.,  50./,  (FIT(N),N=1,5) /0.,.7,.2,
     1.,0.0/ ,  M/5/
      N=1
   20 N=N+1
      IF(N.GT.M) GO TO 300
      IF(TAU(N).LT.T) GO TO 20
      PAT=  FIT(N-1)+(FIT(N)-FIT(N-1))*(T-TAU(N-1))/(TAU(N)-TAU(N-1))
      GO TO 400
  300 PAT=0.0
  400 RETURN
      END
```

Fig. 32d Computer Program to Integrate the Beam Tracing Problem.

POWER. The peak power in megawatts is entered by the READ statement in the main program, as is optical wavelength in cm inside the material, the geometrical radius of curvature of the beam at entry, the depth of the sample to which the calculations are to be carried out, and the effective radius of the Gaussian beam. The NAMELIST PARAM inputs the relaxation time in nanoseconds and the coefficients for the expansion from Eq. (28) in cm/statvolt. The NAMELIST CONTRO introduces the time increment DT in nanoseconds, NET, the total number of mesh points, and some additional control integers. A typical example of the input data cards is shown in Fig. 33. The output which gives the critical power for self-focusing and the actual power in the beam at a specified time, is shown in Fig. 34. The output gives the radius, slope and Poynting flux for the beam at fairly widely separated positions along the beam and also at closely spaced intervals near the beam waist (or at the focus if the beam radius actually reaches zero).

F. Numerical Methods for Integrating the Beam-Tracing Equation with a Finite Response Time Mechanism

In general, there will be a time lag after the application of the optical field before the index of refraction adjusts to its final value. Since the perturbation of the index of refraction remains along the path of the beam for some time after the optical field is reduced, this effect is also known as the residual trail effect. In our formulation, the temporal delay is given by Eq. (30). In the case where the index of refraction is dependent only on the quadratic term in the electric field, Eq. (30) is, in fact, equivalent to an integration of the differential relaxation equation given by Fleck and Kelly[39] and by Shen and Loy.[40] The expression for u is

$$u(r,z,t) = \frac{n_o a_o^2}{2\tau_o} \int_0^t \frac{E_o^2(\tau)}{a^2(z,t)} h^2\left(\frac{r}{a(z,t)}\right) e^{\left(-\frac{t-\tau}{\tau_o}\right)} d\tau \quad , \tag{71}$$

where we take h to be the Gaussian distribution $h^2 = \exp(-r^2/a^2)$. The beam-tracing equation is

```
@X QT
 $PA RA M
 R EL AX =0.1E-04,
 E2=0.2E-12,   E4=0.32E-23,
 $EN D
 $CO NT RO
 D T= 2.0,  NYE T= 13,
 L EG UP =40,  NA= 1,    NB=401,
 L ET S= 1,   NE T=400,
 I NT 0= 2,
 $EN D
   .211 +01   .1060-03   .25  +00   .5    +00   .5000-02
   .211 +01   .1060-03   .25  +00   .5    +00   .5000-02
@F IN
```

Fig. 33 An Example of the Input Data to the Beam Tracing Program.

TIME SEQUENCES FOR A 40 NANOSECOND PULSE
RELAXATION TIME IS .000 01

CRITICAL POWER = .2668 +01MW
ACTUAL POWER = .7000 +01MW

N2/N0	N4/N0	WAVELENGTH	CURVATURE	EXTENT	RADIUS A0
.2000 0-13	.8000 0-24	.1060 0-03	.4000 0+01	.6000 0+01	.2500 0-01

BEAM GEOMETRY WHEN T = 10.0 ONANOSECONDS

POSITION	3.0000 0-01	3.3000 0-00	3.6000 0-01	3.9000 0-00	4.2000 0-00	4.5000 0-00	4.8000 0-00	5.1000 0-00	5.4000 0-00
RADIUS	.5698-02	.3353-02	.1596-02	.4419-02	.6595-02	.8514-02	.1057-01	.1248-01	.1437-01
SLOPE	-.7231-02	-.8787-02	.1326-01	.7759-02	.6910-02	.6592-02	.6433-02	.6343-02	.6285-02
POWERING FLUX	.6962+05	.1981+06	.3749+06	.1141+06	.5123+05	.3003+05	.1996+05	.1431+05	.1078+05

GEOMETRY NEAR THE BEAM WAIST

POSITION	3.4850 0-01	3.4900 0-00	3.4950 0-01	3.5100 0-01	3.5250 0-00	3.5400 0-01	3.5550 0-00	3.5700 0-01	3.5850 0-00
RADIUS	.1047-02	.1445-02	.1228-02	.1001-02	.8067-03	.7769-03	.9459-03	.1170-02	.1390-02
SLOPE	-.1307-01	-.1399-01	-.1490-01	-.1487-01	-.9446-02	.6136-02	.1434-01	.1504-01	.1420-01
POWERING FLUX	.9210+06	.1068+07	.1479+07	.2222+07	.3424+07	.3692+07	.2490+07	.1627+07	.1153+07

CRITICAL POWER = .2668 +01MW
ACTUAL POWER = .2000 +01MW

N2/N0	N4/N0	WAVELENGTH	CURVATURE	EXTENT	RADIUS A0
.2000 0-13	.8000 0-24	.1060 0-03	.4000 0+01	.6000 0+01	.2500 0-01

BEAM GEOMETRY WHEN T = 20.0 ONANOSECONDS

POSITION	3.0000 0-01	3.3000 0-00	3.6000 0-01	3.9000 0-00	4.2000 0-00	4.5000 0-00	4.8000 0-00	5.1000 0-00	5.4000 0-00
RADIUS	.5332-02	.4216-02	.2785-02	.1512-02	.2114-02	.3743-02	.5534-02	.7369-02	.9222-02
SLOPE	-.5114-02	-.5369-02	-.5441-02	-.1908-02	.4700-02	.5828-02	.6068-02	.6153-02	.6191-02
POWERING FLUX	.1588+05	.3122+05	.8208+05	.2785+06	.1424+06	.4545+05	.2078+05	.1172+05	.7486+04

GEOMETRY NEAR THE BEAM WAIST

POSITION	3.9700 0-01	3.9150 0-01	3.9300 0-00	3.9450 0-01	3.9600 0-00	3.9750 0-01	3.9900 0-00	4.0050 0-00	4.0200 0-00
RADIUS	.1512-02	.1486-02	.1467-02	.1454-02	.1448-02	.1449-02	.1457-02	.1472-02	.1493-02
SLOPE	-.1308-02	-.1520-02	-.1070-02	-.6233-03	-.1669-03	.2922-03	.7465-03	.1189-02	.1613-02
POWERING FLUX	.2785+06	.2982+06	.2959+06	.3010+06	.3035+06	.3031+06	.2998+06	.2939+06	.2857+06

Fig. 34 An Example of the Beam Tracing Program Output. The critical power for self-focusing and the actual power in the beam at several times is given.

$$\frac{\partial^2 a}{\partial z^2} = \frac{a}{n_o^2}\left(f(u)\frac{\partial f}{\partial u}\left(\frac{\partial^2 u}{\partial r^2}\right)_{r=0}\right) - \frac{1}{k^2 a^3} \quad , \tag{72}$$

and, from Eq. (71) we find that Eq. (72) must be solved simultaneously with the equations

$$u(0,z,t) = \frac{4}{c\tau_o}\int_0^t \frac{P(\tau)}{a^2(z,\tau)}\, e^{-\frac{t-\tau}{\tau_o}}\, d\tau \quad , \tag{73}$$

and

$$u'' = \frac{\partial^2 u}{\partial r^2}_{r=0} = -\frac{8}{c\tau_o}\int_0^t \frac{P(\tau)}{a^4(z,\tau)}\, e^{\left(-\frac{t-\tau}{\tau_o}\right)}\, d\tau \quad . \tag{74}$$

In Eqs. (73) and (74) $P(\tau)$ is the instantaneous power, which should, strictly speaking be replaced by $P(\tau - z/c)$. The exact form is not necessary in our experimental setup where the thickness of the crystal L always satisfies

$$L \ll c\, P(\tau)/P'(\tau) \quad , \tag{75}$$

but for thick crystals there are some interesting effects as shown by Shen and Loy[40] in which the focal spot can move with a (virtual) velocity which exceeds the speed of light.

The mathematical problem requires us to solve the two integrals from Eq. (73) and (74) simultaneously with the differential equation, Eq. (72), with an arbitrary pulse of power P(t). The listing for the program which has been written to numerically do this is shown in Fig. 35a-d. The values of Eq. (73) and (74) are stored at each mesh point (i.e., position z_i) at a given time t and then updated to time t + dt. The beam tracing equation is then integrated forward starting from z = 0 into the interior of the solid. Since we are not able to take advantage of the

```
C DT=TIME SAMPLE,NYET=NO OF FRAMES
C   THIS PROGRAM CALCULATES THE SELF FOCUSING OF A LASER BEAM
      DIMENSION        P(401),Z(401)   ,POW(12)
      COMMON HEX,CAP,H ,WL ,WILLY
      COMMON/BAND/ G,GNEW,X ,EO ,NET1     ,PILL,POOBA,PILLOW
      COMMON/BANK/ E2,E4
      COMMON/SETUP/ A(401),U(401) ,AST(401) , UR(401)
      NAMELIST/PARAM/ RELAX,E2,E4
      READ(5,PARAM)
      WRITE(6,PARAM)
      NAMELIST/CONTRO/ DT,NYET,LEGUP,NA,NB,LETS,NET,INTO
      READ (5,CONTRO)
      WRITE(6,CONTRO)
  500 READ(5,100)  G,       WL,R,AL,     AO
  100 FORMAT(5E10.4)
C  POWER IN MEGAWATTS,COEFFICIENTS IN CM/STVT,WVLENGTH INCM,RAD OF CUR
C    IN CM, LENGTH IN CM,NO OF POINTS,RADIUS OF BEAM IN CM
      X=DT/RELAX
      ED=EXP(-X)
      WILLY=(WL/6.28318)**2
      PILL=4./.003*(1.-EO)
      POOBA=4./.003*(1.-(1.-ED)/X)
      PILLOW=4./.003*(1.-EO*(1.+X))/X
      PCRIT=.0030*WL*WL/64./3.14159/3.14159/E2    *2.0
      H=AL/FLOAT(NET)
      NET1=NET+1
      GIM=G
      T=0.0
      ITIM=NYET*DT
      WRITE(6,903) ITIM ,RELAX
  903 FORMAT(1H1,25X,'TIME SEQUENCES FOR A',I3,' NANOSECOND PULSE'/
     245X,'RELAXATION TIME IS ',F10.5//)
      DO 5 I=1,NET1
      Z(I)=H*FLOAT(I-1)   + 0.1E-06
      U(I)=0.0
      A(I)=AO
      UR(I)=0.0
    5 P(I)=0.0
      GNEW=0.0
      DO 190 LOCK=1,NYET
      T=T+DT
      G=GNEW
      CALL POWER(T,PAT)
      GNEW=GIM*PAT
      A(1)=AO
      P(1)=-AO/R
      CAP=WILLY          -8.*GNEW              /0.003 *E2
      HEX= 64.*E4*(GNEW/.003)**2
      MIX=35
      DO 533 J=1,NET1
      UR(J)=UR(J)*EO
  533 U(J)=U(J)*EO
      CALL YEW(0)
      DO 515 J=1,NET
      IF(MIX.NE.35) GO TO 832
      IF(A(J).LT.0.0) MIX=J
      IF((P(J)/R) .GT.0.0) MIX=J
```

Fig. 35a Computer Program to Integrate the Coupled Relaxation Equations for Beam Tracing with Finite Response Time.

```
832 CONTINUE
    ZN=Z(J)
    UN=U(J)
    UN1=U(J+1)
    URN=UR(J)
    URN1=UR(J+1)
    AN=A(J)
    PN=P(J)
    CALL        RATE(AN,PN,UN,UN1,URN,URN1,ZN)
    A(J+1)=AN
515 P(J+1)=     PN
    CALL YEW(1)
    IF(MOD(LOCK,LETS).NE.0) GO TO 190
    WRITE(6,210) PCRIT,GNEW,E2,  E4,WL,R,AL,AO,NET
210 FORMAT( 35X,16HCRITICAL POWER =,E12.4,2HMW/37X ,14HACTUAL POWER =,
   2    E12.4,2HMW/
   3 10X,10X,5HN2/NO,10X,5HN4/NO,5X,
   4                    10HWAVELENGTH,          6X,9HCURVATURE,
   5 9X,6HEXTENT, 6X,9HRADIUS AO,11X,
   6                                  4HMESH, /10X,6E15.5,I15/)
    LZ=0
    DO 413 M=NA,NB ,LEGUP
    LZ=LZ+1
413 POW(LZ)= GNEW/3.14159/A(M)**2
    WRITE(6,200) T,(Z(N),N=NA,NB ,LEGUP),   (A(N),N=NA,NB ,LEGUP),
   2                (P(N),N=NA,NB ,LEGUP),    (POW(N),N=1,11)
200 FORMAT(26X,    'BEAM GEOMETRY WHEN T=' ,F6.2,'NANOSECONDS'
   2                                        /4X8HPOSITION,11F10.7/6X,6HRADIU
   3S,11E10.4/7X,5HSLOPE,11E10.4/4X,8HPOYNTING,11E10.4/4X,4HFLUX)
    LZ=MIX-6
    DO 199 M=1,11
    LZ=LZ+1
199 POW(M)= 1./3.14159/A(LZ)**2  *GNEW
    LZ=  MIX-5
    LZ1=MIX+5
    WRITE(6,205)   (Z(N),N=LZ,LZ1       ),   (A(N),N=LZ,LZ1       ),
   2               (P(N),N=LZ,LZ1       ),    (POW(N),N=1,11)
205 FORMAT(26X,    'GEOMETRY NEAR THE BEAM WAIST'
   2                                        /4X8HPOSITION,11F10.7/6X,6HRADIU
   3S,11E10.4/7X,5HSLOPE,11E10.4/4X,8HPOYNTING,11E10.4/4X,4HFLUX )
    DP1=P(MIX)-P(MIX-1)
    ZIP=Z(MIX) -P(MIX)   / DP1*H
    AZIP=A(MIX)+P(MIX)*(ZIP-Z(MIX))+DP1 /2.*(ZIP - Z(MIX))**2/H
    DIGBY=GNEW/3.14159/AZIP/AZIP
    WRITE(6,899)    ZIP,AZIP,DIGBY
899 FORMAT(40X,'WAIST IS AT',F10.5,'CM'/ 16X,'WAIST RADIUS IS ',F10.5,
   2'CM , POWER FLUX IS',E11.3,'MW/SQ. CM'///)
190 CONTINUE
    INTO=INTO-1
    IF(INTO.EQ.11      RELAX=5.0
    IF(INTO.GT.0) GO TO 600
    CALL EXIT
    END
```

Fig. 35b Computer Program to Integrate the Coupled Relaxation Equations for Beam Tracing with Finite Response Time.

```
      SUBROUTINE RATE(AN,PN,UN,UN1,URN,URN1,ZN)
      COMMON HEX,CAP,H ,WL ,WILLY
      COMMON/BANK/ E2,E4
      COMMON/BAND/ G,GNEW,X ,ED ,NET1     ,PILL,POOBA,PILLOW
      Q(UD)=(1.+UD*(E2-E4*UD))   *(E2-2.*E4*UD)
      F(Y,UD,UDR)=WILLY/Y**3     -Q(UD)*Y*UDR
      LAMB=1
      LETGO=1
      NOB=1
      QUAD=H
      GRAND=(UN1-UN)/QUAD
      GRIM=(URN1-URN)/QUAD
      ZEB=ZN
  115 CONTINUE
      T11=H*PN
      UD=UN+GRAND     *(ZEB-ZN)
      UDR=URN+GRIM*(ZEB-ZN)
      BY=AN
      CLINK=POOBA*GNEW/BY**2
      UD=UD+CLINK
      UDR=UDR+2.*CLINK   /BY**2
      T12=F(AN,UD,UDR)*H
      T21=H*(PN+0.5*T12)
      ZEB=ZEB+H/2.
      UD=UN+GRAND     *(ZEB-ZN)
      UDR=URN+GRIM*(ZEB-ZN)
      BY=AN+0.5*T11
      CLINK=POOBA*GNEW/BY**2
      UD=UD+CLINK
      UDR=UDR+2.*CLINK   /BY**2
      T22=F(BY,UD,UDR)*H
      IF(((1.-T12/T22)**2).LT..005)     GO TO 15
      IF((T22/PN)**2.LT.0.1E-07)    GO TO 15
      IF(LETGO.GT.256.AND.NOB.EQ.1)
     2                 WRITE(6,139) LETGO      ,AN
      IF(NOB.EQ.-1)  LAMB=-1
  139 FORMAT(1X,30H SLIPPAGE                              ,13HLETGO EQUALS ,I5,
     2 E15.4)
      IF(NOB.EQ.-1) GO TO 15
      H=H/2.
      ZEB=ZN
      LETGO=2*LETGO
      GO TO 115
   15 CONTINUE
      NOB=-1
      T31=H*(PN+2.*T22-T12)
      ZEB=ZEB+H/2.
      UD=UN+GRAND     *(ZEB-ZN)
      UDR=URN+GRIM*(ZEB-ZN)
      BY=AN+2.*T21-T11
      CLINK=POOBA*GNEW/BY**2
      UD=UD+CLINK
      UDR=UDR+2.*CLINK   /BY**2
      T32=F(BY,UD,UDR)*H
      AN=AN+(T11+4.*T21+ T31)/6.
      PN=PN+    (T12+4.*T22+    T32)/6.
      LETGO=LETGO-1
      IF(LETGO.GT.0) GO TO 115
      H=QUAD
```

Fig. 35c Computer Program to Integrate the Coupled Relaxation Equations for Beam Tracing with Finite Response Time.

```
      SUBROUTINE POWER (T,    PAT)
      DIMENSION TAU(10),FIT(10)
      DATA (TAU(N),N=1,7)/0.,.5,.7,.10.,.15.,.20.,.25./,
     2 (FIT(N),N=1,7)/0.,.7,1.,.0.8,0.5,0.1,0./,M/7/
      N=1
   20 N=N+1
      IF(N.GT.M) GO TO 300
      IF(TAU(N).LT.T) GO TO 20
      PAT=  FIT(N-1)+(FIT(N)-FIT(N-1))*(T-TAU(N-1))/(TAU(N)-TAU(N-1))
      GO TO 400
  300 PAT=0.0
  400 RETURN
      END
```

```
      SUBROUTINE YEW(NOK)
      COMMON/SETUP/ A(401),U(401) ,AST(401) , UR(401)
      COMMON/BAND/ G,GNEW,X ,EO ,NET1     ,PILL,POOBA,PILLOW
      IF(NOK.EQ.1) GO TO 99
      DO 20 J=1,NET1
      UR(J)=UR(J)+2.*PILLOW*G    /A(J)**4
   20 U(J)=U(J)+PILLOW*G/     A(J)**2
      RETURN
   99 DO 35 J=1,NET1
      UR(J)=UR(J)+2.*POOBA *GNEW/A(J)**4
   35 U(J)=U(J)   +    POOBA                    * GNEW/A(J)**2
      RETURN
      END
```

Fig. 35d Computer Program to Integrate the Coupled Relaxation Equations for Beam Tracing with Finite Response Time.

fictitious potential approach in this program, some experimentation is usually necessary in choosing the mesh size in the z-direction small enough (the mesh size is H = AL/NET where AL is the slab thickness) in order to prevent instabilities of the "giant planet" type.

Some results are shown in Sec. IV-G comparing a solid with a response time of 5 nanoseconds and one having an instantaneous response time.

G. Numerical Examples

The program was carried out for some examples using the following parameters

$$\eta_o = 1.0$$
$$\eta_2 = 2.0 \times 10^{-13} \quad \text{cm}^2/\text{statvolt}$$
$$\eta_4 = 3.2 \times 10^{-24} \quad \text{cm}^4/\text{statvolt}^2$$

where

$$\eta = \eta_o + \eta_2 u - \eta_4 u^2 \quad .$$

Figure 36a shows the pulse shape, which approximates an experimental pulse while Fig. 36b shows the focal position as a function of time for an entrance face beam radius of 0.184 mm and a beam convergence angle of 73.6 milliradians which would imply a geometrical optics focus at 0.25 cm. This corresponds to an experimental geometry. The relaxation time τ_o was taken to be a very small (10^{-14} seconds) compared to the pulse time.

In Fig. 37 we show the computed focal position for τ_o = 5 nanoseconds for the same pulse shape and physical parameters used in Fig. 36. In this example the entrance face beam radius was taken as 0.05 mm and the convergence

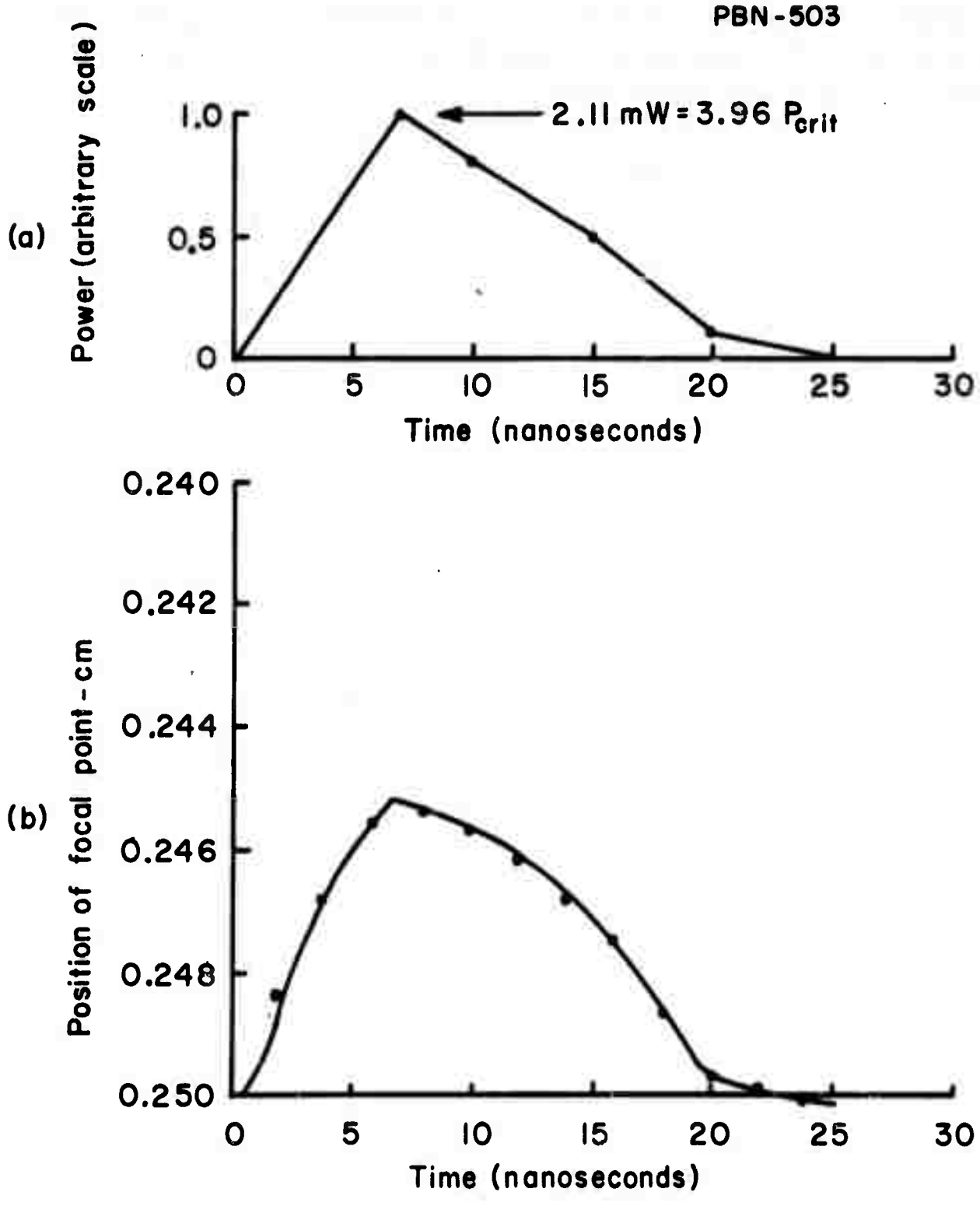

Fig. 36 Calculated Distance of the Focal Point From Entrance Face as a Function of Time for an Initial Beam Radius of 0.184 mm and a Convergence Angle of 73.6 Milliradians.

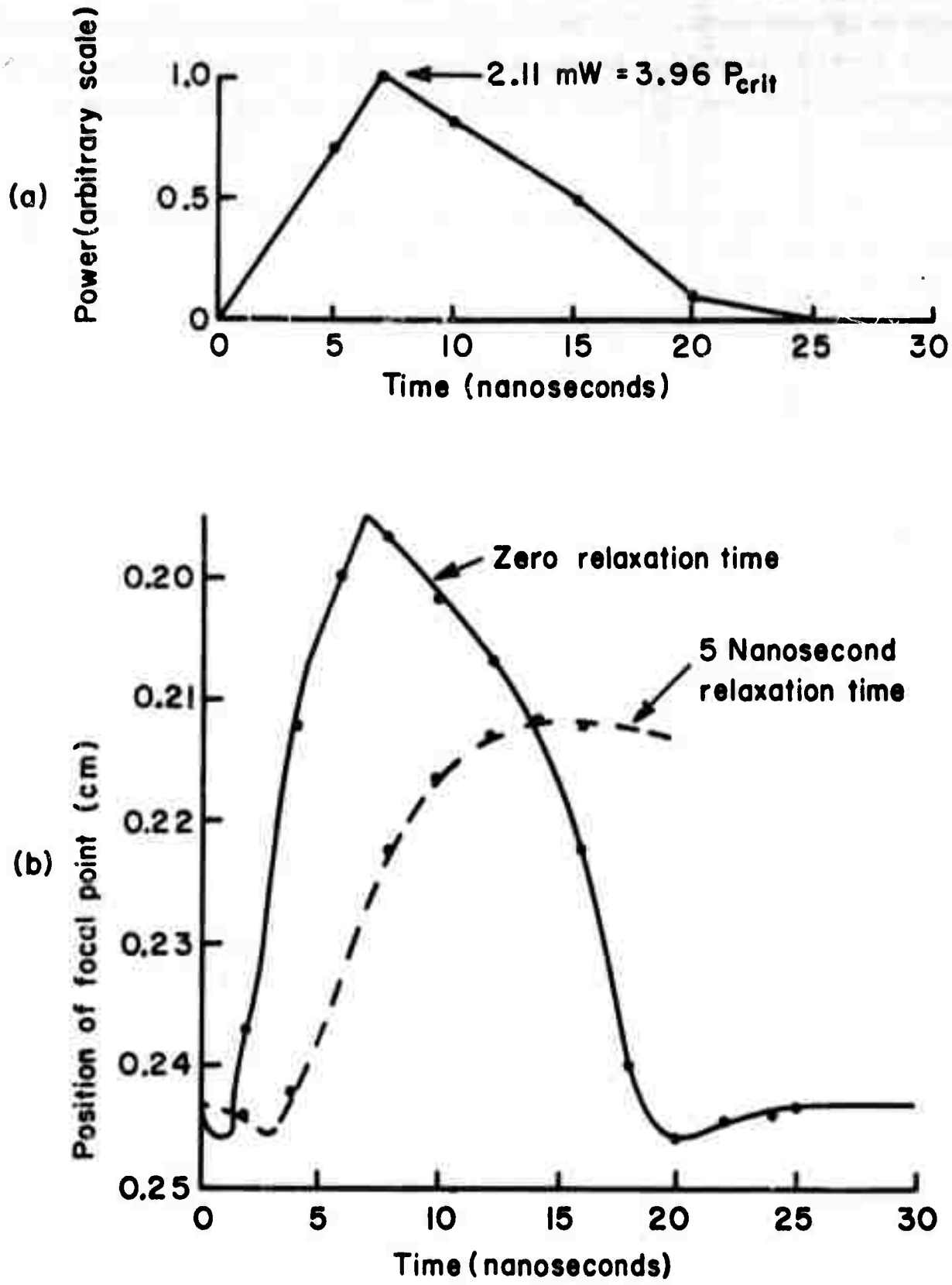

Fig. 37 Calculated Distance of the Focal Point from Entrance Face as a Function of Time for an Initial Beam Radius of 50 μm and a Convergence Angle of 20 Milliradians.

angle as 20 milliradians. The focal length moves in toward the entrance surface as the power increases but the shortest focal length is attained considerably after the power reaches its maximum in contrast to the result for an instantaneous response.

The beam radius as a function of position is plotted in Fig. 38 for the case of instantaneous relaxation at a time 4 nanoseconds after the start of the pulse when the instantaneous total power is 1.18 MW. Since P is greater than P_{crit} (where P_{crit} is defined as the power at which the quadratic term in E^2 is balanced by the diffraction term), the beam is initially self-focused, but when beam radius is less than 3 microns the η_4 term finally dominates and causes the beam to diverge once more. Trapping is much less effective for the form given by Eq. (28) than it is for the more realistic index of refraction given by Eq. (29), which gives the correct saturation limit.

Another situation of experimental interest was a collimated beam which had an entrance beam radius of 313μm. With a power of 1.97 MW, which was nearly four times the critical power of 0.53 MW, the convergence was extremely slow and the beam had converged only to 300μm after 10 cm travel, a beam length large compared with the actual sample size. This result was in agreement with the experimental results, in that no indication of self-focusing could be found with this beam geometry.

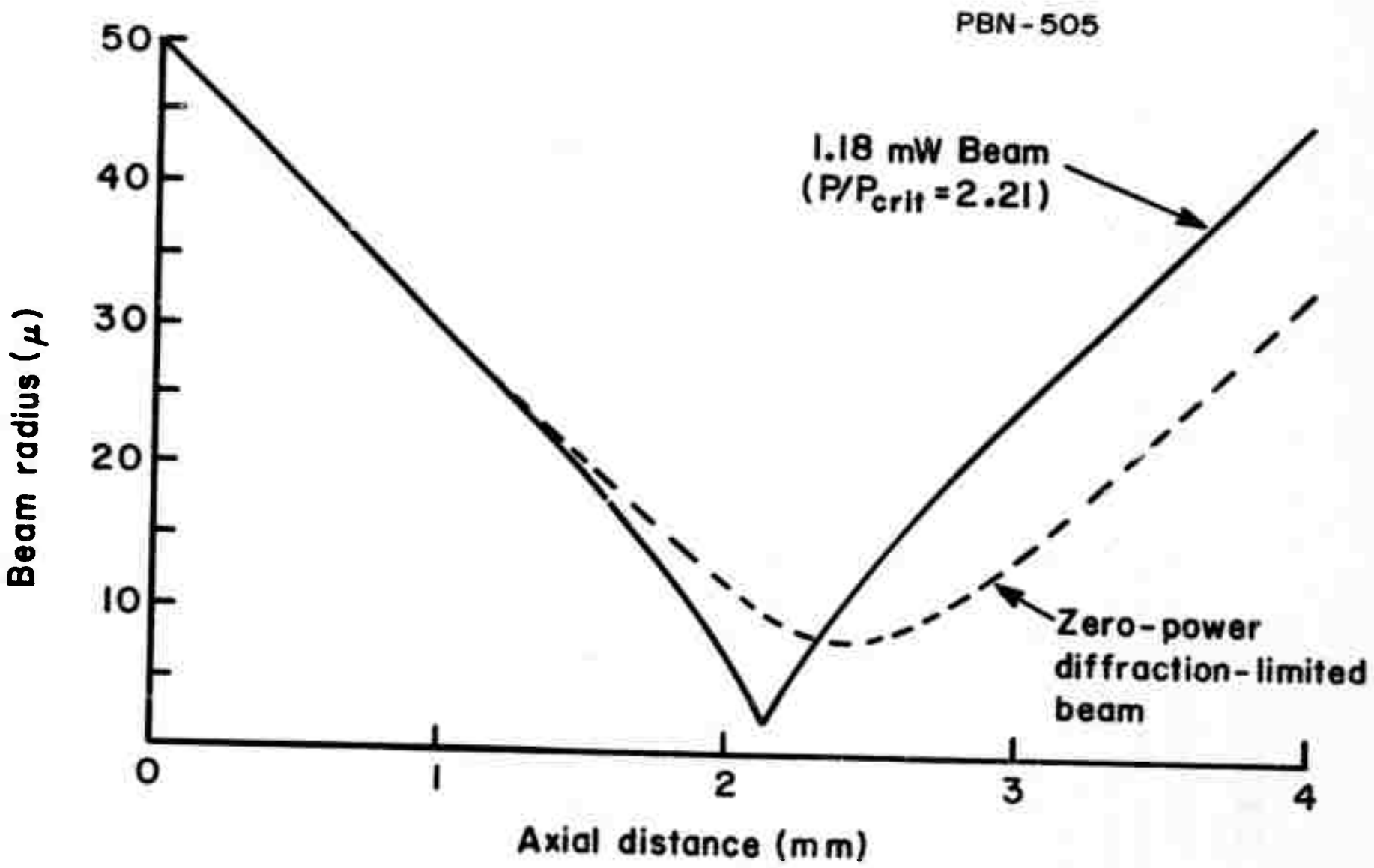

Fig. 38 Calculated Beam Radius as a Function of Axial Distance for a Beam with Power Equal to 2.21 P_{crit} and for a Linear Beam.

V. CONCLUSIONS

The objective of this program is to determine how and why permanent damage is produced and to find means to minimize or avoid its deleterious effects on laser systems. The work to date can be grouped into three general areas: 1, studies of the residual damage after irradiation using optical and electron microscopy, 2, studies of the dynamics of the damage process using high speed streak photography and 3, determination of the probability that a particular material. The following list summarizes the major results reached to date:

1. Residual damage was found only after the laser irradiation caused a visible spark when passing through the sample.

2. The importance of uniform ("hot spot" free) illumination in increasing the ability of a material to withstand laser irradiation was demonstrated by comparing TEM_{00} and multimode damage.

3. Contrary to previously held opinions, when $LiNbO_3$ and KDP are used as Pockel's cell or frequency doubler crystals, internal damage is produced at the same or lower levels of irradiation than those required to produce surface damage.

4. The laser beam's focusing conditions determine the form of the residual damage; that is, whether it is internal, entrance or exit face damage.

5. Internal filamentary damage in $LiNbO_3$ was found to be composed of a series of very fine, nearly planar cracks which intersect to form one or more long lines having diameter $\approx 0.4\,\mu m$. When illuminated with visible light, diffraction effects make these lines appear blurred and give the impression of a "tube" of damaged material.

6. Experiments designed to study the dynamics of damage formation by photographing the laser induced breakdown (the spark) with an image converter streak camera were initiated. The results of these measurements showed that when light is focused inside the material the first damage to occur is near the focal point and additional damage occurs upstream at later times. All laser-induced internal breakdowns were initiated during intervals of time when the level of irradiation increased or was maximum, and never when the intensity decreased.

7. A model for the results in 6 was developed in which self focusing was identified as likely to be responsible for the upstream movement of the sparks and a fast response self-focusing process was shown to be able to explain the fact that internal breakdowns were only produced when the pulse intensity increased. The importance of beam geometry and non-self-focusing configurations were investigated.

8. There is, in general, no sharp threshold for laser induced damage. There is, however, some probability that a particular pulse will damage a particular material. At very high levels of irradiation this probability is unity, at lower levels it is less than one and at very low levels the probability for damage may be vanishingly small. This was studied with both Nd:YAG and ruby lasers.

9. Measurements of the dependence of damage probability on the laser beam's power density for ten different materials have led to a model for the damage mechanism based on avalanche breakdown. Good qualitative agreement has been obtained.

10. Using the streak camera, preliminary measurements of the distribution of breakdown starting times as a function of damage probability have been obtained. These data show that the most likely time for a breakdown to occur is before the peak of the laser pulse. This data may be explained using the probabilistic interpretation of laser induced damage.

REFERENCES

1. The sample was a $LiNbO_3$ sample boule No. LN372 obtained from the Harshaw Chemical Company. This material was grown from a congruent melt.

2. E.L. Kerr, "Laser-Beam Self-Focusing and Glass Damage Caused by Electrostrictively Driven Acoustic Waves," Damage in Laser Glass, ASTMSTP 469, American Society for Testing and Materials, 1969, pp. 23-42.

3. E.S. Bliss, "Laser Damage Mechanisms in Transparent Dielectrics," ibid. pp. 9-22.

4. F.W. Quelle, "Self-Focusing in Glass," ibid. pp. 110-116.

5. G.M. Zverev, E.K. Maldutis and V.A. Pashkov, ZhETF Pis. Red. 9, 108 (1969).

6. The use of SEM techniques in damage studies in ruby is also described by C.R. Giuliano, R.W. Hellwuth, L.D. Hess and G.R. Rickel, "Damage Threshold Studies in Laser Crystals," Semi-Annual Report No. 1 for Contract No. F19728-69-C-0277.

7. V.V. Zhdanova, V.P. Klyziev, V.V. Lemanov, I.A. Smirov and V.V. Tikhov, Sov. Phys. Solid State 10, 1360 (1968).

8. I.A. Fersman and L.D. Khazov, Sov. Phys. Tech. Phys. 15, 834 (1970).

9. M.A. Duguay, J.W. Hansen and S.L. Shapiro, IEEE J. of Quantum Electronics QE-6, 725 (1970).

10. If $N \approx 1/p_1$, the quantity $(1 - p_1)^{N-1} \approx (1 - p_1)^{1/p_1}$ has the limit e^{-1} as $p_1 \rightarrow 0$.

11. Union Carbide Crystal No. T1N 348C1.

12. A. Wasserman, Appl. Phys. Letters 10, 132 (1967).

13. E.A. Sviridenkov, Sov. Phys. Sol. St. 9, 1917 (1968).

14. G.M. Zverev, T.M. Mikhailova, V.A. Pashkov, N.M. Soloveva, Sov. Phys. JETP 26, 1053 (1968).

15. R.W. Hellwarth, Proc. ASTM Symp. on Laser Damage, Boulder, Colorado (1970).

16. For a review see J.J. O'Dwyer Phil. Mag. Suppl. 7, 349 (1958).

REFERENCES (CONT'D)

17. A.G. Chynoweth, Phys. Rev. 109, 1537 (1959) and J. Appl. Phys. 31, 1161 (1960).

18. For a review see A. VonHippel, "Molecular Science and Molecular Engineering," (Technology Press and Wiley, New York, 1959) especially Chapter 5.

19. W. Shockley, Czech J. Phys. B11, 81 (1961) and Sol. St. Elec. 2, 35 (1961).

20. P.A. Wolff, Phys. Rev. 95, 1415 (1954).

21. G.A. Baraff, Phys. Rev. 128, 2507 (1962).

22. L.V. Keldysh, Sov. Phys. JETP 21, 1135 (1965).

23. C.R. Giuliano, D.F. Dubois and G.R. Rickel, "Damage Threshold Studies in Laser Crystals," Semiannual Report No. 4 for Contract No. F19628-69-C-0277, July 1971.

24. E.O. Kane, Phys. Rev. 159, 624 (1967).

25. This requires the presence of the applied field and so damage will only occur if breakdown is reached before the field turns off. The temporal properties of damage and avalanche breakdown will be discussed elsewhere.

26. An alternative damage mechanism is one in which the initiating electron is produced by internal field emission (tunneling from valence to conduction band), after which breakdown occurs with high probability. This again leads to a dependence like Eq. (3),but then K does not involve ℓ.

27. H.P.R. Fredrikse, W.R. Holser, and W.R. Thurbur, Phys. Rev. 143, 648 (1966).

28. S.A. Akhmanov, A.P. Sukhorukov and R.V. Khoklov, "Self Focussing and Self-Trapping of Intense Light Beams in a Nonlinear Medium," Soviet Physics JETP, 23, 1025 (1966).

29. P.K. Tien, J.P. Gordon and J.R. Whinnery, "Focussing of a Light Beam of Gaussian Field Distribution in Continuous and Periodic Lens-Like Media," Proc. of the IEEE 53, 129 (1965).

30. W.G. Wagner, H.A. Haus, and J.H. Marburger, "Large Scale Self-Trapping of Optical Beams in the Paraxial Ray Approximation," Phys. Rev. 175, 256 (1968).

31. E.L. Kerr, "Laser Beam Self-Focusing and Glass Damage Caused by Electrostrictivity Driven Acoustic Waves," in Damage in Laser Glass, ASTM Special Technical Publication, 23, (1969).

REFERENCES (CONT'D)

32. E.L. Kerr, "Track Formation in Optical Glass Caused by Laser Beam Self-Focusing," AFCRL-70-0599, Perkin-Elmer Report No. 9878 (1970).

33. L.I. Sedov, "Similarity and Dimensional Methods in Mechanics," (Cleaver-Hume Press, London, 1959).

34. L.H. Holway, "Self Similar Flow of Blast Waves," Technical Report ESRN-10, SURANO Advanced Development Laboratory, Raytheon Co., (1960).

35. L.H. Holway, "Similarity Model of an Explosion in a Rarefied Atmosphere," Phys. Fluids 12, 2506 (1969).

36. L.D. Landau and E.M. Lifshitz, "Theory of Elasticity," (Addison-Wesley Publishing Co., Reading, 1959).

37. P.M. Morse and H. Feshback, "Methods of Theoretical Physics," Vol. I (McGraw-Hill Book Co., Inc., New York, 1953).

38. H. Goldstein, Classical Mechanics (Addison-Wesley Publishing Co., Inc., Cambridge, Mass., 1953) p. 63.

39. J.A. Fleck and P.R. Kelley, Appl. Phys. Letters 15, 313 (1969).

40. Y.R. Shen and M.M.T. Loy, Phys. Rev. A3, 2099 (1971).

APPENDIX A

THERMAL SELF-FOCUSING IN $LiNbO_3$*

The self-focusing mechanisms for solids most often mentioned are 1) electro-striction[2] and 2) the thermal-heating-induced index-of-refraction changes.[4] In the former, the index of refraction in the irradiated region increases due to the electrostrictively induced stress and the beam is focused. In the latter if the index of refraction increases with temperature, and if there is some absorption process whereby the medium's temperature can be increased, then the beam can be focused.

To see if self-focusing due to thermal effects can be significant in $LiNbO_3$, the absorption in this material at the laser wavelength had to be measured. If the absorption per centimeter in the material is β, the volume V will be heated by $\Delta T = \beta \mathcal{E}/VC$ by the passage of a pulse of light of energy $\mathcal{E}$. C is the specific heat in joules per cm^3 per °K and the pulse duration is assumed so short that thermal conductivity can be neglected.

In $LiNbO_3$ the focal volume of a typical lens used in this work will be heated one centigrade degree by a 1 mJ pulse if

$$\beta = 0.001 \text{ cm}^{-1} \quad .$$

Since so small an absorption cannot be measured using conventional spectrophotometry (i.e., in a device such as a Cary 14 Dual Beam Spectrophotometer) the following very sensitive procedure was developed. If heating due to absorption at 1.06 μm occurred, than a $LiNbO_3$ crystal which was used as an "a-axis" frequency-doubler would require continuous temperature adjustment. If such a crystal were fixed at a

---

*The measurements described in this section were performed as part of work for the Electronics Research Center under NASA Contract NAS12-2155.

temperature below the index-matching temperature T_m, and then exposed to light at 1.06 μm, the heating due to absorption could be detected by monitoring the increase in harmonic output as the temperature of the irradiated volume rose to T_m. Since the initial temperature and the index-matching temperature are known, the absorption can be estimated by measuring the incident laser power and the time required to reach T_m. This type of experiment was performed using "hot" $LiNbO_3$ and the resulting data, the expected "sin Kt/Kt", function is shown in Fig. A-1. A 10-pps pulsed Nd:YAG laser was used. The average power was 1W at 1.06 μm, the maximum harmonic power was 0.005 W and the irradiated volume was a cylinder 1.5 cm long and ~ 0.5 cm in diameter. When the average laser power was ~ 0.1 W and the harmonic power was ~ 0.02 W, no appreciable heating was observed. Thus the heating is due to 1.06 μm absorption, and so by neglecting the thermal conductivity of the material the smallest absorption which could give the requisite temperature increase is found to be $\beta \approx 0.002\ cm^{-1}$.

The possibility that thermal effects can lead to self-focusing in $LiNbO_3$ crystals therefore cannot be ruled out. In fact, since most application involve laser pulses of many milijoules, this possibility must be included in any analysis of damage in $LiNbO_3$. Similar consideration must be given other materials of interest.

It is appropriate to ask whether the absorption described above should account for the melting observed in Figs. 12-14. The melting point of $LiNbO_3$ is 1260°C and the absorption coefficient at 1.06 μm is $\approx 0.002\ cm^{-1}$. Thus the entire pulse energy would have to be absorbed in the 0.006 cm diameter by ~ 1 μm deep crater in Fig. 12, to achieve a temperature increase to the melting point of $LiNbO_3$. However, since the absorption coefficient is so small, it is extremely unlikely that the pulse can be completely absorbed in the first 1 μm of material.

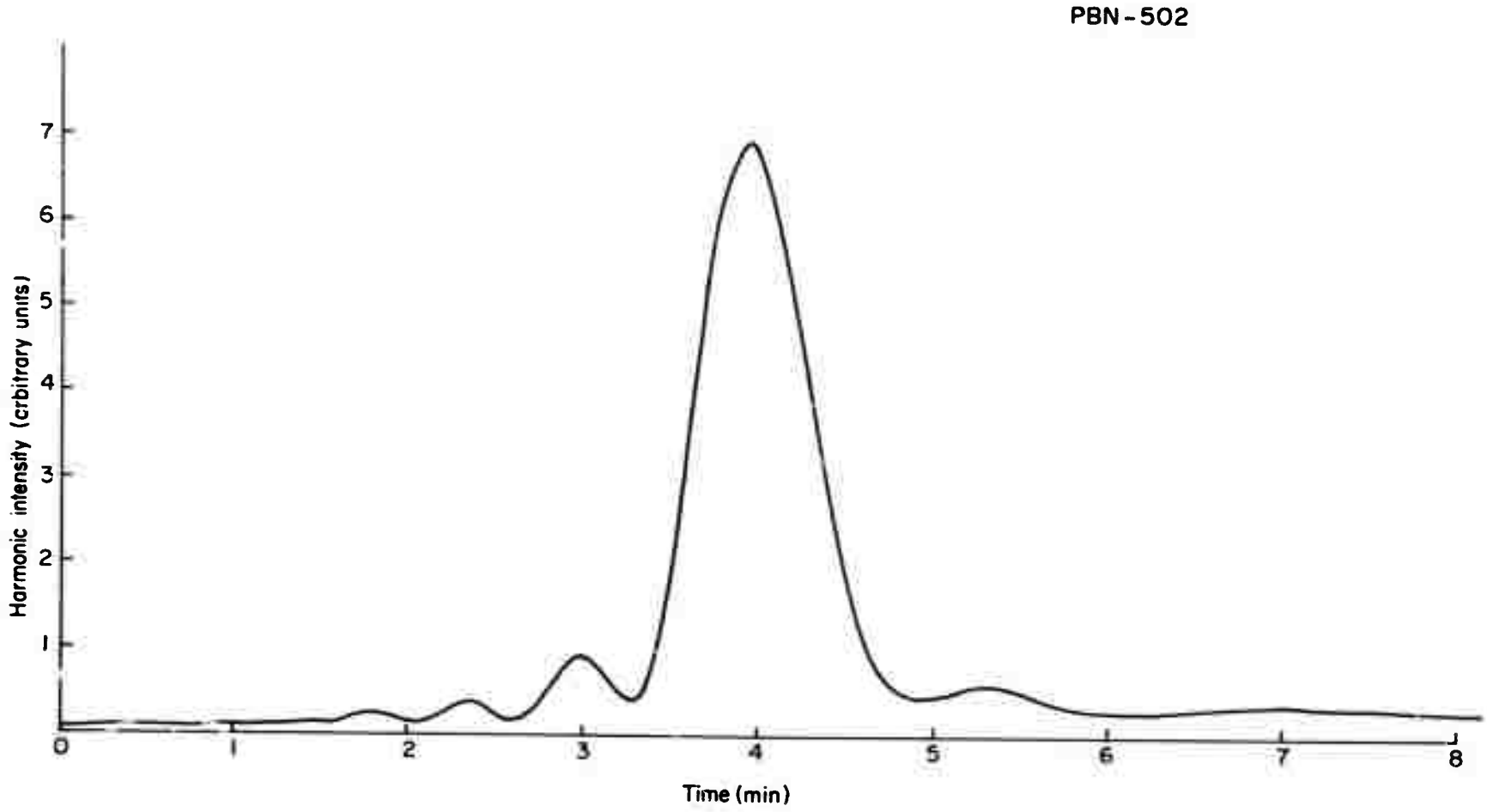

Fig. A-1 Harmonic Intensity vs Time. The SHG from a 1.5 cm long sample of "hot" $LiNbO_3$ generated by a long pulse Nd:YAG laser was monitored as a function of time. The average 1.06 μm power was 1 W and the average 0.53 μm power was < 5 mW.